

Dissertation in Astronomy
submitted to the
Combined Faculties of the Natural Sciences and Mathematics
of the Ruperto-Carola-University of Heidelberg, Germany,
for the degree of
Doctor of Natural Sciences

Put forward by
Dipl.-Phys. Nils Lippok
born in Ludwigshafen am Rhein

Oral examination: 22.01.2014

Earliest Phases of Star Formation

Physical and Chemical Properties of Prestellar Cores

Nils Lippok

Max-Planck-Institut für Astronomie

**Referees: Prof. Dr. Thomas Henning
Dr. Simon Glover**

Zusammenfassung

Mit dem Ziel, die physikalischen und chemischen Anfangsbedingungen bei der Entstehung von massearmen Sternen zu bestimmen, wurde die thermische Staubemission einer Auswahl von prästellaren Kernen mit dem *Herschel-Weltraumteleskop* beobachtet. Aus diesen Beobachtungen wurden die bisher genauesten Karten der Staubtemperatur- und Wasserstoffdichteverteilung in prästellaren Kernen abgeleitet. Dafür wurde eine Strahlverfolgungstechnik angewandt. Auf der Basis dieser neuen Erkenntnisse über die physikalischen Bedingungen in prästellaren Kernen modelliere ich die chemische Entwicklung des enthaltenen Gases. Vergleiche zwischen den Modellen und Beobachtungen der molekularen Linienemission zeigen, dass CO im Zentrum der Kerne stark ausfriert und dass dort sogar die Häufigkeit von N_2H^+ , einem Tracermolekül für hohe Dichten, vermindert ist. Die Modelle ergeben ein chemisches Alter der Kerne in der Größenordnung von 10^5 Jahren – vergleichbar mit der Freifalldauer. Ferner berechne ich die thermischen Gleichgewichtsverteilungen der prästellaren Kerne mit Strahlungstransportmodellen und vergleiche diese mit den beobachteten Verteilungen. Beide stimmen sehr gut überein, was die Zuverlässigkeit der Strahlverfolgungstechnik untermauert. Die Untersuchung ergibt darüber hinaus, dass die Übereinstimmung für eine Vielzahl von Staubmodellen gut ist. Schließlich präsentiere ich Ammoniakbeobachtungen von drei prästellaren Kernen und leite aus ihnen die Gastemperatur ab. Sie stimmen im Innern zweier Kerne, das von Ammoniak geprobt wird, mit den Staubtemperaturen überein. In einem weiteren Kern ist das Gas im Zentrum etwas wärmer als der Staub. Dies könnte die Folge einer verminderten Kollisionskopplung zwischen Gas und Staub auf Grund von Staubkoagulation sein.

Abstract

With the goal of constraining the initial physical and chemical conditions of low-mass star formation, the thermal dust emission of a sample of prestellar cores has been observed with the *Herschel Space Observatory*. From these observations, the most accurate maps of the dust temperature and density structures in prestellar cores existing today have been derived using a ray-tracing technique. Based on this new information on the physical conditions in the prestellar cores I model the chemical evolution of the associated gas. Comparison of the models to molecular line observations reveals that CO freezes out strongly in the core centers and that even the high density tracer N_2H^+ is affected by depletion. I derive a chemical age of the gas in all cores on the order of 10^5 yr which is comparable to the free-fall time of the cores. Furthermore, I calculate the thermal equilibrium distributions of the prestellar cores with radiative transfer models for comparison to the ray-tracing results. I find a very good agreement between the two methods confirming the reliability of the ray-tracing technique. It is also shown that the agreement is good for a large range of dust models. Finally, I present ammonia observations of three prestellar cores and use them as a gas temperature probe. Comparison of gas and dust temperatures shows that both agree in the inner parts of two cores traced by ammonia while the gas is slightly warmer than the dust in the third object; maybe due to a reduced collisional coupling between gas and dust because of coagulation of the dust grains.

CONTENTS

1	INTRODUCTION	1
	STAR FORMATION ON DIFFERENT SCALES	1
	PRESTELLAR CORES	3
	OBSERVATIONAL TRACERS OF PRESTELLAR CORES	3
	PHYSICAL CONDITIONS	4
	CHEMICAL CONDITIONS	7
	BOK GLOBULES	8
	THE EARLIEST PHASES OF STAR FORMATION (EPoS)	9
	SUBJECT OF THE THESIS	10
2	GAS-PHASE CO DEPLETION AND N₂H⁺ ABUNDANCES IN STARLESS CORES	13
2.1	INTRODUCTION	13
2.2	OBSERVATIONS	15
2.2.1	SOURCE SELECTION	15
2.2.2	CONTINUUM OBSERVATIONS	17
2.2.3	MOLECULAR LINE OBSERVATIONS	17
2.3	MODELING	18

2.3.1	DUST TEMPERATURE AND DENSITY MAPS FROM RAY-TRACING MODELS	18
2.3.2	CHEMICAL MODELING	19
2.4	RESULTS & DISCUSSION	23
2.4.1	DUST TEMPERATURE AND DENSITY MAPS	23
2.4.2	SIZES, MASSES, AND STABILITY OF THE CORES.	25
2.4.3	SPECTRA AND MOLECULAR EMISSION MAPS	26
2.4.4	CORE PROPERTIES CONSTRAINED FROM CHEMICAL MODELING	31
	The individual globules	31
	CO abundances	35
	N ₂ H ⁺ abundances	37
	Chemical age of the cores	38
	Strength of the impacting UV-field	39
	Constraints on the grain properties	41
2.5	CONCLUSIONS	41
2.A	OBSERVATIONS	42
2.B	HYDROGEN DENSITY AND DUST TEMPERATURE MAPS	50
2.C	LTE ANALYSIS	54
2.C.1	MODEL	54
2.C.2	RESULTS	55
3	MODELING OF DUST TEMPERATURE DISTRIBUTIONS IN STARLESS CORES	59
3.1	INTRODUCTION	59
3.2	DATA	60
3.3	MODELING	61
3.3.1	DUST MODELS	61
3.3.2	THE RAY-TRACING METHOD	62

3.3.3	RADIATIVE TRANSFER MODELING	64
3.4	MODELING RESULTS	66
3.4.1	DENSITY AND TEMPERATURE PROFILES DERIVED WITH THE RAY-TRACING TECHNIQUE	66
3.4.2	COMPARISON OF DUST RADIATIVE TRANSFER MODELS TO RAY-TRACING RESULTS	67
	Effect of using different dust models	67
	Effect of varying the total flux of the ISRF	70
	Effect of varying the extinction of the envelope	70
	Comparison for all globules	71
3.5	DISCUSSION	79
3.5.1	THE INDIVIDUAL OBJECTS	79
3.5.2	UNCERTAINTIES	80
3.5.3	STEEPNESS OF THE TEMPERATURE PROFILES	81
3.5.4	COMPARISON TO PREVIOUS STUDIES	82
3.6	CONCLUSIONS	82
4	COMPARISON OF DUST AND GAS TEMPERATURES IN STARLESS CORES	85
4.1	INTRODUCTION	85
4.2	OBSERVATIONS	86
4.3	RESULTS	87
4.3.1	INTEGRATED INTENSITY MAPS	87
4.3.2	GAS KINEMATICS	92
4.4	COLUMN DENSITY AND KINETIC TEMPERATURE DERIVED FROM AMMONIA	94
4.4.1	METHOD	94
4.4.2	UNCERTAINTIES	97
4.4.3	MAPS OF THE AMMONIA COLUMN DENSITY AND KINETIC TEMPERATURE	97
4.5	COMPARISON OF GAS AND DUST TEMPERATURES	98

4.6	DISCUSSION	100
4.7	SUMMARY	104
5	SUMMARY AND OUTLOOK	105
5.1	SUMMARY	105
5.2	OUTLOOK	106
	ACKNOWLEDGMENTS	109
	BIBLIOGRAPHY	111

Star formation is one of the most fundamental processes in the universe, transforming dilute gas into stellar systems – potential cradles of life. In fact, star formation is a whole complex of processes and stages, and one of the largest sub-fields in astronomy is devoted to its understanding. During the last decades, observations of countless sites related to the formation of stars have been poured into an evolutionary sequence still leaving many question unanswered. Prestellar cores are the evolutionary stage of the interstellar medium directly prior the onset of gravitational collapse to individual stars. The aim of this thesis is to observationally constrain the physical and chemical conditions in nearby prestellar cores.

STAR FORMATION OBSERVED AT DIFFERENT SCALES

Star formation is directly influenced by many factors like turbulence, magnetic fields, heating and cooling, gravity and feedback mechanisms, chemistry and environment. These effects act on all scales, from the subatomic to the kilo-parsec scale. This makes the observational and theoretical study of the star formation process as a whole very difficult. The study is further complicated because star formation occurs in varying conditions: isolated and clustered, in the outskirts of galaxies and even in extreme environments like the galactic center. Star formation takes place throughout the entire history of the Universe, from nearby galaxies in the present epoch to high red shift galaxies at large look-back times. Finally, most stages of star formation proceed slowly compared to observable time-scales with durations of hundreds of thousands to millions of years for a star to begin hydrogen burning after a first contraction of its parental cloud in the ISM. Astronomers can therefore only observe snap-shots of the star formation process. Because of the enormous complexity of the problem, observers as well as modelers restrict themselves to the study of specific aspects of star formation.

On the largest scales, astronomers estimate the star formation rate of entire galaxies at different cosmological epochs and link it to their evolution with the goal of understanding the star

formation history of the Universe (e.g., Hopkins & Beacom 2006). Even in most nearby galaxies, studies of extra galactic star formation cannot resolve single star forming regions. Astronomers, therefore, commonly derive surface densities of the star formation rate and relate them to surface densities of gas components (Kennicutt 1998). These studies revealed for instance that the star formation rate in spiral galaxies is closely correlated to the surface density of molecular gas but not to the cold atomic gas (e.g., Bigiel et al. 2008). This indicates that the star formation efficiency (with respect to the total gas) varies within and among galaxies. In contrast, the conditions for star formation inside individual molecular clouds observed on the kilo-parsec scale appear to be very similar.

When looking at smaller scales, we begin to resolve individual giant molecular clouds (GMCs). Regions of young stars and those of ongoing star formation are then spatially distinct. At this scale (about 300 pc) the "star formation law" linking surface densities of star formation and molecular gas breaks down (Heiderman et al. 2010; Schrubba et al. 2010). At the same time it becomes possible to study the nature of the individual GMCs and to relate them to the more global property of a star formation rate. For this purpose, a CO survey of the "Whirlpool" galaxy M51 is currently ongoing at the MPIA ("PAWS"; Schinnerer et al. 2013); this survey has for instance found that the star formation rate in GMCs depends on galactic streaming motions caused by an inhomogeneous galactic gravitational potential (Meidt et al. 2013).

Observing the internal structure of GMCs is only possible within our own galaxy. For instance, a CO survey of the galactic GMC W43 is currently conducted with the IRAM 30m telescope ("W43-HERO", Carlhoff et al. 2013). While the angular resolution of this study is a factor 10 worse than the resolution of the PAWS survey, the spatial resolution of 0.3 pc is roughly two orders of magnitude better because of lower distance (6 kpc vs. 8 Mpc). This survey found that W43 has a substructure of several filaments and dense clouds, and only locally concentrated regions of ongoing star formation (see also Beuther et al. 2012).

Turning to the nearest dense clouds at distances below 500 pc shows that also they have a filamentary sub structure. Indeed, observations by the *Herschel space observatory* (Herschel; Pilbratt et al. 2010) of the Gould Belt have revealed that a filamentary structure is omnipresent in dense clouds indicating that they are a natural result of a universal way of cloud formation (André 2013). These filaments are not only present in active star forming parts of dense clouds like the Aquila Rift but also in translucent clouds without ongoing star formation like the Polaris flare. This indicates that the build up of filamentary clouds occurs at an evolutionary stage before the condensation of prestellar cores. It has been found for the Aquila Rift complex that these filaments fragment locally into self-gravitating prestellar cores above a threshold hydrogen (atom) column density of $N_{\text{H}} \sim 1.4 \times 10^{22} \text{ cm}^{-2}$.

Furthermore, the core mass function (CMF) seems to be closely related to the stellar initial mass function (IMF) which indicates that the processes that lead to the formation of prestellar cores already determine to a large extent the final distribution of stars that will form in the cloud (e.g., Nutter & Ward-Thompson 2007; André et al. 2010). This is in agreement with

theoretical models that also suggest that the IMF is partly determined by cloud physics prior the onset of fragmentation (e.g., Hennebelle & Chabrier 2008). In fact, the core mass function in many star forming regions allows for the interpretation that prestellar cores typically form single stars with an efficiency of 20-40% (see André 2013 and references therein).

However, interferometric studies of nearby molecular cloud cores inhabiting protostars find that roughly half of them have protostellar companions within a few thousand AU (e.g., Connelley et al. 2008; Chen et al. 2013). This is only a lower limit of the companion fraction because the resolution and sensitivity of present-day studies is still limited. The processes in prestellar cores leading to fragmentation and angular momentum removal and eventually to individual protostars are not yet well understood (Hennebelle 2013). In this thesis we put new constraint onto the physical and chemical conditions in prestellar cores.

PRESTELLAR CORES

Prestellar¹ cores (and pre-brown dwarf cores, André et al. 2012) are the smallest units formed in molecular clouds and the sites at which gravitational collapse will lead to individual protostars. They typically have sizes of $\lesssim 0.1$ pc, contain gas of up to a few solar masses and have hydrogen number densities between 10^3 cm^{-3} and up to a few 10^6 cm^{-3} (Bergin & Tafalla 2007). They show only weak subsonic turbulent motions that are scale independent (e.g., Caselli et al. 2002; Tafalla et al. 2004). This is in stark contrast to their parental clouds and indicates that the turbulent driving of the gas breaks down at the scale of starless cores (Goodman et al. 1998). This "transition to coherence" can be considered as the starting point of the final evolution of the gas to stars. Therefore, the conditions in prestellar cores are often called "initial conditions of star formation". Constraining them from observations is of great importance for models of the earliest stages of star formation.

OBSERVATIONAL TRACERS OF PRESTELLAR CORES

The material that makes up prestellar cores consists to about 98% out of molecular hydrogen (H_2 ; Stahler & Palla 2005). This molecule has no permanent electric dipole moment and does thus not emit from rotational transitions at low temperatures. The main constituent of prestellar cores is thus not observable. However, the conditions in prestellar cores allow other molecular species to form and they can be used as tracers of the gas abundance, temperature,

¹The term "prestellar" is used differently in the literature. While some authors use it interchangeably with the term "starless", others relate it to a starless core's ability to form stars. Mostly, a starless core is considered prestellar when it is gravitationally bound. Others restrict the usage to cores that show direct evidence of instability like infall motions. I use the terms "prestellar" and "starless" interchangeably throughout the thesis and only emphasize if a starless core is actually star forming when it is relevant.

kinematics, and the magnetic field. The individual molecular abundances can also be used to constrain the age and history of the cores (see Bergin & Tafalla 2007 and references therein).

About 1% of the total mass of prestellar cores is concentrated in dust grains. They strongly extinct optical light from background stars. The near and mid-infrared background emission is less affected, and extinction measurements in this wavelength range can yield column densities of the dust in the cores. They can subsequently be converted to hydrogen column densities by assuming a gas-to-dust ratio (see e.g., Alves et al. 2001; Kainulainen et al. 2013). A complementary measurement of the dust column densities can be obtained from the thermal continuum radiation of the dust grains (e.g., Launhardt & Henning 1997; Launhardt et al. 2010, 2013). Its spectral energy distribution peaks in the far-infrared for typical temperatures around 10 K in prestellar cores. From the ground, only the (sub-)mm part of their spectral energy distribution can be observed with satisfactory precision. This emission traces the column densities of starless cores because it is optically thin even at the highest column densities. However, in contrast to extinction measurements, the derivation of column densities from thermal (sub-)mm emission requires the assumption of a corresponding dust temperature. Only by sampling the peak of the thermal dust emission – which requires observations outside the earth’s atmosphere – it is possible to constrain the dust temperature and column density from observations simultaneously. In fact, observing the thermal emission of “the cold universe” was the main purpose of the *Herschel Space Observatory*.

PHYSICAL CONDITIONS IN PRESTELLAR CORES

DENSITY

Observational studies of prestellar cores have revealed density profiles that drop following a power-law at large radii and flatten towards the center of the cores (e.g., Ward-Thompson et al. 1994, 1999). The profiles were empirically described by a broken power-law (Ward-Thompson et al. 1994, 1999), a softened power-law (Tafalla et al. 2002) or Plummer-like profiles (Whitworth & Ward-Thompson 2001; Nielbock et al. 2012). The central hydrogen number density of cores n_{H} ranges typically between a few 10^4 cm^{-3} and a few 10^6 cm^{-3} .

A physical model assuming that prestellar cores are spherical, isothermal, self-gravitating, pressure bound, and only supported against gravity by thermal pressure, leads to density profiles described by Bonnor-Ebert spheres (Ebert 1955; Bonnor 1956). They generally represent observations well (Bacmann et al. 2000; Alves et al. 2001; Kandori et al. 2005; Kirk et al. 2005; Shirley et al. 2005). The model can be expanded to assume non-isothermality, but Evans et al. (2001) showed that the effect on the hydrostatic equilibrium is small. However, these studies also found that the observed profiles when interpreted as Bonnor-Ebert spheres are generally not stable against gravitational contraction. Stable Bonnor-Ebert spheres require higher gas temperatures or stronger turbulence in the cores than observed. Another explana-

tion is that prestellar cores are in a contracting phase but this is only observed for a fraction of the cores (see below). Moreover, models based on very different physical conditions can also lead to shapes of prestellar cores that can be described as Bonnor Ebert spheres. This is even the case for models assuming supersonic turbulence in the cores (Ballesteros-Paredes et al. 2003). Likewise, models that account for stabilization by magnetic fields against gravitation predict centrally flattened density profiles (e.g., Lizano & Shu 1989). Because of all these potential explanations for the density structure of prestellar cores, its true origin remains unclear and observations of the density profile alone cannot distinguish between the scenarios.

TEMPERATURE

The temperature structure of prestellar cores is a result of heating and cooling processes. Since gas and dust are affected differently by heating sources and also cool by radiating independently, gas and dust temperatures are generally different. Only at hydrogen densities above a few 10^4 cm^{-3} the temperatures are expected to become coupled due to collisions between molecules and dust grains (Goldsmith 2001; Galli et al. 2002).

There are two principal external heating sources of prestellar cores: the inter-stellar radiation field (ISRF) and cosmic rays (CR). In the interior, the dust is mainly heated by the former and the gas by the latter source. Only in the low density envelopes, the gas is photo-electrically heated by the UV-component of the ISRF causing a strongly increased gas temperature (e.g., Bergin et al. 2006). In their interior, the cores are completely shielded from UV-radiation by the outer envelope of dust and gas.

The dust cools purely by thermal radiation. At low densities, also the gas can cool by radiation but the line emission of main coolants like CO soon becomes optically thick and at hydrogen densities above 10^4 cm^{-3} many molecules, and in particular CO, freeze out onto the dust grains reducing further the ability of the gas to cool from line emission. Instead, collisional coupling between gas and dust becomes effective and the molecules are cooled by collisions with the dust grains. Whether this heats the dust at the same time is theoretically not fully understood. While Evans et al. (2001) argue that the dust temperature would not be changed, models by Goldsmith (2001) predict a dust temperature increase of about 1-2 K from the collisions.

Measurements of the dust temperature from the thermal dust emission so far suffered heavily from the limitations of the available telescopes. Low-resolution observations by the *Infrared Space Observatory* (ISO; Kessler et al. 1996) revealed central dust temperatures of 10-12 K and 15-20 K in the outskirts of prestellar cores (Ward-Thompson et al. 2002). This is in agreement with radiative transfer models of the temperature equilibrium distributions (Evans et al. 2001; Zucconi et al. 2001; Stamatellos & Whitworth 2003; Gonçalves et al. 2004), but the observational constraints on the dust temperature from these early observations is only weak. They were significantly improved by *Herschel* observations obtained as part of the EPoS project (see below and also Stutz et al. 2010; Nielbock et al. 2012; Launhardt et al. 2013;

Lippok et al. 2013; Schmalzl et al. submitted).

The gas temperature is of greater importance for the thermal stability of prestellar cores than the dust temperature as it represents the major fraction of the core mass. Ammonia observations yield central gas temperatures in prestellar cores around 10 K (Bergin & Tafalla 2007) which is similar to estimates of the central dust temperature. Deriving gas temperatures at lower densities involves relatively high uncertainties, because it requires knowledge about the distribution of the tracer molecules and their level excitations. For this purpose, CO is most commonly used. Its low-lying rotational states are already excited at low densities (Evans 1999) and being the by far most abundant tracer molecule its emission is relatively strong. The so far most comprehensive study on the gas temperature in prestellar cores was probably done by Bergin et al. (2006) for the Bok globule B 68. With a significant modeling effort they derived a gas temperature of 6-7 K using isotopologues of CO that trace intermediate hydrogen densities in the core around 10^4 cm^{-3} . The gas in this region seems to be colder than the modeled dust temperature of the same region. In the center of the core many molecules like CO deplete from the gas phase and cannot act as coolants. Hence, the gas temperature increases. Traced with ammonia, the central gas temperature of B 68 is about 10 K and the gas is warmer than the dust. This implies that the gas and dust temperatures in this particular are not even perfectly coupled at the highest densities.

KINEMATICS

The contribution of the rotational and turbulent energy to the stabilization of starless cores against gravity is small with the rotational and turbulent energy being typically only a few percent of the gravitational energy. However, the velocity structure harbors clues on the mechanisms that lead to the formation and evolution of the cores. For detailed reviews, see Bergin & Tafalla (2007); André et al. (2009) and Hennebelle (2013). Since the work in this thesis does not focus on the kinematics of prestellar cores, I only briefly summarize a few important points.

Isolated prestellar cores as well as prestellar cores in turbulent clustered regions show only weak and subsonic turbulent motions even at radii of more than 0.25 pc from the core center. This finding is hard to explain by models of core formation with pure hydrodynamic gravoturbulent fragmentation (e.g., Klessen et al. 2005). It rather indicates that magnetic fields have a strong impact on the formation of prestellar cores. Prestellar cores are generally found to rotate slowly and, moreover, slower than clouds (Goodman et al. 1993) that contain cores. This requires a mechanism that removes the angular momentum of the contracting gas. A possible explanation is a coupling of the gas with its environment via magnetic fields. This behavior might, however, also be explained by turbulent fragmentation (Jappsen & Klessen 2004). Observations of the velocity structure of prestellar cores lead in general to an ambiguous picture. While infall motions are detected in some cases, also cores without motions in radial direction

and even expanding motions are observed (e.g., Schnee et al. 2013).

MAGNETIC FIELDS

Magnetic fields have a stabilizing effect on prestellar cores, since they counteract infall motions of the gas perpendicular to the magnetic field lines. On the other hand, they also contribute to the removal of angular momentum in the cores through magnetic braking. Their importance for the star formation process is not yet completely understood (e.g., André et al. 2009). However, measurements of the magnetic field strength in starless cores find that the magnetic field is typically on the order needed to counteract gravity (Heiles & Crutcher 2005) indicating that their contribution to the stabilization of the cores is relevant.

CHEMICAL CONDITIONS IN PRESTELLAR CORES

Despite being extremely cold and rarefied – a particle density of 10^5 cm^{-3} which is found in "dense" cores corresponds to extreme ultrahigh vacuum (XUHV) in laboratories on earth – the material in starless cores evolves chemically over the course of thousands of years (see e.g., Herbst & van Dishoeck 2009). The appearance of molecules other than H_2 in the gas is of great importance. They have for instance influence on the cloud's ability to cool or on its ionization fraction which in turn determines the effectiveness of the magnetic field coupling to the gas. Some molecular species can be used as observational tracers of the density and kinematics, the ionization fraction or the magnetic field strength of the cores. Modeling the chemical abundances observed in starless cores permits constraining their history and age using them as "chemical clock".

The second most abundant molecule in the ISM after H_2 is CO. It is the most common tracer of the ISM (because H_2 does not emit at the conditions in prestellar cores). CO has a relatively small dipole moment so that it is excited already at low densities. All other molecules have typically a few orders of magnitudes lower abundances than CO. At the high densities and low temperatures in the centers of prestellar cores, however, CO freezes out onto the dust grains making it unsuitable as tracer of the density (see e.g., Bergin & Tafalla 2007). Its disappearance at the same time allows other molecules to build up in the gas that would otherwise be destroyed, because CO is a main agent to react with ions in the gas phase. For instance H_3^+ , a precursor of many molecules, reacts with CO. Important molecules that appear in the gas phase when CO is depleted are N_2H^+ and its daughter molecule NH_3 . Comparing observations of various molecules with models of the chemical evolution in their environment therefore permits to constrain the history and age of the cores.

Another effect of carbon and oxygen depletion is the increase of deuterated species in the gas phase. Their precursor is in many cases H_3^+ as well. This molecule can react with HD to form

H_2D^+ and further to form D_2H^+ and D_3^+ (see e.g., Albertsson et al. 2013). These reactions are exothermic which leads to an enhancement of observable deuterated species in prestellar cores, because the back-reaction is suppressed in the cold cores. The relative abundance of deuterated species therefore provides constraints on the thermal history of cores.

The freezeout of many molecules onto the dust grains also changes the grain properties. The ice-layers favor coagulation so that the grains grow over time and form fluffy aggregates (e.g., Ossenkopf 1993; Ormel et al. 2009). This reduces the surface area of the grains which in turn influences the molecular abundances in the gas phase, since molecular reactions on grain surfaces play an important role in the chemistry of prestellar cores (e.g., Hasegawa & Herbst 1993). Furthermore, freezeout and coagulation change the opacity of the dust grains and therefore the temperature in the cores (e.g., Ossenkopf & Henning 1994; Ormel et al. 2011).

BOK GLOBULES

Bok globules appear as small and relatively isolated dark regions in the night sky when observed with optical telescopes. These objects were discovered by Herschel (1785) but were first related to the formation of stars about 60 years ago by Bok (1948). Today it is known that Bok globules are small molecular clouds that often contain one or two star-forming cores, in many cases at different evolutionary stages (Launhardt et al. 2010). Bok globules are usually found in proximity to larger cloud complexes. They also show a similar line-of-sight velocity as these clouds (Launhardt & Henning 1997). It is therefore believed that Bok globules form as part of larger molecular clouds and are isolated at later stages. Because of their proximity, isolation and relatively simple structure, globules are ideal objects to study many aspects of star formation in detail, like the kinematic structure, the fragmentation, collapse and chemistry, that lead to the formation of individual protostars. However, these results cannot be directly transferred to the more common formation of stars in clustered regions, since the conditions there are different. For instance, cores in clusters are less exposed to the external ISRF and may feel a different external pressure. They may also be affected by outflows of nearby protostars, competitive accretion, or the radiation of nearby young massive stars (Ward-Thompson et al. 2007). The different conditions become manifest by prestellar cores in cluster-forming regions being typically smaller but having higher column densities. Deciphering the processes at play in clustered star-formation observationally, is a formidable task, because of the 2D projection of an arbitrary 3D structure and other effects like source blending or large opacities. A viable theory of star formation has to be able to describe the star formation process in the conditions in clusters as well as in the other extreme of isolation. For the latter conditions, Bok globules offer the optimal test bed.

THE EARLIEST PHASES OF STAR FORMATION (EPoS) – A HERSCHEL GUARANTEED TIME KEY PROJECT

The cold dust in star forming clouds emits the bulk of its thermal dust radiation in the FIR. This radiation is not accessible with ground based telescopes. Only the long-wavelength portion of the thermal emission is observable from the ground due to the effects of the Earth's atmosphere. Measurements of this radiation have been the basis of estimates of masses and the density structure of star-forming cores. Other tracers like molecules are less suited because their relative abundance with respect to the total cloud mass is less constrained and NIR-extinction measurements have the disadvantage that they lose sensitivity at the highest column densities found in starless cores. However, without knowing the dust temperature any derivation of the dust density from dust emission has large uncertainties. This is illustrated by the following example. The dust emission follows the Planck law of black-body radiation modified by the frequency dependent emissivity of the dust grains (modified black-body radiation). At a wavelength of 1 mm, which is observable from the ground, more than twice the amount of 8 K dust is needed to emit the same flux density as 12 K dust. A temperature estimate of 10 ± 2 K thus still results in an uncertainty of the dust mass by a factor of 2. Furthermore, the dust temperature itself (which is close to the gas temperature as discussed above) is also a very important property of the cores since it determines the thermal pressure.

In order to measure the temperature of the radiating dust, it is necessary to observe the peak of the emission spectrum. This was in the past only possible at low resolution and sensitivity, e.g., with *ISO*. This satellite was operated between 1996 and 1998. It had a resolution of about $2'$ at $240 \mu\text{m}$ which is too low to resolve even the nearest cores. And observations of obscured cluster-forming regions heavily suffered from source blending. With the *Herschel Space Observatory* that operated at the second Lagrangian point of the Earth-Sun system from 2009 until 2013, it has for the first time become possible to sample the peak of the spectral energy distribution (SED) of the cold dust with a resolution that permits investigating single star forming cores in nearby clouds and that is of the same order as that of complementary ground based (sub-)mm observatories. The MPIA therefore initiated the guaranteed time key program "Earliest Phases of Star Formation" (EPoS) with the aim of constraining the initial physical conditions in star forming regions better than ever before. As one part of this project², a previously well studied sample of 15 Bok globules has been observed with the *Herschel* photometers of the Photodetector Array Camera and Spectrometer (PACS; Poglitsch et al. 2010) in the $100 \mu\text{m}$ and $160 \mu\text{m}$ bands and the Spectral and Photometric Imaging Receiver (SPIRE; Griffin et al. 2010) in the $250 \mu\text{m}$, $350 \mu\text{m}$, and $500 \mu\text{m}$ bands. In order to reduce the background confusion noise, only such globules were chosen for the EPoS sample that lie slightly

²The EPoS project has two parts. Besides the part dedicated to the observations of Bok globules, a second part focuses on potential sites of high-mass star formation. In total a sample of 45 regions has been observed in order to better understand the mechanisms that lead to the formation of stars with the highest masses ($M > 8M_{\odot}$). For early results see Henning et al. (2010); Beuther et al. (2010); Linz et al. (2010); Beuther et al. (2012); Ragan et al. (2012) and Pitann et al. (2013).

outside the galactic plane. This ensured background levels of about 1 mJy/arcsec^2 . Typical values in Taurus and Ophiuchus attain for example between 2 and 4 mJy/arcsec^2 (Launhardt et al. 2013). As a result, the $100 \mu\text{m}$ maps of the globules of the EPoS sample are deeper than most maps of large-area surveys and permit deriving robust dust temperature estimates.

The first result of the EPoS project was line-of-sight averaged dust temperature and column density maps of Bok globules (Stutz et al. 2010; Launhardt et al. 2013). They were derived from modified black-body fits to the spatially resolved SEDs of the thermal dust emission using the *Herschel* data in combination with (sub-)mm data from ground-based observations. In a next step, a ray-tracing technique was developed that determines the temperature structure in the cores taking into account a thermal gradient along the line-of-sight when fitting the SEDs. Maps of the mid-plane dust temperature and hydrogen density obtained with this method for the globules containing starless cores are presented in (Nielbock et al. 2012; Lippok et al. 2013; Schmalzl et al. submitted). In the future, it is planned to upgrade the ray-tracing technique and to apply it also to protostellar cores. As a further step, three-dimensional radiative transfer forward modeling will be applied to derive the thermal structure of the prestellar cores making use of the full spatial information of the different wavelength bands of the observations. By taking into account also NIR observations it is planned to also constrain the dust properties in the cores.

SUBJECT OF THE THESIS

The work in this thesis bases on the newly obtained information on the dust temperature and density structure of starless cores derived from observations by *Herschel* as part of the EPoS project.

In Chapter 2, I explore the chemical evolution of the gas in the starless cores for the physical conditions constrained by the dust temperature and density maps derived from the *Herschel* data. I apply time-dependent chemical modeling and subsequently calculate synthetic observations using line-radiative transfer modeling. By comparing the modeling results to observations of ^{12}CO , ^{13}CO , C^{12}O and N_2H^+ in these cores, I constrain the abundance of the molecules and their depletion in the core centers. I further derive the chemical age of the cores.

In Chapter 3, I compare the ray-tracing results of the starless cores for different dust opacity models. Then I test, if the derived dust temperature and density structures are in agreement with radiative transfer models of the thermal equilibrium distributions in the cores. This test is meant to validate the ray-tracing method and to constrain the pool of dust models that are in accordance with the observations.

In Chapter 4, I derive the gas temperature of the starless cores from ammonia observations. I compare the gas and dust temperatures in order to test, if they are coupled and under which

conditions they might decouple.

In Chapter 5, I summarize the findings of this thesis and give an outlook.

GAS-PHASE CO DEPLETION AND N_2H^+ ABUNDANCES IN STARLESS CORES

*This Chapter is adapted from the paper
Lippok, Launhardt, Semenov, et al. 2013, A&A 560, A41.*

2.1 INTRODUCTION

Stars form in cold cloud cores. In the prestellar phase, the centers of the cloud cores cool down to temperatures below 10 K and the hydrogen densities typically exceed 10^5 cm^{-3} . At these conditions complex molecules are synthesized (e.g., Bacmann et al. 2012). At the same time, in the densest regions of the cores, many molecular species stick onto the dust grains (e.g., Bergin & Tafalla 2007). The evolution of the chemical composition influences the cooling rate of the clouds and changes the degree of ionization - both important properties which influence the star formation process.

The gas in the local interstellar medium (ISM) consists of about 98% molecular hydrogen and helium. These species, however, do not emit at cold temperatures. Therefore, CO has become a popular tracer of the ISM. It is the second most abundant molecule and readily excited already at low temperatures. However, at the conditions in prestellar cores, CO freezes out onto the dust grains. This alters the chemical composition of the cloud cores and the dust properties. Nitrogen-bearing species like N_2H^+ , which are otherwise destroyed by CO molecules, can now accumulate in the gas phase and trace these denser regions. N_2H^+ molecules form and deplete on longer time-scales than CO. Under reasonable assumptions of the initial abundances, physical conditions, and reaction rates, modeling both species together can therefore constrain the chemical age of the cores.

While early studies had already detected CO mantles on dust grains from absorption features in the mid-infrared (e.g., Tielens et al. 1991), direct observational proof of molecular depletion

from the gas-phase in the centers of dense cores came only later. It requires the accurate determination of molecular abundances in the gas phase and of the total gas mass. One of the most robust ways to determine the total mass in dense clouds is to infer it via a presumably known gas-to-dust mass ratio from (column-) densities of the dust. They in turn can be derived from the black-body radiation of the dust grains (e.g., Launhardt et al. 2013) or the visual to mid-infrared extinction caused by the dust (e.g., Witt et al. 1990; Alves et al. 2001).

Several studies have been performed that quantify the CO depletion in starless cores on the basis of hydrogen masses deduced from dust measurements (e.g., Willacy et al. 1998; Caselli et al. 1999; Bacmann et al. 2002; Bergin et al. 2002; Tafalla et al. 2004; Pagani et al. 2005; Stutz et al. 2009; Ford & Shirley 2011). All of them found strong indications for a central freezeout of CO. So far, however, the observational studies of molecular depletion had no or only weak constraints on the temperature distribution within molecular clouds. Knowledge of the dust temperature is however essential for both deriving column densities from the dust emission and robust chemical modeling (Pavlyuchenkov et al. 2007). Uncertainties in the temperature also introduce large errors to the hydrogen densities derived from (sub-)mm dust emission.

Isolated Bok globules, which often contain only a single dense core and are devoid of larger envelopes, are the best suited objects for detailed studies of the physical and chemical structure of starless cores. We have therefore observed seven globules containing a starless core as part of the *Herschel* Guaranteed Time Key project EPoS. The *Herschel* space observatory (Pilbratt et al. 2010) and its sensitive PACS (Poglitsch et al. 2010) and SPIRE (Griffin et al. 2010) bolometer arrays have made it possible to sample the peak of the thermal spectral energy distributions (SED) of cold molecular clouds with high sensitivity and spatial resolution for the first time. In Stutz et al. (2010); Launhardt et al. (2013) we presented dust temperature and hydrogen density maps of the starless cores in the globules derived by modified black-body fits to the continuum emission. We have also developed a ray-tracing method to restore the full volume density and dust temperature structure of these cores. The results are presented in Nielbock et al. (2012) for B 68, for CB 17 in Schmalzl et al. (submitted), and in this paper for the remaining five globules.

We also present maps of the ^{12}CO (J=2-1), ^{13}CO (J=2-1), C^{18}O (J=2-1), and N_2H^+ (J=1-0) transitions of the same seven globules. The maps of ^{12}CO (J=2-1) and ^{13}CO (J=2-1) of the globules CB 17, CB 26, and CB 244 were previously presented in Stutz et al. (2009). Based on dust temperature and hydrogen density maps derived from the *Herschel* observations and using time-dependent chemical modeling, we derive the molecular abundances. From the modeling results we also constrain the chemical age of the cores and infer information on the dust grains in the globules.

The paper is structured as follows. In Section 2 we describe the observations and data reduction. In Section 3 we describe our modeling approaches. In Section 4 we present and discuss the results. We summarize our findings in Section 5. Maps of the observations and the derived

Table 2.1: Source list

Source	Other names	R.A., Dec. (J2000) ^a [h:m:s, °:':"]	Region	Dist. [pc]	Ref.
CB 4	...	00:39:05.2, +52:51:47	Cas A, Gould Belt (GB)	350 ± 150	1
CB 17 ^b	L 1389	04:04:37.1, +56:56:02	Perseus, GB	250 ± 50	2, 1
CB 26 ^c	L 1439	05:00:14.5, +52:05:59	Taurus-Auriga	140 ± 20	2, 3,4
CB 27	L 1512	05:04:08.1, +32:43:30	Taurus-Auriga	140 ± 20	3,4,5
B68	L 57, CB 82	17:22:38.3, -23:49:51	Ophiuchus, Pipe nebula	135 ± 15	6, 7, 8
CB 130 ^d	L 507	18:16:14.3, -02:32:41	Aquila rift, GB	250 ± 50	9, 10
CB 244 ^e	L 1262	23:25:26.8, +74:18:22	Cepheus flare, GB	200 ± 30	2, 4, 11

Notes. ^(a) These are the positions of the center of the starless cores. They are defined as column density peaks found in Launhardt et al. (2013). ^(b) CB 17: additional low-luminosity Class I YSO 25'' from starless core. ^(c) CB 26: additional Class I YSO 3.6' south-west of the starless core. ^(d) CB 130: additional Class 0 core ~ 30'' east and Class I YSO ~ 45'' east of starless core. ^(e) CB 244: additional Class 0 source ~ 90'' east of starless core.

References. (1) Perrot & Grenier (2003); (2) Launhardt et al. (2010); (3) Loinard et al. (2011); (4) Stutz et al. (2009); (5) Launhardt et al. (2013); (6) de Geus et al. (1989); (7) Lombardi et al. (2006); (8) Alves & Franco (2007); (9) Launhardt & Henning (1997); (10) Straizys et al. (2003); (11) Kun (1998).

dust density and hydrogen density maps are shown in the on-line appendix. We also present a simple LTE analysis of the molecular column densities in Appendix 2.C.

2.2 OBSERVATIONS

2.2.1 SOURCE SELECTION

Within the EPoS project, 12 nearby Bok globules have been observed with the *Herschel* bolometers. The sample of globules has been selected based on results from previous studies (see Launhardt et al. 2013 and references therein) and was known to contain low-mass pre- and protostellar cores. Of particular importance for the selection was the criterion that the globules be very isolated and located outside the galactic plane. Their mean galactic latitude is 7.3 ± 3 degrees, with the closest one still 3.5 degrees away from the galactic plane, such that background levels and confusion from the galactic plane are minimized. Out of the 12 globules, seven globules contain starless cores. These globules are studied in this paper and are listed in Table 3.1. Three of the globules contain only a single starless core (CB 4, CB 27, and B 68), one contains an additional Class 0 core (CB 244), and two contain an additional Class I young stellar object (CB 17 and CB 26). CB 130 contains two additional cores (Class 0 and I).

Table 2.2: List of observations

Source	Line	Freq. [GHz]	Tel.	Date [mo/yr]	HPBW [arcsec]	Δv [m s ⁻¹]	η_{mb}	Map size	Ref.
CB 4	^{12}CO (2–1)	230.537990	HHT	10/09	32.2	300	0.85	10' × 10'	
	^{13}CO (2–1)	220.398686	HHT	10/09	33.7	300	0.85	10' × 10'	
	C^{18}O (2–1)	219.560319	30m	12/10	11.3	53	0.52	3' × 3'	
	N_2H^+ (1–0)	93.1737	30m	12/10	26.6	63	0.75	3' × 3'	
CB 17	^{12}CO (2–1)	230.537990	HHT	04/08	32.2	300	0.85	10' × 10'	
	^{13}CO (2–1)	220.398686	HHT	04/08	33.7	300	0.85	10' × 10'	
	C^{18}O (2–1)	219.560319	30m	10/96	10.9	107	0.48	35''/ 7''	
	N_2H^+ (1–0)	93.1737	30m	10/96	26.6	63	0.95	140'' × 140''	
CB 26	^{12}CO (2–1)	230.537990	HHT	03/09	32.2	300	0.85	10' × 10'	1
	^{13}CO (2–1)	220.398686	HHT	03/09	33.7	300	0.85	10' × 10'	1
	C^{18}O (2–1)	219.560319	30m	12/10	11.3	53	0.52	6' × 5'	
	N_2H^+ (1–0)	93.1737	30m	12/10	26.6	63	0.75	6' × 5'	
CB 27	^{12}CO (2–1)	230.537990	HHT	01/07	32.2	300	0.85	10' × 10'	1
	^{13}CO (2–1)	220.398686	HHT	01/07	33.7	300	0.85	10' × 10'	1
	C^{18}O (2–1)	219.560319	30m	12/10	11.3	53	0.52	3' × 3'	
	N_2H^+ (1–0)	93.1737	30m	12/10	26.6	63	0.75	3' × 3'	
B 68	^{12}CO (2–1)	230.537990	HHT	03/08	32.2	300	0.85	10' × 10'	
	^{13}CO (2–1)	220.398686	HHT	03/08	33.7	300	0.85	10' × 10'	
	C^{18}O (1–0)	109.782182	30m	04/00	23.6	30	0.91	4' × 4' / 12'' ^(a)	
	N_2H^+ (1–0)	93.1737	30m	04/01	26.6	63	0.75	3' × 3' / 12-24'' ^(a)	
CB 130	^{12}CO (2–1)	230.537990	30m	07/11	11.3	51	0.92	4' × 4'	
	^{13}CO (2–1)	220.398686	30m	07/11	11.8	53	0.92	4' × 3'	
	C^{18}O (2–1)	219.560319	30m	01/11	11.3	53	0.52	5' × 5'	
	N_2H^+ (1–0)	93.1737	30m	01/11	26.6	63	0.75	5' × 5'	
CB 244	^{12}CO (2–1)	230.537990	HHT	04/08	32.2	300	0.85	10' × 10'	1
	^{13}CO (2–1)	220.398686	HHT	04/08	33.7	300	0.85	10' × 10'	1
	C^{18}O (2–1)	219.560319	30m	12/10	11.3	53	0.52	5' × 5'	
	N_2H^+ (1–0)	93.1737	30m	12/10	26.6	63	0.75	5' × 5'	

Notes. ^(a) Data first presented in [Bergin et al. \(2002\)](#). These maps were obtained from tracked observations with the listed pointing separations.

References. (1) [Stutz et al. \(2009\)](#)

2.2.2 CONTINUUM OBSERVATIONS

All globules were observed in the *Herschel* PACS bands at 100 and 160 μm and the *Herschel* SPIRE bands at 250 μm , 350 μm , and 500 μm . These observations were complemented with ground-based (sub-) mm observations ranging from 450 μm to 1.2 mm. The respective observations and data-reduction are described in detail in [Nielbock et al. \(2012\)](#) and [Launhardt et al. \(2013\)](#), and references therein. The dust temperature and density maps presented in Sect. 2.4.1 were derived from this set of observations.

2.2.3 MOLECULAR LINE OBSERVATIONS

On-the-fly maps of the C^{18}O ($J=2-1$) line at 219.560 GHz and the N_2H^+ ($J=1-0$) line complex around 93.174 GHz have been taken at the IRAM 30m telescope between November 2010 and January 2011 of all starless cores except B 68. For this globule, we used data that were obtained before and published in [Bergin et al. \(2002\)](#). The observing parameters are compiled in Tab. 2.2. Map sizes are different for different sources and range from $3' \times 3'$ to $6' \times 5'$. The HPBWs were 12'' for C^{18}O and 28'' for N_2H^+ . The channel widths were 40 kHz for C^{18}O and 20 kHz for N_2H^+ , corresponding to 0.05 and 0.06 km/s, respectively. Both molecular transitions were observed simultaneously using the EMIR receivers ([Carter et al. 2012](#)). Calibration was done using the standard chopper-wheel method every 15 minutes. The weather conditions were mixed during the course of the observations leading to mean system temperatures of 700 K for C^{18}O and 180 K for N_2H^+ , respectively. During the observations of CB 130 the weather was better, resulting in lower system temperatures of 300 K and 100 K, respectively.

To minimize scanning artifacts, the on-the-fly maps were taken with two orthogonal scan directions with two coverages each and a scanning speed of 6''/s. A reference position was observed approximately every 1.5 minutes. These positions were derived from IRIS 100 μm all-sky maps ([Miville-Deschênes & Lagache 2005](#)). They lie within extended regions of the lowest 100 μm continuum emission, preferentially within 10' from the source and were expected to have most likely no CO emission.

Molecular line maps of the ^{12}CO and ^{13}CO species at the $J = 2 - 1$ transition (230.538 GHz and 220.399 GHz) were obtained with the *Heinrich Hertz Submillimeter Telescope* (HHT) on Mt. Graham, Arizona, USA. The channel width was ~ 0.34 km/s and the angular resolution of the telescope was 32'' (*FWHM*). For more details on the observations and data reduction, we refer the reader to [Stutz et al. \(2009\)](#).

Table 2.2 lists all molecular line observations used for this study. All maps were reprojected to the coordinate system of the corresponding dust temperature and density maps. They have also been smoothed to the same Gaussian beam size of 36.4'' (resolution of the SPIRE 500 μm maps and the dust temperature and density maps) and been regridded to the same pixel scale

of $10'' \times 10''$.

2.3 MODELING

2.3.1 DUST TEMPERATURE AND DENSITY MAPS FROM RAY-TRACING MODELS

The goal of the ray-tracing fitting of the continuum observations of the starless cores is to go beyond the line-of-sight (LoS) optical depth-averaged analysis presented in [Launhardt et al. \(2013\)](#) by also modeling the dust temperature variation along the LoS and deriving volume density distributions. The ray-tracing algorithm developed to derive the dust temperature and density structure of the cores from the *Herschel* and complementary ground-based continuum maps is described in [Nielbock et al. \(2012\)](#). Here, we only briefly summarize the hydrogen density and temperature profiles used by the algorithm and mention the formulae to illustrate the meaning of the profile parameters.

For all modeling steps we use the dust opacities $\kappa_d(\nu)$ tabulated in [Ossenkopf & Henning \(1994\)](#)¹ for mildly coagulated composite dust grains with thin ice mantles (10^5 yrs coagulation time at gas density 10^5 cm^{-3})². The density profiles of the cores have been modeled assuming a ‘‘Plummer’’-like shape ([Plummer 1911](#)), which characterizes the radial density distribution of prestellar cores on the verge of gravitational collapse ([Whitworth & Ward-Thompson 2001](#)):

$$n_{\text{H}}(r) = \frac{\Delta n}{\left(1 + \left(\frac{r}{r_0}\right)^2\right)^{\eta/2}} + n_{\text{out}} \quad \text{if } r \leq r_{\text{out}} \quad (2.1)$$

where $n_{\text{H}} = 2 \times n(\text{H}_2) + n(\text{H})$ is the total number density of hydrogen nuclei. The radius r_{out} sets the outer boundary of the model cloud. The density beyond this radius is set to zero. We add a constant term to the profile to account for the fact that the outer density and column density profiles in most globules do not drop off like a power law, but turn over into a low-density envelope. This profile (i) accounts for an inner flat density core inside r_0 with a peak density $n_0 = n_{\text{out}} + \Delta n$ ($\Delta n \gg n_{\text{out}}$), (ii) approaches a modified power-law behavior with an exponent η at $r \gg r_0$, (iii) turns over into a flat-density halo outside r_1 , where

$$r_1 = r_0 \sqrt{\left(\frac{\Delta n}{n_{\text{out}}}\right)^{2/\eta} - 1}, \quad (2.2)$$

and (iv) is cut off at r_{out} . The tenuous envelope is actually neither azimuthally symmetric nor

¹<ftp://cdsarc.u-strasbg.fr/pub/cats/J/A+A/291/943>

²Note that this is not identical to the often-used OH5 opacities, which were calculated for a gas density of 10^6 cm^{-3}

fully spatially recovered by our observations. Therefore, its real size remains unconstrained and r_{out} cannot be considered a reliable source property.

For the temperature profile of an externally heated cloud, we adopt the following empirical prescription. It resembles the radiation transfer equation in coupling the local temperature to the effective optical depth toward the outer “rim”, where the interstellar radiation field (ISRF) impacts:

$$T(r) = T_{\text{out}} - \Delta T \left(1 - e^{-\tau(r)}\right) \quad (2.3)$$

with $\Delta T = T_{\text{out}} - T_{\text{in}}$ and the frequency-averaged effective optical depth

$$\tau(r) = \tau_0 \frac{\int_r^{r_{\text{out}}} n_{\text{H}}(x) dx}{\int_0^{r_{\text{out}}} n_{\text{H}}(x) dx}. \quad (2.4)$$

τ_0 is an empirical (i.e. free) scaling parameter that accounts for the a priori unknown mean dust opacity and the spectral energy distribution of the UV radiation of the ISRF. T_{in} is the minimum, inner temperature, and is determined by IR and cosmic ray heating.

The results of this modeling approach are presented in Sect. 2.4.1. The uncertainties of the method have been discussed thoroughly in Nielbock et al. (2012) and Launhardt et al. (2013). They come to the conclusion that the largest uncertainty (up to a factor 3) in the derived density is introduced by the uncertainty in the dust opacities. Additional uncertainties are introduced by the assumed distances, the gas-to-dust ratio, the symmetry assumption (w.r.t. the plane-of-sky) for the LoS, and the limited angular resolution. In particular in the center of the cores, the density can be systematically underestimated due to beam smoothing. We therefore estimate the overall fitting uncertainty of the derived density maps to be $\pm 25\%$, plus a scaling uncertainty by up to a factor 3 due to the not well-constrained dust opacity model. The accuracy of the dust temperature is not as strongly affected by the aforementioned effects and the modeled dust temperature has an estimated uncertainty of ${}_{-1}^{+2}$ K.

2.3.2 CHEMICAL MODELING

On the basis of the dust temperature and the hydrogen density maps that were derived using the ray-tracing technique and that are presented in Section 2.4.1, we model the chemical evolution of the molecular gas in the cloud cores. The density and temperature profiles are kept constant during the chemical evolution of the cores. The gas is initially atomic comprising 13 elements and evolves with time because of the processes described below. This approach of a chemical evolution at constant physical conditions is often called “pseudo time-dependent”. We call the time span during which the chemical models evolve “chemical age”. How this parameter is

related to the "real" age of the cores is discussed in Sect. 2.4.4.

We act on the assumption that the gas temperature is equal to the dust temperature everywhere in the clouds. This simplifying assumption should hold to first order at hydrogen densities above 10^4 cm^{-3} where dust and gas are collisionally coupled (Galli et al. 2002) and from where most of the molecular emission originates. However, the coupling might not be perfect even in the densest regions of our study ($> 10^6 \text{ cm}^{-3}$). E.g., for B 68, where we have derived a central hydrogen density of $4 \times 10^5 \text{ cm}^{-3}$ and central dust temperature of 8 K, Hotzel et al. (2002) and Lai et al. (2003) find a central gas temperature of 10-11 K from ammonia observations. On the other hand, ammonia might be depleted in the core center such that it rather traces a somewhat warmer inner layer of the envelope. In our model of B 68, the dust temperature in a shell of radius 5000 to 7000 AU is indeed 10-11 K. This could also explain at least part of this small discrepancy. The decoupling of gas and dust temperatures at lower densities affects our modeling results less than the chemical evolution, since the rotational transitions at low densities are subthermally excited. For instance, at a hydrogen density of 10^3 cm^{-3} and a gas temperature of 100 K, the $J = 2 - 1$ transition of CO would only be excited to about 9 K while the same transition would be excited to 5 K at a gas temperature of 20 K³. Therefore, underestimating the gas temperature affects the modeled level populations and the molecular emission at low densities only weakly.

In the vicinity of the core centers, the majority of globules show almost circularly symmetric shapes. As we study these central cloud regions, the modeling is performed assuming 1D radial profiles. We obtain 1D-profiles of the observed molecular emission and the dust temperature and density maps by azimuthally averaging. We cut out the segment of the circle in the direction of asymmetries for the averaging task. The regions which have been taken into account for the derivation of the 1D-profiles are indicated in Figs. 2.11 - 2.17. The resulting profiles of the dust temperature, hydrogen densities and column densities are shown in Fig. 2.1.

We use the time-dependent gas-grain chemical model 'ALCHEMIC' (see Semenov et al. 2010). A brief summary is given below. The chemical network is based on the 2007 version of the OSU network⁴. The reaction rates as of November 2010 are implemented (e.g., from KIDA database⁵). We consider cosmic ray particles (CRP) and CRP-induced secondary UV photons as the only external ionizing sources. We adopt a CRP ionization rate of $\zeta_{\text{CR}} = 1.3 \times 10^{-17} \text{ s}^{-1}$ (Herbst & Klemperer 1973), although recent studies have revealed higher CRP ionization rates in translucent clouds (e.g., Indriolo et al. 2012). The dense molecular cloud cores studied here are embedded in extended envelopes that, despite their low density, effectively scatter the low energy particles of the cosmic rays and thereby reduce the luminosity of the cosmic rays in the shielded regions. Therefore the lower value of Herbst & Klemperer (1973) is expected to hold for dense and shielded clouds (e.g., Garrod 2013; Vasyunin &

³This has been calculated using the on-line version of RADEX (van der Tak et al. 2007)

⁴see: <http://www.physics.ohio-state.edu/~eric/research.html>

⁵<http://kida.obs.u-bordeaux1.fr>

Herbst 2013). The UV dissociation and ionization photo rates are adopted from van Dishoeck et al. (2006)⁶. The self-shielding of H₂ from photodissociation is calculated by Equation (37) from Draine & Bertoldi (1996). The shielding of CO by dust grains, H₂, and its self-shielding are calculated using the precomputed table of Lee et al. (1996 Table 11). As the chemical model does not include carbon isotopologues, the self-shielding factors for ¹²C¹⁸O are calculated by lowering the ¹²C¹⁶O abundances by an appropriate isotopic ratio (see below).

In addition to gas-phase chemistry, the chemical model includes the following gas-grain interaction processes (We refer the reader to Sect. 2.3 in Semenov et al. (2010) for the corresponding equations.). Molecules accrete on and stick to dust grains by physisorption with 100% probability, except of H₂ which is not allowed to stick. Chemisorption of surface molecules is not allowed. The surface molecules are released back to the gas phase by thermal, CRP-, and CRP-induced UV-photodesorption. All these processes are modeled with a first-order kinetics approach (Equation (2) in Semenov et al. (2010)). A UV photodesorption yield for surface species of 10⁻³ is assumed (e.g., Öberg et al. 2009a,b). The grain charging is modeled by dissociative recombination and radiative neutralization of ions on grains, and electron sticking to grains. The synthesis of complex molecules is included, using a set of surface reactions and photoprocessing of ices from Garrod & Herbst (2006). We assume that each 0.1 μm spherical olivine grain provides ≈ 1.88 × 10⁶ surface sites for accreting gaseous species (Biham et al. 2001). The surface recombination proceeds only via the Langmuir-Hinshelwood mechanism. Upon a surface recombination, the reaction products are assumed to remain on the grains. Following Katz et al. (1999), we use the standard rate equation approach to the surface chemistry and do not consider tunneling of H and H₂ through the grain surface. Overall, our chemical network consists of 656 species made of 13 elements, and 7907 reactions. All chemical parameters are kept fixed during the iterative fitting of the observational data. With this model we calculate time-dependent CO and N₂H⁺ abundances and use them for the line radiative transfer modeling and fitting of the observed spectral maps.

In the cloud 1D physical model, the density profiles are cut off at an outer radius where either no density could be derived because the continuum emission is too weak or where the morphology of the cloud becomes asymmetric. These radii are also the outer boundaries for the chemical modeling. At these radii the density has, however, not yet dropped to zero as the cores are further embedded in low-density extended envelopes. We therefore have to take into account that the external UV field is already attenuated at the outer edge of the cores. We derive the extinction level by converting the column density at the outer boundaries to an extinction level A_V . We use a conversion factor A_V/N_H of $1 \times 10^{-21} \text{ cm}^2$. This is the average value estimated by comparing the N_H maps derived from the dust emission to complementary near-infrared extinction maps (see Launhardt et al. 2013; Kainulainen et al. 2006), which will be presented and discussed in more detail in a forthcoming paper.

We want to compare models and observations of ¹³CO, C¹⁸O and N₂H⁺. Since the rare isotopo-

⁶<http://www.strw.leidenuniv.nl/~ewine/photo/>

logues are not explicitly taken into account in the chemical modeling, we proceed in two steps. In the first step, we calculate the chemical model for ^{12}CO to get accurately the N_2H^+ abundances. The modeling itself also consists of two steps. First, the abundance of the molecules and the corresponding shielding factors are calculated using an analytic approximation. The shielding factors are subsequently used for the second step - the full time-dependent modeling. In order to calculate the profiles of ^{13}CO and C^{18}O , we artificially decrease the ^{12}CO abundance by a factor in the analytic approximation and calculate the shielding-factor for these species. They are used for the time-dependent chemical modeling. The initial abundances are however taken to be the same as for the modeling of ^{12}CO . In order to obtain the abundance of the rare isotopologues, the resulting abundances of the time-dependent modeling are divided by the corresponding fraction of these species with respect to their main isotopologue. This approach allows us to take into account the reduced self-shielding of ^{13}CO and C^{18}O with respect to ^{12}CO without extending the chemical network to the rarer isotopologues. In the literature there is a spread of values mentioned for the ratios of the isotopologues. We use a fraction of 1/70 for ^{13}CO with respect to ^{12}CO and 1/490 for C^{18}O (Wilson & Rood 1994; Lodders et al. 2009).

As the temperature and abundances of the molecules vary along the LoS, the molecular emission could be partly subthermally excited or be optically thick. For these reasons, we calculate the rotational level populations and emission of the molecules from the synthetic abundance profiles using line-radiative transfer modeling. It is not our goal to model the kinematics of the cores. For the pure purpose of modeling the lineshape and the total intensity of the transitions, we can neglect variations of macroscopic and turbulent motions in the cores, since they are so weak that this simplification does not affect the results on the molecular abundances. We use the non-LTE line radiative transfer code ‘LIME’ (Brinch & Hogerheijde 2010) and the molecular data files of the “Leiden Atomic and Molecular Database” (Schöier et al. 2005). The LIME code allows to take into account line-broadening due to micro turbulent motions. This is done by setting a scalar Doppler broadening parameter. Since the linewidths in the globules do not vary significantly over the globules, it is possible to set this parameter such that the linewidths of models and observations agree everywhere. The Doppler broadening parameter is taken as one free parameter in the modeling process. Thereby we ensure that the optical depth of the emission is properly taken into account. The macroscopic velocity field in the modeling is set to zero. The velocity channel width is set to the value of the observed spectral cubes and the pixel spacing is set to $10''$ to which all observational data are also regridded.

For the comparison of synthetic and observed spectra, the latter have been prepared as followed. We have removed line shifts from macroscopic motions in the observed spectra as we do not model the kinetics of the cores. For this task, the spectra have been fitted and shifted by the derived v_{LSR} such that the centers of all spectra are located at $v_{\text{LSR}} = 0$. They have also been rebinned such that $v_{\text{LSR}} = 0$ lies in the center of a bin as it is the case for the synthetic spectra. Finally, the spectra are azimuthally averaged. The resulting radially varying spectra build up the reference to which the modeled spectra can be compared directly.

During the course of the modeling, we vary four parameters. The chemical model has only one "true" free parameter: the chemical age, which is the time during which the gas evolves at constant physical conditions. In addition, we take into account uncertainties in the derived hydrogen densities of up to a factor 3 resulting from the uncertainties of the assumed dust properties (see Sect. 2.3.1). The relative initial abundances of the atomic species are kept constant when the hydrogen density is varied. We also need to take into account that the hydrogen density has not dropped to zero at the outer boundaries of the model cores. Halos of dust particles around the globules with a mean extinction A_V of typically 1-3 mag are detected in the SPIRE as well as NIR extinction maps that are quite extended. Since these envelopes shield the globules from the UV-part of the ISRF, they need to be considered in the chemical modeling. The halos are not strictly spherically symmetric, neither in extinction / column density, nor in extent, as was pointed out in [Launhardt et al. \(2013\)](#). In order to account for this and other uncertainties discussed in Sect. 2.4.4, we consider the measured mean envelope extinction as a starting guess only and vary them during the modeling procedure.

We find the best model in the following way. The relative differences of observed and synthetic spectra are summed up for each velocity bin and at all radii. The model with the lowest value of this sum is taken as best model. It reproduces not only the integrated emission well, but also the line shape such that the optical depth of the emission is taken into account properly.

2.4 RESULTS & DISCUSSION

2.4.1 DUST TEMPERATURE AND DENSITY MAPS

The final parameters of the hydrogen number density and dust temperature profiles in the cores according to the formulae given in Sect. 2.3.1 are listed in Table 2.3. In Figs. 2.18 - 2.24 we show the hydrogen density and dust temperature maps of all globules in the mid-plane across the sky as they were obtained from the continuum data with the ray-tracing technique described in Sect. 2.3.1. The central density of the starless cores ranges from $4 \times 10^4 \text{ cm}^{-3}$ to $4 \times 10^5 \text{ cm}^{-3}$. The cores are clearly non-isothermal as already predicted by radiative transfer models (e.g., [Evans et al. 2001](#)). In all cores the dust temperature drops from the outer rims with 13-19 K to the core centers to 8-13 K. Compared to the temperatures derived from the modified black-body fitting technique in [Launhardt et al. \(2013\)](#), the central temperatures are lower by 1-3 K. The central column densities reach from 7×10^{21} to $6 \times 10^{22} \text{ cm}^{-2}$ in the maps derived with the ray tracing technique compared to the column densities of 7.5×10^{21} to $4.6 \times 10^{22} \text{ cm}^{-2}$ in [Launhardt et al. \(2013\)](#) which is in average 60% more. The lowest difference is found in the case of CB 17 with an increase of only 6% and the highest in the case of B 68 with an increase of 230%.

From the maps we have derived one-dimensional profiles by azimuthally averaging around the

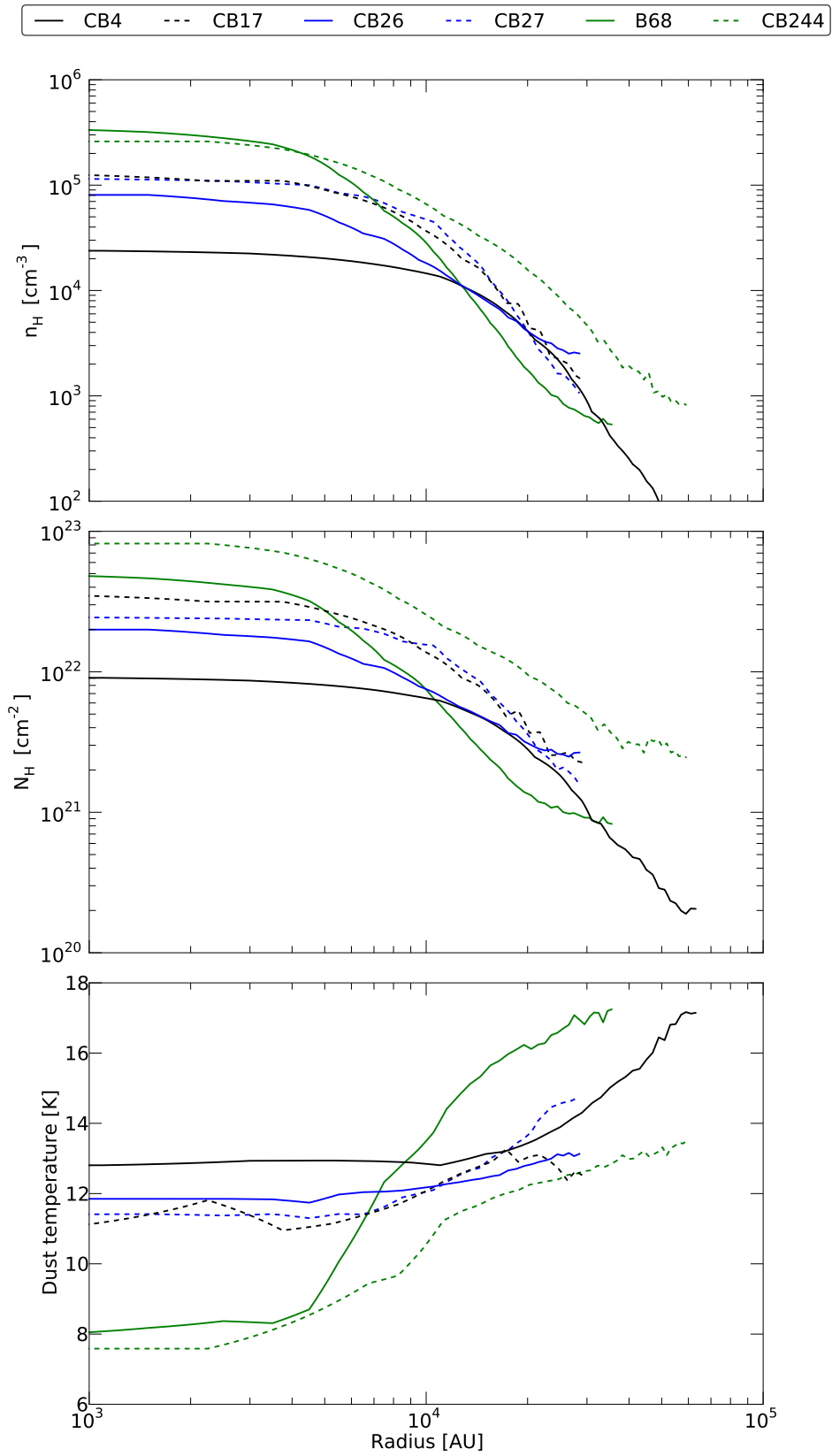


Figure 2.1: Azimuthally averaged profiles of the hydrogen density (top), hydrogen column density (center) and dust temperature (bottom) derived with the ray-tracing technique.

Table 2.3: Parameters of the hydrogen density and dust temperature profiles corresponding to Equations (3.1) - (2.4)

Source	N_0^a [cm ⁻²]	n_0^a [cm ⁻³]	n_{out} [10 ² cm ⁻³]	η^b	r_0 [10 ⁴ AU]	r_1 [10 ⁴ AU]	r_{out} [10 ⁴ AU]	T_{in}^c [K]	T_{out}^c [K]
CB 4	9.2×10^{21}	2.5×10^4	1	5.0	2.0	5.7	8	13.1	19
CB 17 ^d	3.0×10^{22}	1.3×10^5	6	5.0	1.1	3.0	4	10.5	13
CB 26	2.0×10^{22}	8.7×10^4	5	3.0	0.8	4.4	3	12.0	14
CB 27	2.7×10^{22}	1.3×10^5	7	6.0	1.3	6.6	3	11.3	14
B 68 ^d	5.5×10^{22}	4.0×10^5	4	5.0	0.7	2.7	5	8.1	17
CB 244	9.1×10^{22}	2.5×10^5	7	4.0	1.1	4.7	7	8.4	14

Notes. ^(a) The estimated relative uncertainty is $\pm 25\%$, plus a scaling uncertainty by up to a factor of 3 due to the not well-constrained dust opacity model (see uncertainty discussion in Sect. 3.1.). ^(b) The estimated uncertainty is ± 1 . ^(c) The estimated uncertainty is ± 1 K. The temperature estimate is less affected by the dust model (see Launhardt et al. 2013). ^(d) Slight differences to the values derived by Schmalzl et al. (submitted to A&A) and Nielbock et al. (2012) can be accounted to the uncertainties discussed in Sect. 3.1.).

centers of the starless cores. The regions which were taken into account for the derivation of the radial profiles are indicated with thick white lines in the *SPIRE* 250 μm maps in Figs. 2.11-2.17. Because of its strong asymmetry and the nearby protostellar core, the starless core in CB 130 is not well-suited for a 1D study. We therefore do not derive a radial profile of its density and temperature structure and will also not take it into account for the chemical modeling. The profiles of the hydrogen volume and column density, and dust temperature of the other globules are plotted in Fig.2.1.

2.4.2 SIZES, MASSES, AND STABILITY OF THE CORES.

We derived masses of the starless cores by integrating over the circularized 1D hydrogen density profiles $n_H(r)$. We conservatively estimate the mass by choosing r_1 (Eq. 3.2) as outer radii of the cores where the profiles turn from a power-law like into a flat shape. These radii range from 27×10^3 to 57×10^3 AU and are listed in Table 2.3. We take into account that the total gas mass is higher by a factor of $\mu_H = 1.36$ than the hydrogen atom mass so that the core masses are given by:

$$M_{\text{core}} = M(r_1) = \mu_H m_H \times 4\pi \int_0^{r_1} n_H(r) r^2 dr \quad (2.5)$$

The resulting core masses range from 2 M_\odot to 10 M_\odot (see Fig. 2.2) and are well in agreement with those previously estimated from modified black-body fits (see Stutz et al. 2010; Launhardt et al. 2013).

The stability of the cores was checked by comparing the gravitational potential with the thermal energy of the particles in the cores. We neglected turbulent pressure, rotational energy and

magnetic fields. This is justified since the thermal energy is the strongest contributor to the stabilization. Assuming typical magnetic field strengths in Bok globules of a few $100\ \mu\text{G}$ (Wolf et al. 2003), these three contributions are dominated by the turbulent pressure which we have estimated for all cores and typically adds only 10% to the thermal energy.

We estimated the gravitational potential by

$$E_{\text{grav}} = -4\pi G m_{\text{H}} \mu_{\text{H}} \int_0^{r_1} M(r) n_{\text{H}}(r) r dr \quad (2.6)$$

where G is the gravitational constant. The thermal energy of the molecules is calculated from

$$E_{\text{therm}} = \frac{3k_{\text{B}}\mu_{\text{H}}}{2\mu} 4\pi \int_0^{r_1} T(r) n_{\text{H}}(r) r^2 dr \quad (2.7)$$

where k_{B} is the Boltzmann constant and $\mu_{\text{H}} n_{\text{H}}/\mu$ with $\mu/\mu_{\text{H}} = 0.6$ the mean particle density for molecular gas. For the gas temperature, we adopt the dust temperature. T_{Gas} might actually be higher than T_{Dust} in the outer regions of the envelopes, so that we probably underestimate E_{therm} .

In the top panel of Fig. 2.2, we plot the ratio of the total gravitational to thermal energy of all starless cores against their masses. The dashed horizontal line at a ratio of 2 indicates virial equilibrium while the dashed line at a ratio of 1 marks the bounding limit. The values for the cores indicate that only the starless core of CB 244 is clearly gravitationally unstable. In Fig. 2.2 (bottom) we plot the central density against the total mass of the cores. The dashed line indicates the maximum central density of a pressure-supported, self-gravitating modified (non-isothermal) Bonnor-Ebert sphere (BES; Bonnor 1956; Ebert 1955), calculated by Keto & Caselli (2008) for a core with photoelectric heating at the boundary. The comparison of the core properties to the theoretical curve strengthens the result that the starless core in CB 244 is prestellar. It also suggests that CB 17, CB 27, and B 68 are thermally super critical.

2.4.3 SPECTRA AND MOLECULAR EMISSION MAPS

In Figs. 2.11-2.17, integrated emission maps of ^{12}CO (J=2-1), ^{13}CO (J=2-1), C^{18}O (J=2-1) and N_2H^+ (J=1-0) are presented. For the sake of comparison we also have included maps showing the same regions as observed with the SPIRE bolometer in the $250\ \mu\text{m}$ band and from the Digitized Sky Survey 2 archive⁷. Because of their different abundances, the emission of three isotopologues becomes optically thick at different column-densities. ^{12}CO as the main CO isotope traces the envelopes of the globules particularly well, while ^{13}CO is best suited to trace the outer parts of the cores. C^{18}O as the rarest isotope traces the dense regions of the cores up to hydrogen densities of $\sim 1 \times 10^5\ \text{cm}^{-3}$. At these densities CO freezes out onto the

⁷http://archive.stsci.edu/cgi-bin/dss_form

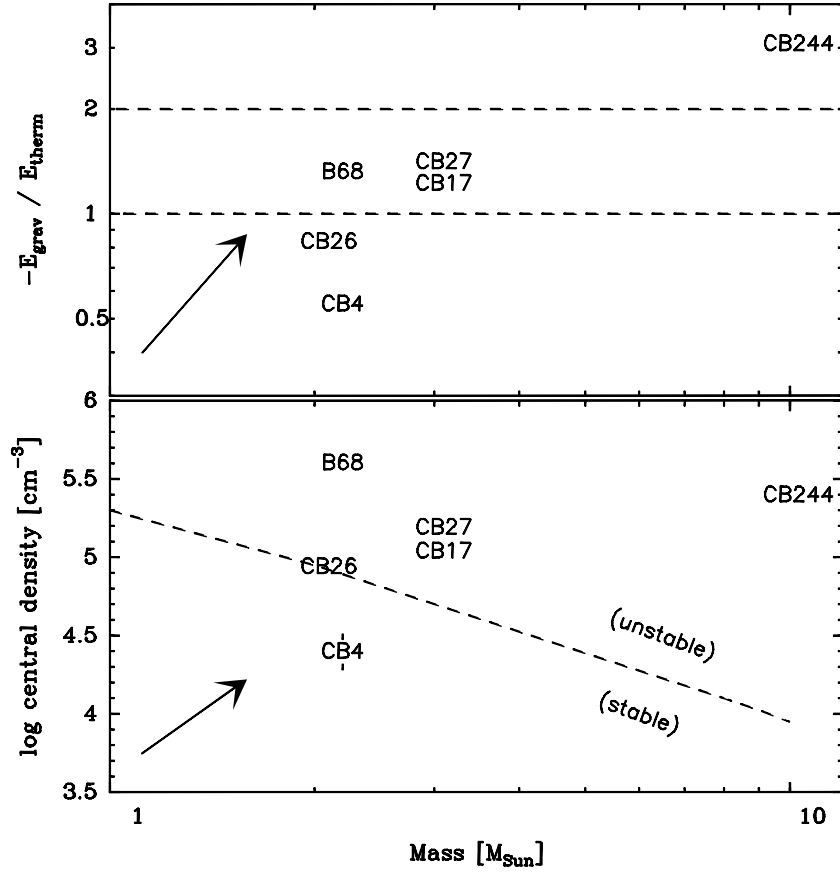


Figure 2.2: Stability of the cores. Same plot as Fig. 6 in Launhardt et al. (2013), but here for the results of the ray-tracing models. *Top:* ratio of gravitational potential to thermal kinetic energy vs. total gas mass (M_{core}). The lower dashed horizontal line marks the bounding limit of $-E_{\text{grav}}/E_{\text{therm}} = 1$, while the upper line marks the state of virialization at $-E_{\text{grav}}/E_{\text{therm}} = 2$. *Bottom:* Central density vs. total gas mass for the same cores. The dashed line marks the maximum stable density of a pressure-supported, self-gravitating modified (non isothermal) BES as calculated by Keto & Caselli (2008 their Fig. 14, model with photoelectric heating at the core boundary taken into account). The uncertainty resulting from the ray-tracing modeling is indicated by the error bars at CB 4. The arrows indicate the maximum systematic shift of the cores in the diagram if grain properties of ISM dust would be used in the modeling.

Table 2.4: Spectral line parameters at the centers of the starless cores

Source	Line	Δv_{chann} [m/s]	$v_{\text{LSR}}^{(a,b)}$ [km/s]	$T_{\text{mb}}^{\text{peak}(a,b)}$ [K]	$\Delta T_{\text{mb}}^{\text{RMS}}$ [K]	$\Delta v_{\text{FWHM}}^{(a,b)}$ [km/s]	$\Delta v_{\text{therm}}^{(c)}$ [km/s]	$\Delta v_{\text{non-therm}}^{(d)}$ [km/s]	$I_{\text{line}}^{(e)}$ [K.km/s]
CB 4	$^{12}\text{CO}(2-1)$	0.325	-11.423 ± 0.002	13.3 ± 0.3	0.11	0.510 ± 0.007	0.15	0.49 ± 0.01 (7.7)	7.8 ± 0.6
	$^{13}\text{CO}(2-1)$	0.34	-11.35 ± 0.01	7.3 ± 0.6	0.22	0.45 ± 0.02	0.15	0.42 ± 0.03 (6.6)	4.4 ± 0.3
	$\text{C}^{18}\text{O}(2-1)$	0.053	-11.442 ± 0.004	3.5 ± 0.3	0.15	0.19 ± 0.01	0.15	0.12 ± 0.04 (1.9)	0.73 ± 0.04
	$\text{N}_2\text{H}^+(1-0)$	0.063	-11.355 ± 0.005	0.47 ± 0.09	0.09	0.17 ± 0.02	0.15	0.08 ± 0.08 (1.3)	0.38 ± 0.08
CB 17	$^{12}\text{CO}(2-1)$	0.325	-4.74 ± 0.01	9.7 ± 0.5	0.15	0.97 ± 0.03	0.14	0.96 ± 0.03 (16.1)	12.8 ± 0.8
	$^{13}\text{CO}(2-1)$	0.34	-4.70 ± 0.01	6.2 ± 0.4	0.19	0.71 ± 0.03	0.14	0.70 ± 0.03 (11.8)	2.5 ± 0.4
	$\text{C}^{18}\text{O}(2-1)$	0.053	-4.764 ± 0.004	2.4 ± 0.1	0.07	0.45 ± 0.01	0.13	0.43 ± 0.02 (7.8)	1.2
	$\text{N}_2\text{H}^+(1-0)$	0.063	-4.630 ± 0.001	1.5 ± 0.2	0.19	0.325 ± 0.002	0.14	0.29 ± 0.01 (4.9)	3.0
CB 26	$^{12}\text{CO}(2-1)$	0.325	+5.590 ± 0.007	3.6 ± 0.1	0.08	1.17 ± 0.02	0.14	1.16 ± 0.02 (19.5)	6.3 ± 0.3
	$^{13}\text{CO}(2-1)$	0.34	+5.64 ± 0.01	2.7 ± 0.2	0.14	1.01 ± 0.03	0.14	1.00 ± 0.03 (16.8)	2.3 ± 0.5
	$\text{C}^{18}\text{O}(2-1)$	0.053	+5.60 ± 0.02	1.1 ± 0.1	0.15	0.70 ± 0.04 ^(f)	0.14	0.69 ± 0.04 (11.6)	0.73 ± 0.09
	$\text{N}_2\text{H}^+(1-0)$	0.063	^(g)	^(g)	0.08	^(g)	^(g)	^(g)	0.4 ± 0.1
CB 27	$^{12}\text{CO}(2-1)$	0.325	+7.127 ± 0.005	4.1 ± 0.1	0.08	0.89 ± 0.01	0.14	0.88 ± 0.01 (14.8)	4.4 ± 0.2
	$^{13}\text{CO}(2-1)$	0.34	+7.14 ± 0.02	3.4 ± 0.05	0.10	0.61 ± 0.05	0.14	0.59 ± 0.06 (9.9)	2.2 ± 0.3
	$\text{C}^{18}\text{O}(2-1)$	0.053	+7.058 ± 0.005	3.0 ± 0.2	0.16	0.24 ± 0.01	0.13	0.20 ± 0.02 (3.4)	0.78 ± 0.06
	$\text{N}_2\text{H}^+(1-0)$	0.063	+7.104 ± 0.001	2.1 ± 0.08	0.08	0.187 ± 0.004	0.14	0.12 ± 0.03 (2.0)	2.15 ± 0.07
B 68	$^{12}\text{CO}(2-1)$	0.325	+3.30 ± 0.01	5.9 ± 0.4	0.16	0.63 ± 0.02	0.14	0.61 ± 0.03 (10.3)	4.4 ± 0.3
	$^{13}\text{CO}(2-1)$	0.34	+3.35 ± 0.01	3.1 ± 0.5	0.12	0.51 ± 0.05	0.14	0.49 ± 0.06 (8.2)	1.8 ± 0.3
	$\text{C}^{18}\text{O}(2-1)$	0.030	+3.292 ± 0.001	2.10 ± 0.02	0.02	0.200 ± 0.001	0.14	0.14 ± 0.02 (2.4)	0.45 ± 0.04
	$\text{N}_2\text{H}^+(1-0)$	0.063	+3.347 ± 0.001	0.88 ± 0.01	0.01	0.249 ± 0.003	0.14	0.21 ± 0.02 (3.5)	1.5 ± 0.04
CB 130	$^{12}\text{CO}(2-1)$	0.051	^(h)	2.3 ⁽ⁱ⁾	0.08	4.2 ^(j)	0.14	..	11.6 ± 0.1
	$^{13}\text{CO}(2-1)$	0.053	+7.60 ± 0.01	1.2 ± 0.1	0.07	1.26 ± 0.04 ^(f)	0.14	1.25 ± 0.04 (21.0)	1.8 ± 0.1
	$\text{C}^{18}\text{O}(2-1)$	0.053	+7.524 ± 0.006	0.96 ± 0.05	0.05	0.48 ± 0.01	0.14	0.46 ± 0.02 (7.7)	0.52 ± 0.03
	$\text{N}_2\text{H}^+(1-0)$	0.063	+7.514 ± 0.002	1.34 ± 0.04	0.04	0.397 ± 0.005	0.14	0.37 ± 0.01 (6.2)	3.2 ± 0.05
CB 244	$^{12}\text{CO}(2-1)$	0.325	+3.407 ± 0.008	4.2 ± 0.1	0.05	1.62 ± 0.02	0.13	1.61 ± 0.02 (29.2)	7.5 ± 0.5
	$^{13}\text{CO}(2-1)$	0.34	+3.86 ± 0.01	2.5 ± 0.1	0.07	0.98 ± 0.03	0.13	0.97 ± 0.03 (17.6)	2.7 ± 0.2
	$\text{C}^{18}\text{O}(2-1)$	0.053	+3.805 ± 0.007	3.0 ± 0.2	0.19	0.43 ± 0.02	0.13	0.41 ± 0.03 (7.4)	1.2 ± 0.1
	$\text{N}_2\text{H}^+(1-0)$	0.063	+3.875 ± 0.002	1.90 ± 0.08	0.08	0.34 ± 0.005	0.13	0.31 ± 0.01 (5.6)	4.6 ± 0.2

Notes. ^(a) for the CO isotopologues determined from Gaussian fits, for N_2H^+ determined from fits of the hyperfine structure, ^(b) for N_2H^+ of the main line at 93173.777 MHz, ^(c) assuming a constant gas temperature along the LoS which is equal to the dust temperature derived from modified black body fitting. We estimate an uncertainty 0.02km/s, ^(d) in brackets the same value in terms of the isothermal sound speed, ^(e) Determined by integrating of the spectra (in the case of N_2H^+ all components), ^(f) This line is double peaked. The linewidth given here, is even so given for a Gaussian fitted to the full spectrum, ^(g) not detected, ^(h) not determinable, ⁽ⁱ⁾ not fit with a Gaussian. Peak value taken directly from the spectrum., ^(j) not fit with a Gaussian. Width of spectrum where $T_{\text{mb}} > 0.5T_{\text{mb}}^{\text{peak}}$.

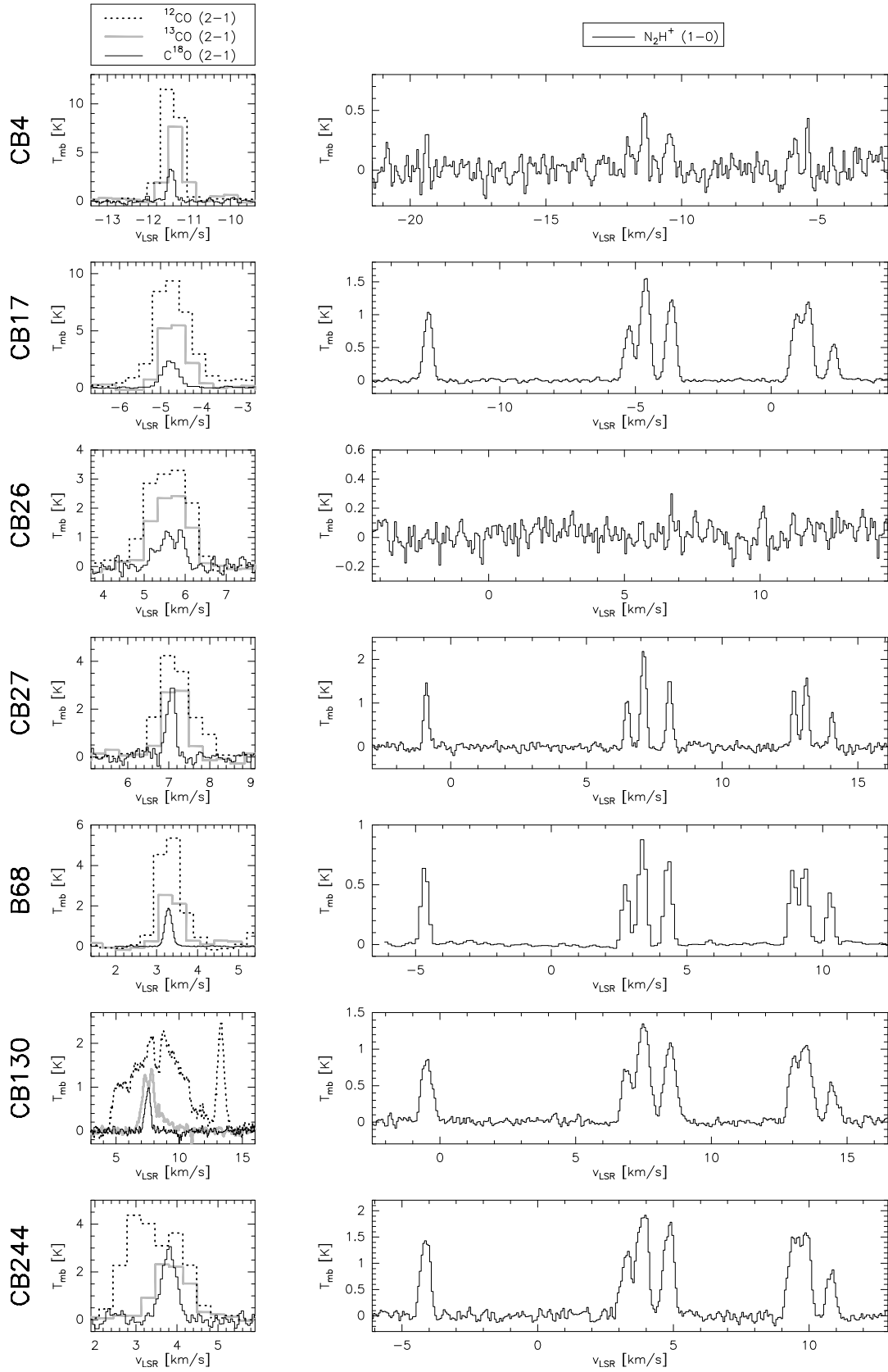


Figure 2.3: Spectra of the ^{12}CO (2-1), ^{13}CO (2-1), C^{18}O (2-1) and N_2H^+ (1-0) transitions in a $36.4''$ HPB at the centers of the starless cores.

dust grains. We therefore complemented our set of molecular line observations with maps of N_2H^+ , which traces the densest parts of the cores where CO is frozen out. The time-scales of build-up and depletion of N_2H^+ are longer than for CO so that both species in combination allow to constrain the ages of the cores.

The ^{12}CO and ^{13}CO maps are smaller than the *SPIRE* $250\ \mu\text{m}$ maps, but the molecular emission of ^{12}CO is more extended than the continuum emission in some cases. This indicates the existence of extended cold envelopes to which the continuum observations are less sensitive. C^{18}O is the least abundant CO isotopologue used in this study. It is therefore the optically thinnest and best suited CO isotopologue for the dense regions of the cores where CO is not frozen out. While its emission is enhanced at the positions of some Class I objects, it does not show enhancement at the locations of the starless cores. In contrast, the N_2H^+ emission shows a positive gradient towards the core centers. In the two least dense starless cores, CB 4 and CB 26, N_2H^+ emission was only marginally detected.

The spectral line parameters at the centers of the starless cores are listed in Table 2.4. The spectra of all molecules toward the centers of the starless cores are also plotted in Fig. 2.3. C^{18}O is single-peaked in all sources except CB 26, where two distinct peaks at a velocity separation of 0.33 km/s are observed. It is unlikely, that the dip is due to self-absorption, since the line is quite weak. It is more likely caused by multiple velocity components. Almost no N_2H^+ emission is detected from the starless core in CB 26. At the position of the protostar in CB 26, the C^{18}O line is also double peaked, with the dip at the same velocity as for the starless core. This is an indication of the edge-on seen protoplanetary disk (Launhardt & Sargent 2001). The peak main beam temperature T_{MB} of the C^{18}O ($J = 1 - 0$) transition ranges from 2 to 6 K in the various globules.

The channel-width of the ^{13}CO observations is only 0.34 km/s compared to 0.05 km/s of the C^{18}O spectra. If the ^{13}CO line of CB 26 was double peaked as the C^{18}O line, we could not resolve it. The ^{13}CO line is single peaked in all cores except for CB 130 where it shows two peaks with a velocity separation of 0.53 km/s. The dip of this line falls into the peak of the C^{18}O emission and is thus probably a result of self-absorption.

The emission of the main isotopologue ^{12}CO is optically thick towards the core centers but traces also the outskirts of the globules where the emission of the less abundant isotopes drops below the detection limit. Consequently, its linewidth is highest throughout the sample and ranges from 0.3 km/s to 0.7 km/s in the globules which only contain starless cores. In those globules which also inhabit proto-stellar cores, the linewidths are generally higher and reach values of up to 1.6 km/s. CB 130 is an exceptional case with a very broad line emission, consistent with its location within a larger diffuse structure.

All globules show signs of slow large-scale motions. The linewidths are typically larger than the thermal linewidths and increase from the rare to the abundant CO isotopologues. The average linewidths of the spectra toward the core centers are 0.30 km/s, 0.69 km/s and 1.0 km/s

for C^{18}O , ^{13}CO , and ^{12}CO respectively. The thermal linewidths are typically around 0.15 km/s, if one assumes that the gas temperature is equal to the dust temperature. The radiation of ^{13}CO and ^{12}CO emanate mainly from regions with $n_{\text{H}} \lesssim 10^4 \text{ cm}^{-3}$ where the gas is expected to be warmer than the dust, since the density is too low to couple both temperatures via collisions. Therefore, a fraction of the linewidth increase can be attributed to higher gas temperatures at the outskirts of the globules. Gas temperatures of 30 K to 50 K would, however, only result in a thermal line-broadening of 0.22 km/s to 0.29 km/s, respectively. The remaining broadening must be caused by turbulent or macroscopic motions, but is partly also mimicked by the optical thickness of the lines.

With the N_2H^+ observations we trace the inner part ($r \lesssim 10^4 \text{ AU}$) of the cores where large amounts of CO are expected to be frozen out onto the dust grains. The spectra at the position of the core centers are shown in Fig. 2.3 (right panels). The linewidths range from 0.08 km/s up to 0.37 km/s. This range can only partially result from different temperatures and must have its origin in the different dynamics of the gas.

2.4.4 CORE PROPERTIES CONSTRAINED FROM CHEMICAL MODELING

On the basis of the dust temperature and hydrogen density profiles presented in Sect. 2.4.1, we have modeled the chemical evolution of the globules. The approach is explained in Sect. 2.3.2. The best fits of the modeled integrated emission to the observed profiles are presented in Fig. 2.4. In Fig. 2.5, we demonstrate the quality of the agreement between modeled and observed line shapes.

THE INDIVIDUAL GLOBULES

CB 4: While CB 4 is the most symmetric and isolated globule of our study (Fig. 2.11), it is also the least dense one with a central hydrogen density of only $4 \times 10^4 \text{ cm}^{-3}$. It is the only core in the study for which the modeled ^{13}CO emission is underestimated with all parameter sets. Due to its low density the coupling of gas and dust temperature is expected to be the weakest in this globule and the gas temperature might thus be significantly higher than the dust temperature. The emission of C^{18}O and N_2H^+ is dominated by inner regions such that the gas temperature is closer to the dust temperature. We find that the chemical age of CB 4 is $\sim 10^5 \text{ yr}$. The significance of the derived chemical ages is discussed in Sect. 2.4.4. In order to match the observations, we have to increase the hydrogen density by a factor of 3. We require $A_{V, \text{out}}$ to be set at a value of at least 4 mag, while from the NIR extinction maps a value of 0.6 mag has been derived.

CB 17: The ^{13}CO emission of CB 17 can be reproduced assuming a chemical age of $7 \times 10^4 - 10^5 \text{ yr}$ and that the hydrogen density is increased by a factor of 3. We only have a very small

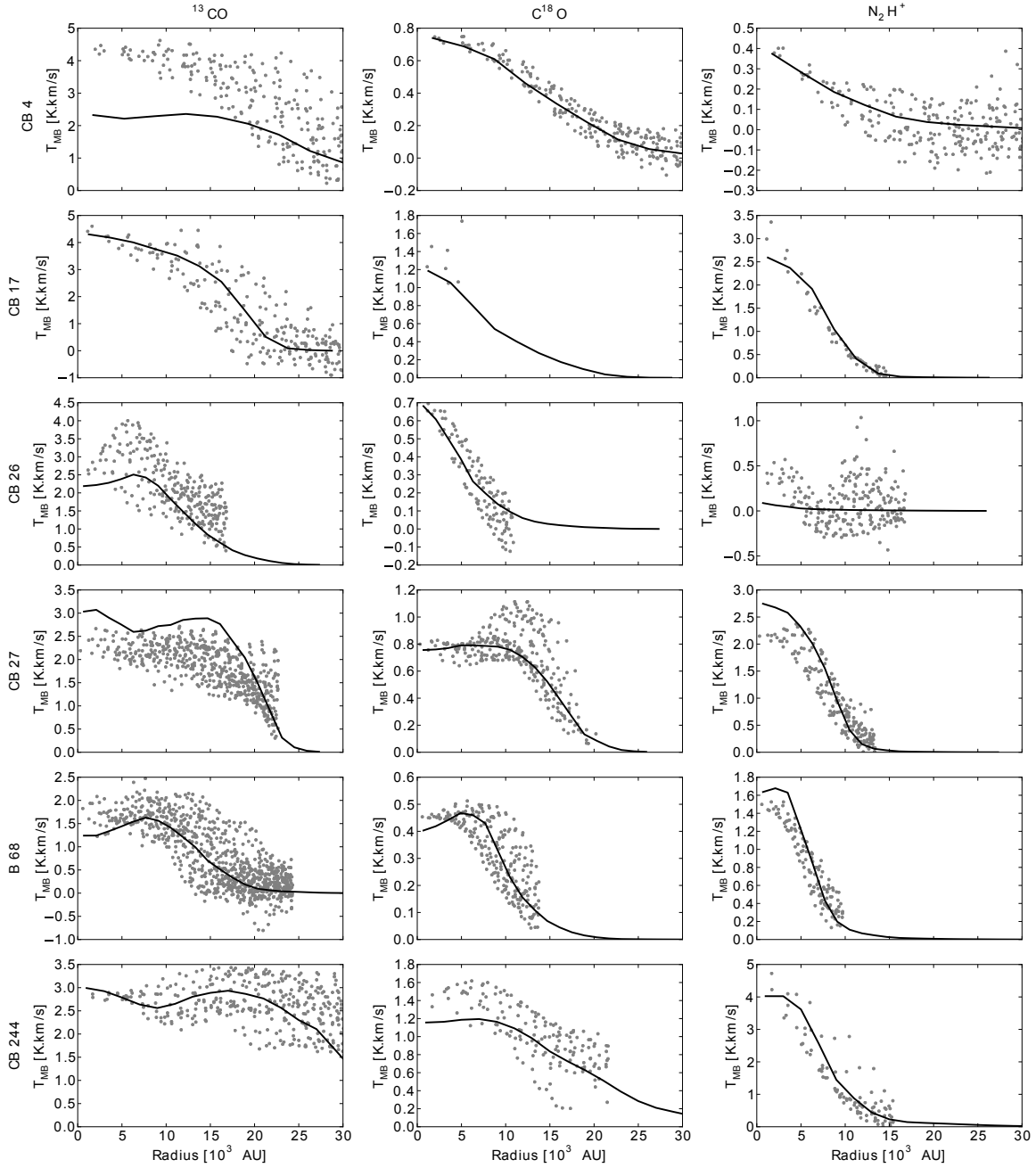


Figure 2.4: Profiles of the integrated emission that would result from the molecular abundances of the final models (solid line) compared to the observed profiles of the integrated emission for all modeled starless cores. (Left) ^{13}CO ($J=2-1$), (center) C^{18}O ($J=2-1$), (right) N_2H^+ ($J=1-0$).

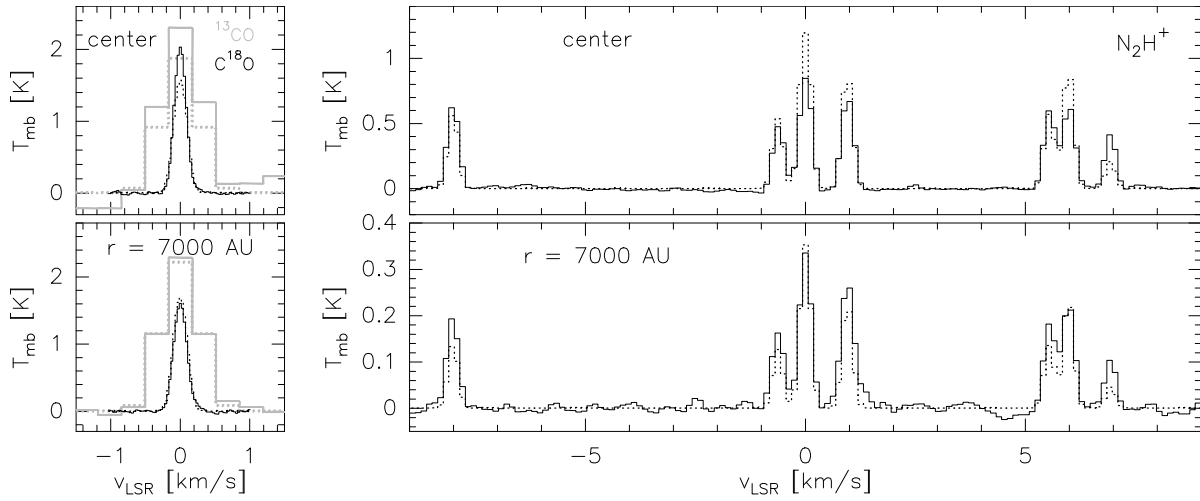


Figure 2.5: To quantify the agreement of models and observations we compare the spectra over the full radius of the models. Here, an example of B 68 is shown. The solid lines represent observations, the dotted lines the synthetic spectra of the best models. On the left hand side, we show the spectra of the ^{13}CO ($J=2-1$) (grey) and C^{18}O ($J=2-1$) (black) transitions. On the right hand side, we show the spectra of the N_2H^+ ($J=1-0$) transition. The top line shows the spectra at the position of the core center, the bottom line the spectra at a radial distance of 7000 AU.

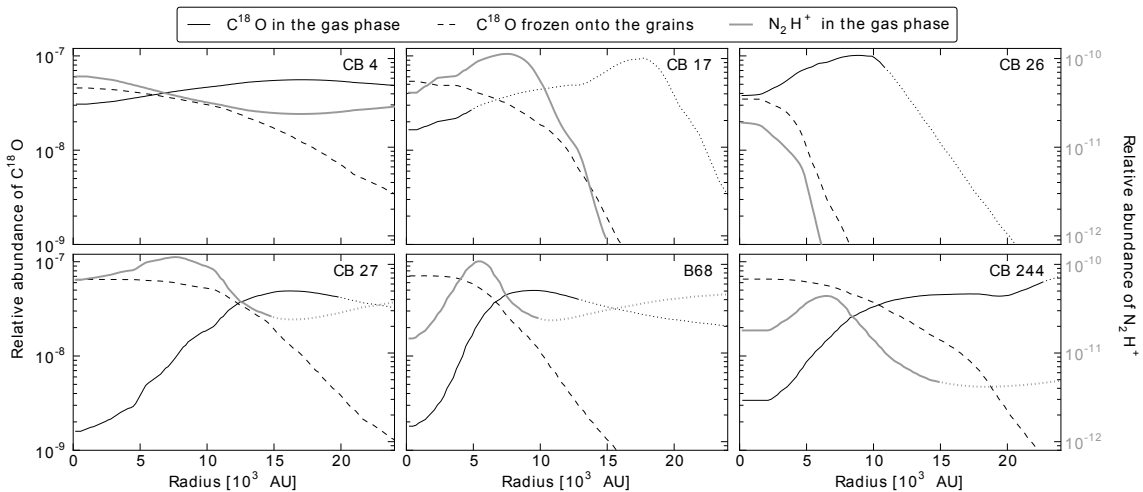


Figure 2.6: Relative abundances (absolute molecular density with respect to the hydrogen density) of gaseous C^{18}O (black solid line), frozen-out C^{18}O (dashed black line) and gaseous N_2H^+ (grey solid line) in the final models. At the outer radii of the emission profiles derived from the observations, the lines turn from a solid into a dotted line shape, indicating that these parts of the profiles are not constrained by observations.

map of C^{18}O emission for this source, such that the observational constraint to the model is limited. We find the best fit for an age of $5 \times 10^4 - 10^5$ yr. The best model for N_2H^+ is found at a chemical age of 10^5 yr. We find the best fits for an external visual extinction of 2 mag which is also found from the NIR extinction mapping, but the deviation is not strong for $A_{V, \text{out}}$ values ranging from 0 to 6 mag. Our finding of a low chemical age does not confirm the finding of Pavlyuchenkov et al. (2006) who found a chemical age of 2 Myr for the starless core in CB 17.

CB 26: We reproduce the ^{13}CO emission from the starless core in CB 26 with a chemical age of 4×10^5 yr. The emission profile of C^{18}O , however, is very steep and shows no signatures of freeze-out. It is best described with chemical models at an age of only $\sim 10^4$ yr and by setting the external visual extinction at the model boundary to 0 ($A_{V, \text{out}} = 1$ in the NIR extinction map). The parameters are consistent with the very weak observed emission of N_2H^+ .

CB 27: The ^{13}CO emission of CB 27 cannot be fit well. In particular the emission coming from large radii is underestimated in all our models. This discrepancy can be overcome, if an increased gas temperature in the envelope of this core is assumed. The range of chemical ages, for which the models fit the data similarly well within the uncertainties, is large and reaches from 10^5 to 10^6 yr. For the C^{18}O emission we find the best models at $A_{V, \text{out}}$ values ranging from 2 to 6 mag ($A_{V, \text{out}} = 1$ has been found in the NIR-extinction map), and an age between 5×10^4 and 10^5 yr. The hydrogen density needs to be multiplied by a factor of 3 with respect to the density profiles obtained from the EPoS project. The N_2H^+ emission is modeled best with the same age as the C^{18}O emission but only a factor 2 in density.

B 68: This is the only core for which all three molecular emission profiles can be reproduced from our chemical models with the hydrogen density profile as derived in Sect. 2.4.1. If we increase the hydrogen density in the models, the resulting molecular emission profiles deviate significantly from the observed profiles. The best chemical age to match the ^{13}CO observations is 2×10^5 yr, while we find that the C^{18}O and N_2H^+ profiles are best explained by models with a chemical age between 7×10^4 and 10^5 yr. Bergin et al. (2006) found an chemical age of $\sim 10^5$ yr from chemical modeling and a comparison of the modeled and observed ^{13}CO and C^{18}O emission. This is well in agreement with our findings. $A_{V, \text{out}}$ needs to be around 4 - 6 mag in the models while we derived a value of about 1 mag from the NIR extinction map.

CB 244: As for CB 27, all our models underestimate the ^{13}CO emission at large radii, which could be explained by a decoupling of dust and gas temperatures at low densities. The chemical age which fits the data best is around 2×10^5 yr. In contrast, the C^{18}O and N_2H^+ profiles are best fit with a chemical age of only 4×10^4 yr. Changing the external A_V at the model boundaries does not have significant impact on the goodness of the fits. The hydrogen density needs to be multiplied by 2 for the CO isotopologues and by a factor of 3 for N_2H^+ .

The fact that we obtain a discrepancy of the order of a factor $\sim 2-3$ is an indication that the assumed dust model may be incorrect. This result will be discussed in Sect. 2.4.4.

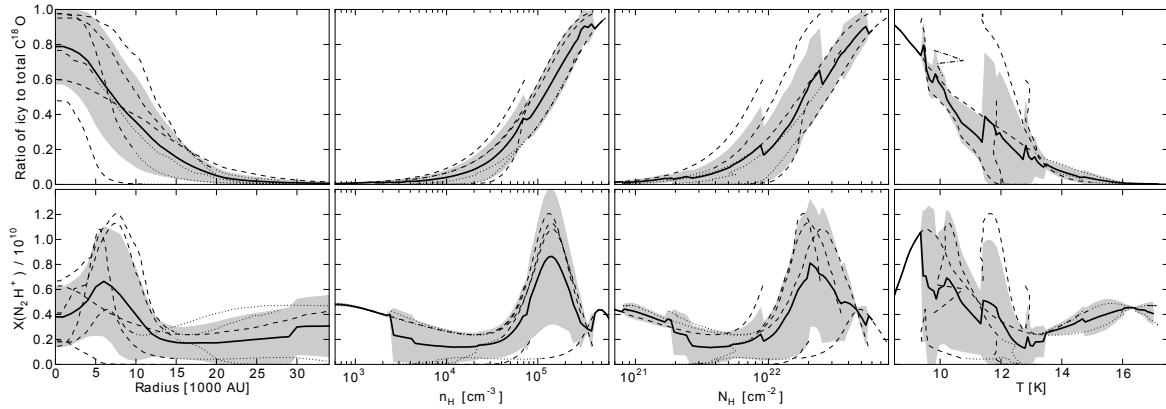


Figure 2.7: *Top row:* The ratio of icy to total C^{18}O abundance of the best-fit models is plotted against the core radius, the hydrogen number density, the column-density, and the dust temperature. *Bottom row:* The N_2H^+ abundance (relative to the hydrogen density) is plotted against the same quantities. The dashed lines indicate the results of the individual globules. Where the models cannot be compared to observations (because the line radiation is too weak), the dashed lines turn over into dotted lines. The bold solid lines mark the mean values. The grey area indicates one standard deviation.

Table 2.5: Ratio of icy to total C^{18}O abundance in the core centers, radius, hydrogen column density, hydrogen density, and dust temperature at which 50% of the total C^{18}O abundance is frozen onto the grains.

	$X(\text{sC}^{18}\text{O})/$ $X(\text{C}^{18}\text{O})$ [%]	$R(50\%)$ [AU]	$N_{\text{H}}(50\%)$ [cm^{-2}]	$n_{\text{H}}(50\%)$ [cm^{-3}]	$T_{\text{D}}(50\%)$ [K]
CB 4	60	6,000	7.7×10^{21}	5.7×10^4	12.9
CB 17	77	9,000	1.6×10^{22}	1.5×10^5	11.1
CB 26	48
CB 27	98	12,000	1.1×10^{22}	8.2×10^4	12.5
B 68	98	7,000	1.8×10^{22}	8.9×10^4	10.5
CB 244	95	10,000	2.8×10^{22}	1.6×10^5	9.8

CO ABUNDANCES

In Fig. 2.6, we plot the modeled relative abundance profiles of gaseous and frozen C^{18}O of the final models that correspond to the emission profiles presented in Fig. 2.4. The abundance of gaseous C^{18}O ($X(\text{C}^{18}\text{O}) \equiv n(\text{C}^{18}\text{O})/n_{\text{H}}$) in molecular gas that is assumed to be well shielded and undepleted varies in the literature and ranges from 3.5×10^{-8} (Tafalla & Santiago 2004) to 2.4×10^{-7} (Lee et al. 2003). In the outer parts of all our cores the C^{18}O abundances $X(\text{C}^{18}\text{O})$ reach the value of Tafalla & Santiago (2004). The highest abundance of 9×10^{-8} is reached in the envelope of the young and not that dense core CB 26. The hydrogen densities in the regions of maximum C^{18}O abundances are typically between 10^4 and $5 \times 10^4 \text{ cm}^{-3}$. In the center of the cores, the gaseous C^{18}O abundance drops because of freezeout onto the dust grains. There, the C^{18}O abundance (relative to the peak abundance) drops by a factor of 2 in the least dense core (CB 4) and by a factor of 30 in the denser cores (CB 27, B 68, and CB 244).

Table 2.6: Ratio of the N_2H^+ abundance in the core centers to the the maximum abundance, corresponding radius, hydrogen density, and dust temperature

	Ratio [%]	R_{max} [AU]	$n_{\text{H,max}}$ [cm^{-3}]	$T_{\text{D,max}}$ [K]
CB 17	36	7500	4.7×10^4	10.2
CB 27	55	7700	6.5×10^4	11.7
B 68	13	5400	1.4×10^5	9.5
CB 244	41	6400	1.6×10^5	9.5

Table 2.7: Chemical ages of the best fit models for ^{13}CO , C^{18}O , and N_2H^+ .

	Chem. Age of ^{13}CO [yr]	Chem. Age of C^{18}O [yr]	Chem. Age of N_2H^+ [yr]
CB 4	...	10^5	10^5
CB 17	7×10^4	4×10^4	10^5
CB 26	4×10^5	10^4	7×10^4
CB 27	2×10^5	7×10^4	10^5
B 68	2×10^5	7×10^4	10^5
CB 244	2×10^5	4×10^4	4×10^4

Towards the outer edges, CO is photodissociated by UV radiation, so that $X(\text{C}^{18}\text{O})$ there also drops. The emission profiles of ^{13}CO are not as well reproduced by the chemical models as for C^{18}O (see Fig. 2.4). The reason for this is most likely that the emission of this molecule is dominated from the outer envelope which is very likely warmer than the dust in the same layers. Thus, the observed emission profiles are flatter and further extended towards larger radii than it is the case in the models. The optical thickness of the lines becomes apparent for instance in modeled emission profile of CB 244 (Fig. 2.4). The density distribution of this model peaks at a radius of about 2×10^4 AU. The drop towards smaller radii is still indicated in the emission profile, but towards even smaller radii it is dominated by the warm outer layer so that it even rises, thus explaining the double-peaked ^{13}CO emission profiles in CB 27 and CB 244 (Fig. 2.4).

We also plot the profiles of icy C^{18}O as they are predicted by the best-fit chemical models in Fig. 2.6. Its amount in the core center is in some cases larger than the amount of gaseous C^{18}O at its peak position, since at high densities the CO production is faster than the freezeout of atomic C. If the abundances of icy C^{18}O at the core centers are compared to the total C^{18}O abundance in the core centers, the ratios range from 45% in CB 4 to more than 90% in those cores which have a central hydrogen density of more than 10^5 cm^{-3} . In Fig. 2.7, we compare these ratios in all cores and correlate them to the core radius, the hydrogen volume and column densities, and the dust temperature. The freezeout increases towards the core centers and with increasing hydrogen densities. The total temperature range between T_{in} and T_{out} in the cores is less than 10 K and the correlation of freezeout with the temperature is not as clear as for the other quantities. Typically, half of the total C^{18}O molecules stick to the grains at a radius of

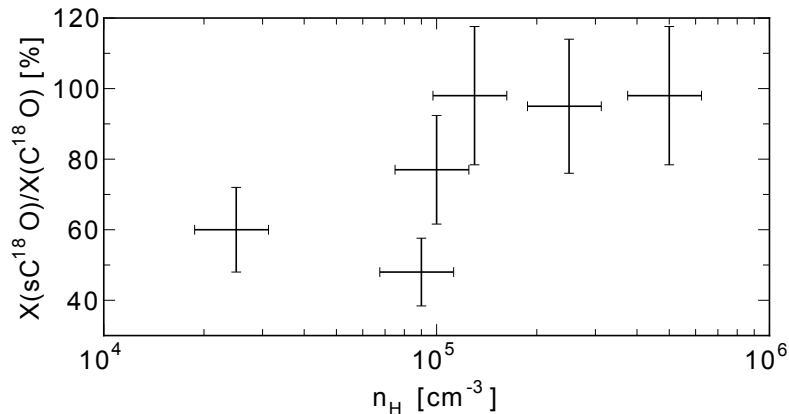


Figure 2.8: Correlation of C^{18}O freeze out and hydrogen density in the core centers. The horizontal error-bars on the hydrogen density represent the fitting uncertainty of the ray-tracing modeling (i.e., excluding systematic uncertainties from, e.g., the dust opacity model; see Sect. 2.3.1). The vertical error bars represent a 20% uncertainty in the amount of icy CO in the chemical model.

$\sim 10^4$ AU, a hydrogen density of $\sim 10^5 \text{ cm}^{-3}$, and a temperature of 11 K. In Table 2.5 we list the maximum level of freezeout in the individual cores and the conditions at which half of the total C^{18}O molecules are frozen onto the dust grains. The correlation of the freezeout level to the hydrogen densities is plotted for the conditions of the core centers in Fig. 2.8.

N_2H^+ ABUNDANCES

N_2H^+ forms and depletes on longer time-scales than CO. We find that in four out of the six studied globules (those with a central density larger than 10^5 cm^{-3}), N_2H^+ is strongly depleted in the core centers. For comparison, we show in Appendix 2.C that a simple line-of-sight averaged LTE-analysis would not reveal depletion of N_2H^+ , although the emission is optically thin ($\tau \lesssim 0.5$) in all cores as we have derived for the calculation of the molecular column densities in Appendix 2.C. The ratios of the central to maximum abundance of N_2H^+ molecules are listed in Table 2.6. They range from 13% to 55%. The radii, hydrogen density and dust temperature at which the N_2H^+ abundances reach their maximum are also given in Table 2.6. CB 4 and CB 26 do not show detectable depletion of N_2H^+ . CB 4 is probably not dense enough and CB 26 might be too young to show depletion at its low central density (see Sect. 2.4.4). The correlation of $X(\text{N}_2\text{H}^+)$ with core radii, hydrogen volume and column density and with temperature are plotted for all cores in the bottom row of Fig. 2.7. $X(\text{N}_2\text{H}^+)$ typically peaks at hydrogen densities of 10^5 cm^{-3} in cores at a chemical age of 10^5 yr. The mean radius of the peak $X(\text{N}_2\text{H}^+)$ is (6800 ± 1000) AU. We resolve the regions of N_2H^+ depletion in all cores, since these radii are 2 to 3 times larger than the half beamwidth.

We find that the depletion of N_2H^+ is stronger restricted to the center as compared to CO and occurs at hydrogen densities $\gtrsim 10^5 \text{ cm}^{-3}$ and column densities $> 10^{22} \text{ cm}^{-2}$, and requires a chemical age of $\gtrsim 10^5$ yr. This finding is consistent with the work of Bergin et al. (2002) on

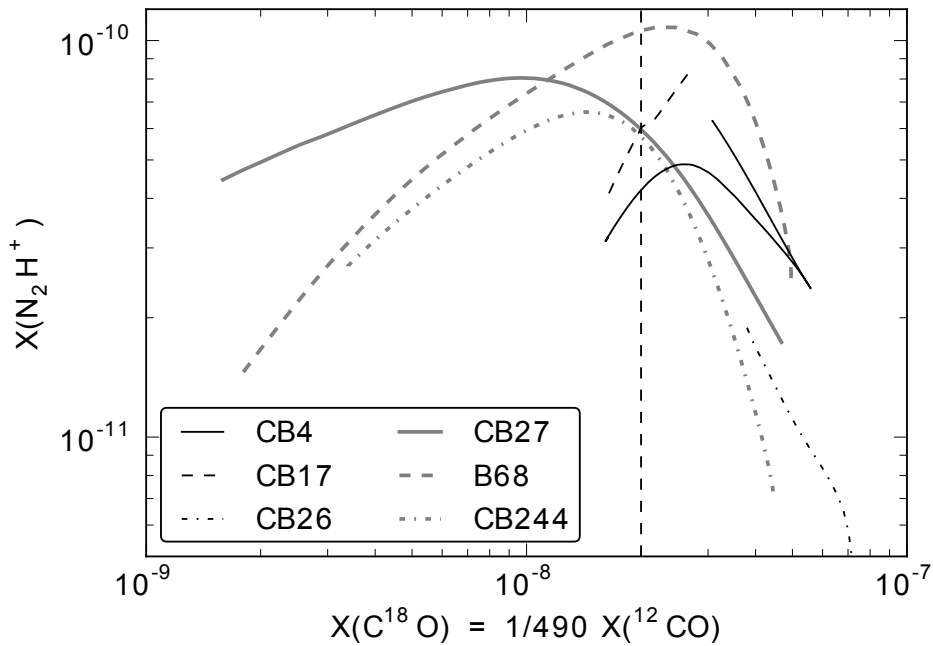


Figure 2.9: Relative gas phase abundance of C^{18}O against that of N_2H^+ . At $X(\text{C}^{18}\text{O}) \approx 2 \times 10^{-8}$ the correlations turns over into an anti-correlation. While at high $X(\text{C}^{18}\text{O})$ the N_2H^+ molecules are destroyed by reactions with CO, at low $X(\text{C}^{18}\text{O})$ (and high densities) freeze-out of nitrogen is the dominant reason for depletion of N_2H^+ .

B 68, while other studies have claimed that depletion of N-bearing species would only occur at hydrogen densities $\gtrsim 10^6 \text{ cm}^{-3}$ (Tafalla et al. 2002; Pagani et al. 2005). The abundance quickly increases outwards and peaks where the majority of CO is still frozen onto the grains. Further outwards, it drops where CO becomes abundant in the gas phase. In Fig. 2.9, we plot the relative gas phase C^{18}O abundance against that of N_2H^+ for all globules. The N_2H^+ and C^{18}O abundances are anti-correlated at C^{18}O abundances above 10^{-8} (corresponding to $X(\text{CO}) = 5 \times 10^{-6}$ when assuming $X(\text{CO})/X(\text{C}^{18}\text{O}) = 490$), but the curves turn over to a positive gradient below this value. At this point, depletion of nitrogen mainly in form of N and N_2 becomes the dominant reason for depletion of N_2H^+ compared to reactions with CO.

CHEMICAL AGE OF THE CORES

”Chemical age” is a parameter in the modeling process. It sets the time span during which the gas develops starting from a state of purely atomic gas of 13 different elements. In this period complex molecules build up and deplete onto the grains. We find that the individual species are fitted best for models of different chemical ages. They are listed in Table 2.7. The average chemical age of the ^{13}CO best-fit models is $(2 \pm 1) \times 10^5$ yr, for C^{18}O $(6 \pm 3) \times 10^4$ yr, and for N_2H^+ $(9 \pm 2) \times 10^4$ yr. Up to an age of $\sim 2 \times 10^5$ yr, the chemical models evolve quickly so that deviations of a few 10^4 yr already lead to significantly worse fits of the models to the data.

Therefore, the difference in the chemical ages of the best-fit models between the individual species is significant. ^{13}CO which traces mainly the outer envelope of the cores is modeled best with chemical ages that are on average more than 10^5 yr higher than those of the best-fit models of C^{18}O and N_2H^+ .

We interpret this finding as a result of core contraction and cooling during the chemical evolution. This would accelerate the freezeout of CO and the synthesis of N_2H^+ molecules. Since we assume a constant physical structure in the chemical modeling, we would thus systematically underestimate the chemical age of those species that trace the regions which have been contracting during the chemical evolution. Additional support for this hypothesis is provided by the analysis of the gravitational stability of the cores in Sect. 2.4.2. We found there that four cores are thermally supercritical and might be gravitationally unstable. This finding is less profound for the other two cores, but cannot be excluded.

Other effects that are not included in our model, such as non-thermal desorption processes like explosive desorption (Shalabiea & Greenberg 1994) or exothermic reactions in the grain mantles (Garrod et al. 2007), might also lead to an underestimation of the chemical ages. Also turbulent diffusion (Xie et al. 1995; Willacy et al. 2002) of the gas and grains within the cores can decelerate the chemical aging. Coagulation of the dust grains in the dense part would also slow down the chemical evolution, since thereby the grain surface area and thus the rate of grain surface reactions are reduced. In Sect. 2.4.4 we show, however, that the bulk of the dust in these globules cannot be significantly processed and coagulated. Accounting for these combined intrinsic uncertainties in the density structures of the cores, uncertainties associated with chemical reaction rates, and a range of grain sizes in the depletion zone of the cloud, we estimate that the best-fit chemical ages are between 10^5 and 10^6 years. This is consistent with a pre-stellar core life-time of 0.3-1.6 Myr as derived by Lee & Myers (1999).

STRENGTH OF THE IMPACTING UV-FIELD

Changing the parameter $A_{v,\text{out}}$ that accounts for the unconstrained extent of the dusty material around the globules in the chemical models has effects that cannot always be clearly distinguished from changing either the hydrogen density or the gas temperature. Nevertheless, the observations are modeled better, if $A_{v,\text{out}}$ is increased half of the globules by a few mag relative to the values that have been measured with NIR extinction mapping (which range from 0.2 to 2 mag for the different globules at the model boundaries). This is probably not a result of an overestimation of the ISRF in the chemical models. Launhardt et al. (2013) derived the total FIR/mm luminosity of the globules and it is for all of them approximately equal to the luminosity of the "Standard UV-field" (Draine 1978) impacting on spheres of the size of the globules. The same field is also adopted in the chemical modeling and we thus do not overestimate its strength.

In the envelopes of the globules at hydrogen densities below 10^4 cm^{-3} , gas and dust temper-

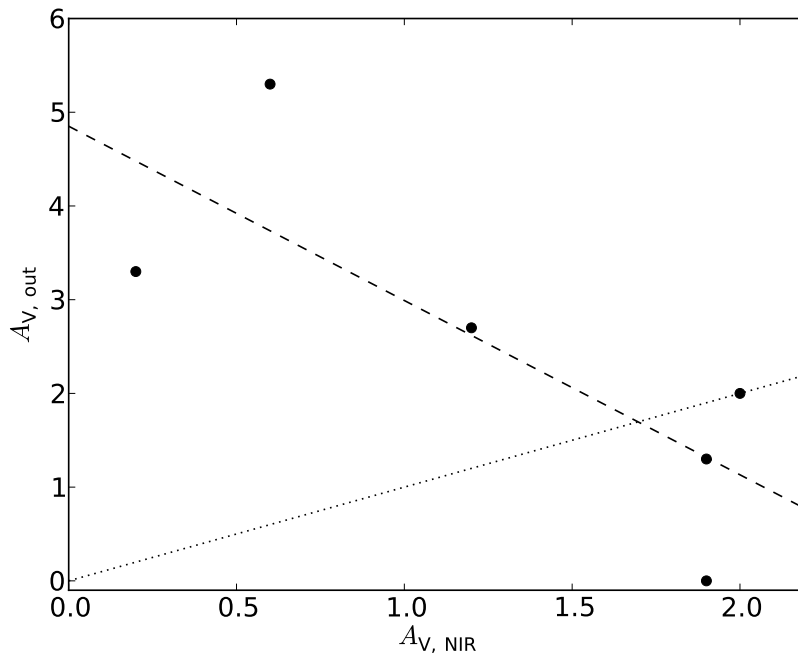


Figure 2.10: We plot the parameters $A_{V,\text{out}}$ of the best models over the measured values of $A_{V,\text{NIR}}$ from the NIR extinction maps. The dashed line is a linear fit to the data points which is only meant to illustrate the trend. The dotted line indicates $A_{V,\text{out}} = A_{V,\text{NIR}}$. We interpret the anti-correlation as indication of an increasing decoupling of gas and dust temperatures towards lower extinction.

atures are expected to be decoupled. Since we assume equal gas and dust temperatures in the modeling, we introduce systematic errors in our analysis. In particular, the emission of the gas in the envelopes is underestimated. With a large $A_{V,\text{out}}$ we artificially compensate this error. The additional shielding protects the molecules from being photodissociated and thus increases their abundance. This hypothesis is supported when comparing $A_{V,\text{out}}$ of the best models to $A_{V,\text{NIR}}$ which are the values derived from the NIR extinction maps. Both values appear to be anti-correlated and while we do not need to increase $A_{V,\text{out}}$ with respect to the observed values at $A_{V,\text{NIR}} \sim 2$ mag, we have to increase it by more than 3 mag for the least shielded cores. Because of these uncertainties, we think that the need to increase $A_{V,\text{out}}$ is not a convincing evidence that the globules are in fact stronger shielded from UV-radiation than inferred from NIR-extinction maps.

A direct measurement of the gas temperature in the envelopes would of course be desirable as constraint for the chemical modeling and, furthermore, in comparison to the dust temperature it would allow to distinguish between shielding from extended envelopes and a weaker ISRF as the presumed Draine field, since the gas is only heated from the FUV component of the ISRF. Measuring the excitation of the gas in the envelopes is difficult, however, since the emission is weak and most transitions are subthermally excited. The best-suited transition to study for this purpose might therefore be the ^{12}CO ($J=1-0$) line. Unfortunately, we do not have such data at hand. Another way to distinguish between both scenarios may be to study

the distribution and emission of PAHs. All globules of this study have been mapped with *Spitzer's* infrared array camera (IRAC). In particular the $5.8\ \mu\text{m}$ and $8\ \mu\text{m}$ bands are known to show PAH emission (e.g., Pagani et al. 2010). However, the maps are not extended enough to define a background level that would allow to derive absolute values of the emission.

CONSTRAINTS ON THE GRAIN PROPERTIES

To correctly model the observed molecular abundances, we must increase the molecular hydrogen density and with it the initial abundances of all species by a factor of 2 to 3 (except for B 68). We thus seem to systematically underestimate the hydrogen density in the dust-based modeling. This is understandable at least in the envelopes of the cores since we have assumed mildly coagulated grains, with a coagulation time of 10^5 yr at a gas density of $10^5\ \text{cm}^{-3}$ (Ossenkopf & Henning 1994)⁸ over the entire globule. With the assumption of normal ISM dust (e.g., OH1), we would have derived hydrogen densities which are by a factor of 2.5 higher. Increasing the density could also partly compensate an underestimation of the gas temperature. However, we do not find a dependence on the observed A_V . Moreover, the only core for which we do not have to increase the density is that of B 68 – one of the least shielded cores in our sample. Our molecular line observations and modeling thus suggest that in most regions of the cores that are resolved by our study, the grains are not yet significantly coagulated.

2.5 CONCLUSIONS

We have observed a sample of seven globules containing starless cores in the ^{12}CO (J=2-1), the ^{13}CO (J=2-1), the C^{18}O (J=2-1) and the N_2H^+ (J=1-0) transitions. The globules were also observed with the Herschel bolometers as part of the EPoS project (Launhardt et al. 2013). We present dust temperature and hydrogen density maps of the globules that have been obtained with a ray-tracing technique. Based on these dust-based temperature and density profiles, we analyze the molecular emission assuming $T_{\text{Dust}} = T_{\text{Gas}}$. In the following we summarize the main results of this study.

1. We confirm the findings of Launhardt et al. (2013) on the stability of the cores. Only one starless core (CB 244, see also Stutz et al. 2010) is clearly not supported against gravitational collapse by thermal pressure. CB 17, CB 27, and B 68 are probably also thermally supercritical. CB 4 and CB 26 are probably gravitationally stable.
2. CO is depleted in the center of all studied cores to a level of at least 46%. CB 27, B 68, and CB 244 show a central CO depletion of more than 90%. The level of freezeout

⁸[ftp://cdsarc.u-strasbg.fr/pub/cats/J/A+A/291/943](http://cdsarc.u-strasbg.fr/pub/cats/J/A+A/291/943)

- increases towards the core centers and with the hydrogen density. The average radius at which half of the CO is frozen to the grains is 9000 AU, the average hydrogen density is 10^5 cm^{-3} .
3. N_2H^+ is depleted in the center of the cores with hydrogen densities exceeding 10^5 cm^{-3} . The radius with maximum abundance of N_2H^+ is on average at 6800 AU. The degree of depletion in the center with respect to the maximum abundance ranges from 13% to 55%.
 4. The chemical age at which we find the models to match the data best is higher for ^{13}CO than for C^{18}O and N_2H^+ . We find an average age of the six modeled cores of $2 \pm 1 \times 10^5$ yr for ^{13}CO and of $6 \pm 3 \times 10^4$ yr for C^{18}O , and $9 \pm 2 \times 10^4$ yr for N_2H^+ . The different ages of the dense gas tracers and ^{13}CO suggest a central contraction of the cores during the chemical evolution. Considering the uncertainties, all cores have a chemical age of at most 10^6 yr and are probably younger.
 5. We generally need to increase the gas density which has been derived from the dust density assuming mildly coagulated grains⁸ by a factor of 2-3 in order to model the observed molecular emission profiles correctly. We interpret this as sign that the dust grains are not as heavily coagulated as assumed by our dust model in large parts of the globules and are better described by ISM dust models like OH1.
 6. We have to reduce the strength of the UV radiation field impacting at the globule boundaries with respect to the value predicted by [Draine \(1978\)](#) for half of the cores. However, we think that this does not indicate that the impacting UV-field is in fact weaker, but rather that we thereby compensate for the systematic error which is introduced by the underestimation of the gas temperature in the envelopes of these cores.

2.A OBSERVATIONS

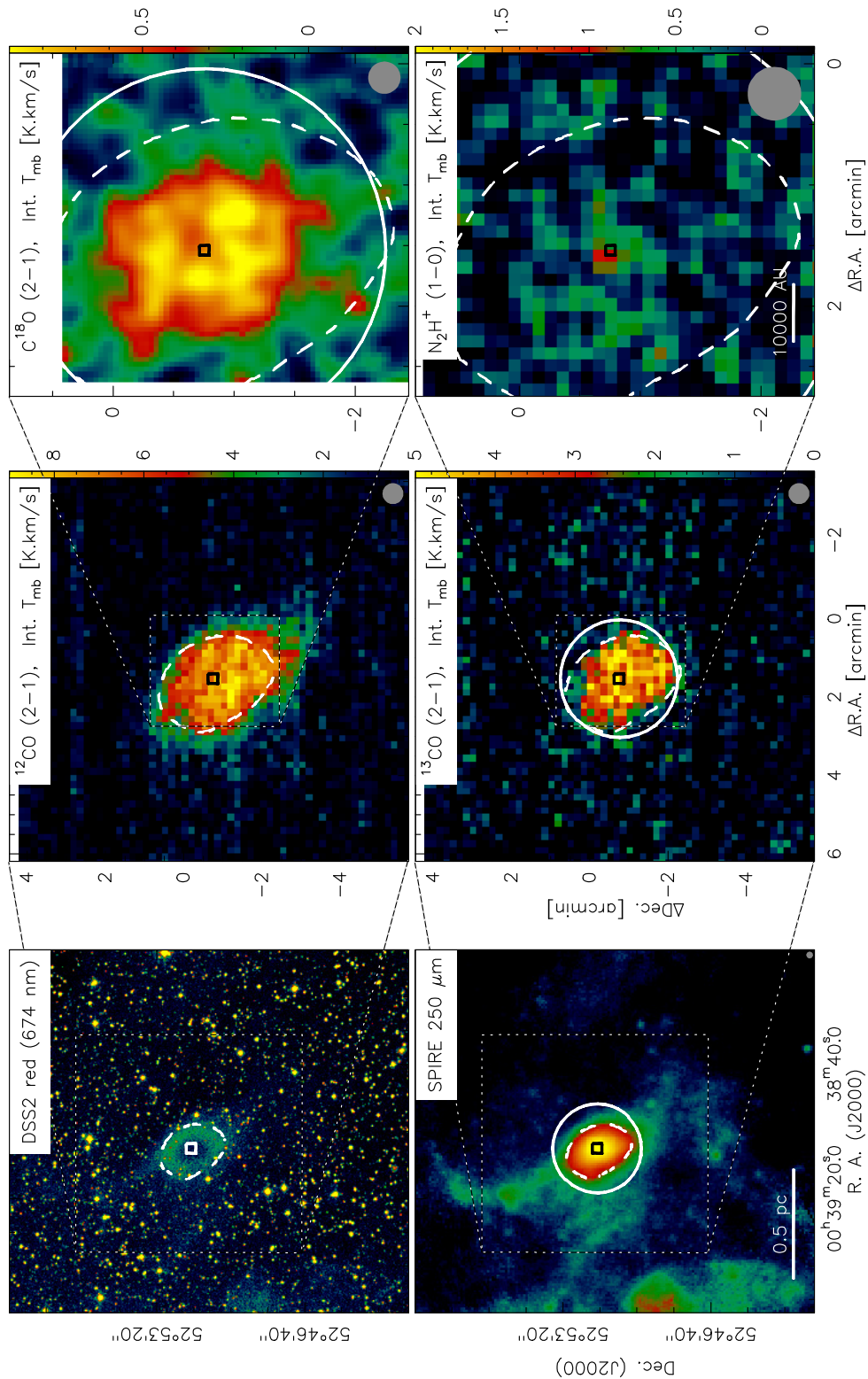


Figure 2.11: Observations of CB4. Digitized Sky Survey (DSS) red, Herschel SPIRE 250 μm , ^{12}CO ($J=2-1$), ^{13}CO ($J=2-1$), C^{18}O ($J=2-1$), and N_2H^+ ($J=1-0$). The grey circles in the lower right corners indicate the respective beam sizes. The squared marker indicates the center of the starless core. The dashed contour marks $N_{\text{H}} = 10^{21} \text{cm}^{-2}$. The white circles indicate the regions of which 1D-profiles were obtained by azimuthally averaging.

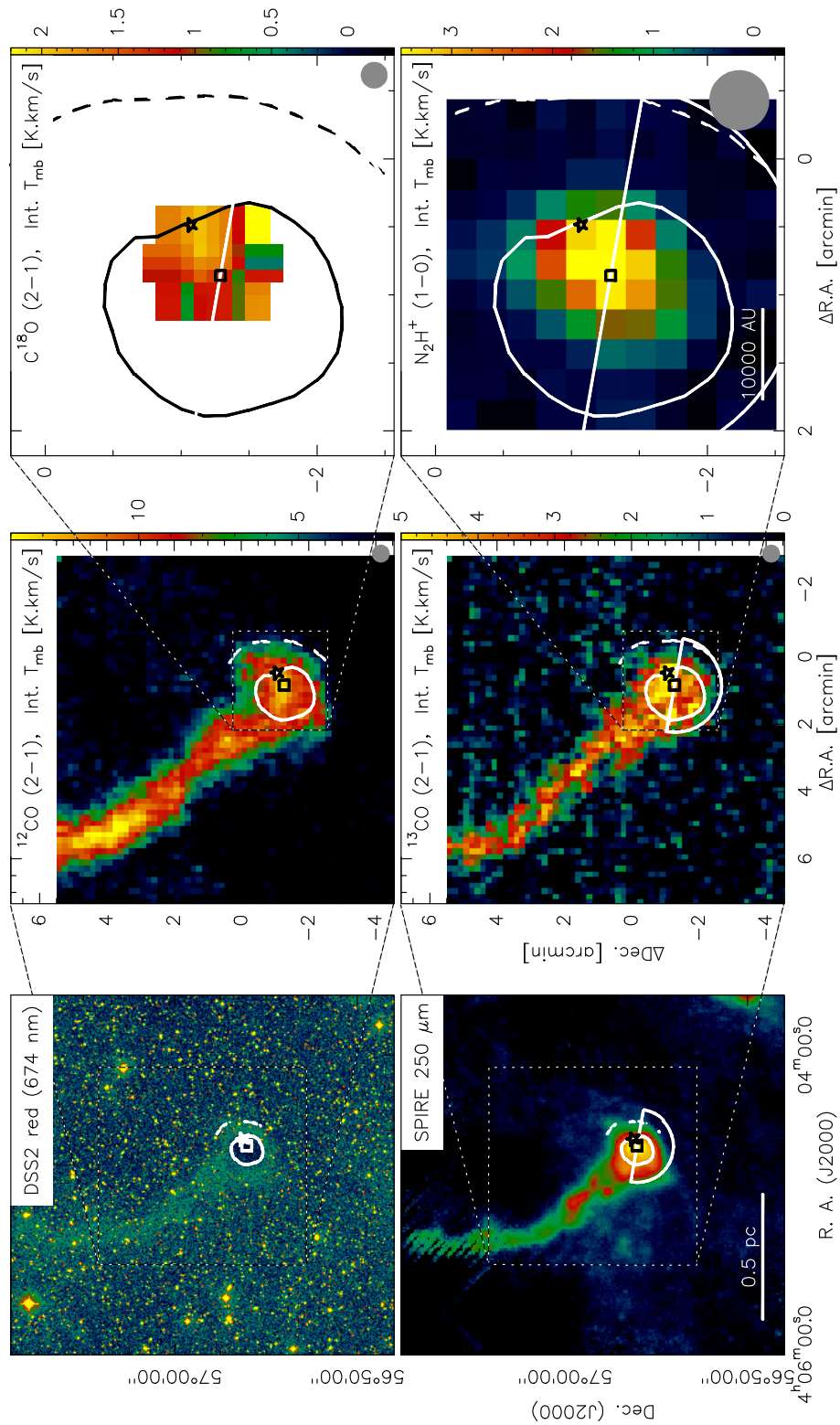


Figure 2.12: Observations of CB17. DSS red, Herschel SPIRE 250 μm , ^{12}CO ($J=2-1$), ^{13}CO ($J=2-1$), C^{18}O ($J=2-1$), and N_2H^+ ($J=1-0$). The grey circles in the lower right corners indicate the respective beam sizes. The squared marker indicates the center of the starless core. The asterisk the position of the Class I YSO. The dashed contour marks $N_{\text{H}} = 10^{21}\text{cm}^{-2}$, the solid contour $N_{\text{H}} = 10^{22}\text{cm}^{-2}$. The white circles indicate the regions of which 1D-profiles were obtained by azimuthally averaging.

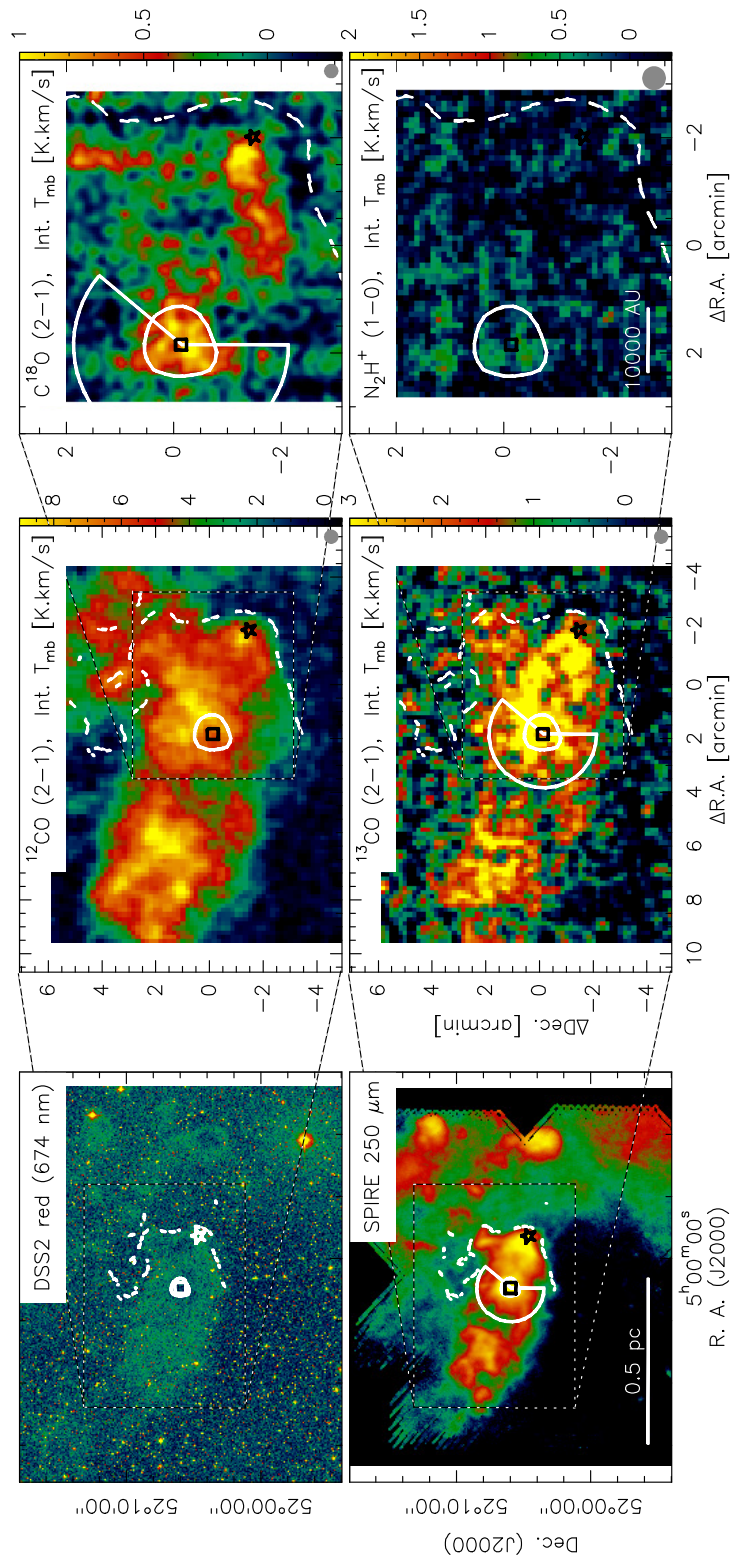


Figure 2.13: Observations of CB26. DSS red, Herschel SPIRE 250 μm , ^{12}CO (J=2-1), ^{13}CO (J=2-1), C^{18}O (J=2-1), and N_2H^+ (J=1-0). The grey circles in the lower right corners indicate the respective beam sizes. The squared marker indicates the center of the starless core. The asterisk the position of the Class I YSO. The dashed contour marks $N_{\text{H}} = 10^{21} \text{cm}^{-2}$, the solid contour $N_{\text{H}} = 10^{22} \text{cm}^{-2}$. The white circles indicate the regions of which 1D-profiles were obtained by azimuthally averaging.

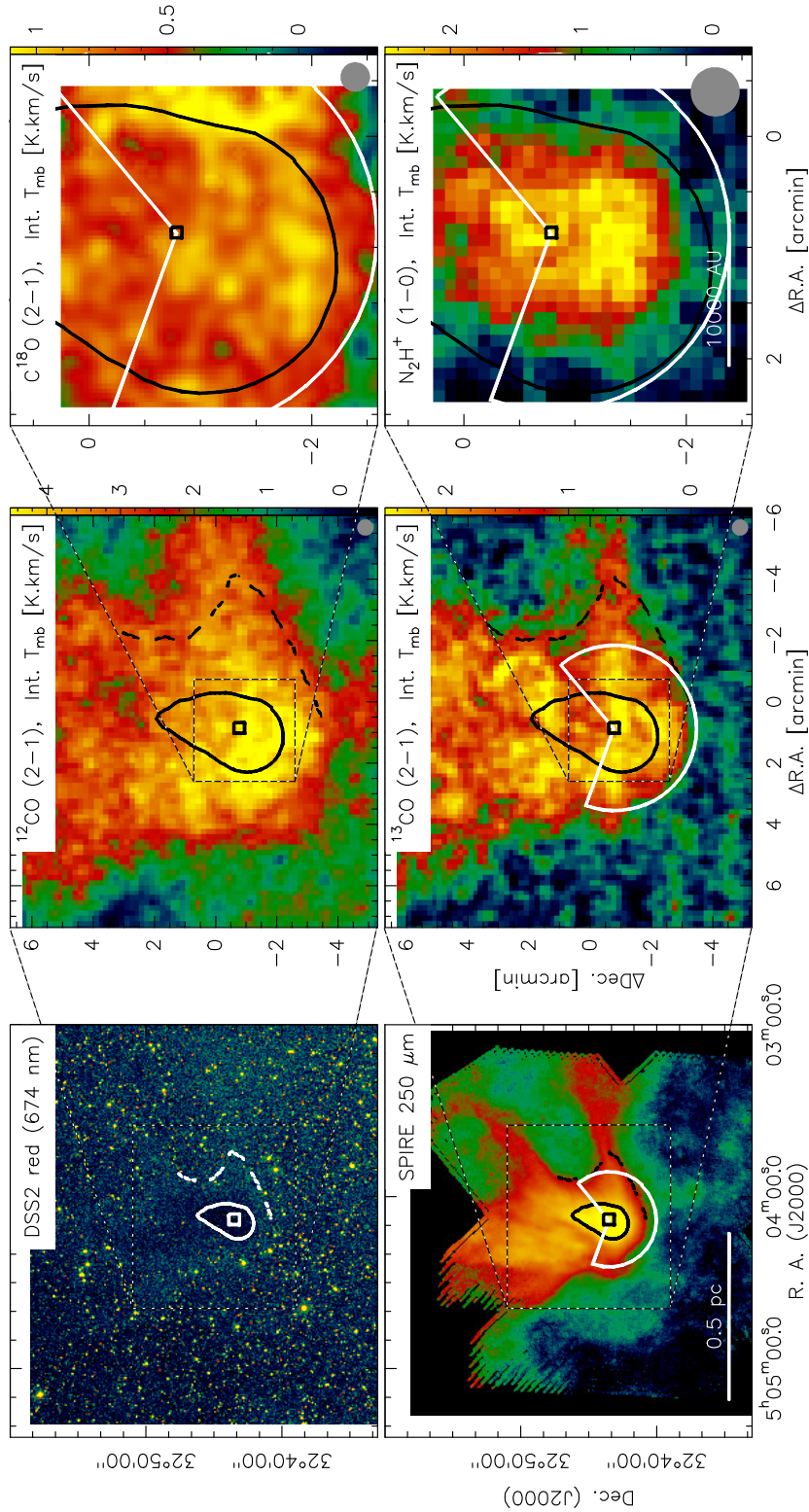


Figure 2.14: Observations of CB27. DSS red, Herschel SPIRE 250 μm , ^{12}CO ($J=2-1$), ^{13}CO ($J=2-1$), C^{18}O ($J=2-1$), and N_2H^+ ($J=1-0$). The grey circles in the lower right corners indicate the respective beam sizes. The squared marker indicates the center of the starless core. The dashed contour marks $N_{\text{H}} = 10^{21}\text{cm}^{-2}$, the solid contour $N_{\text{H}} = 10^{22}\text{cm}^{-2}$. The white circles indicate the regions of which 1D-profiles were obtained by azimuthally averaging.

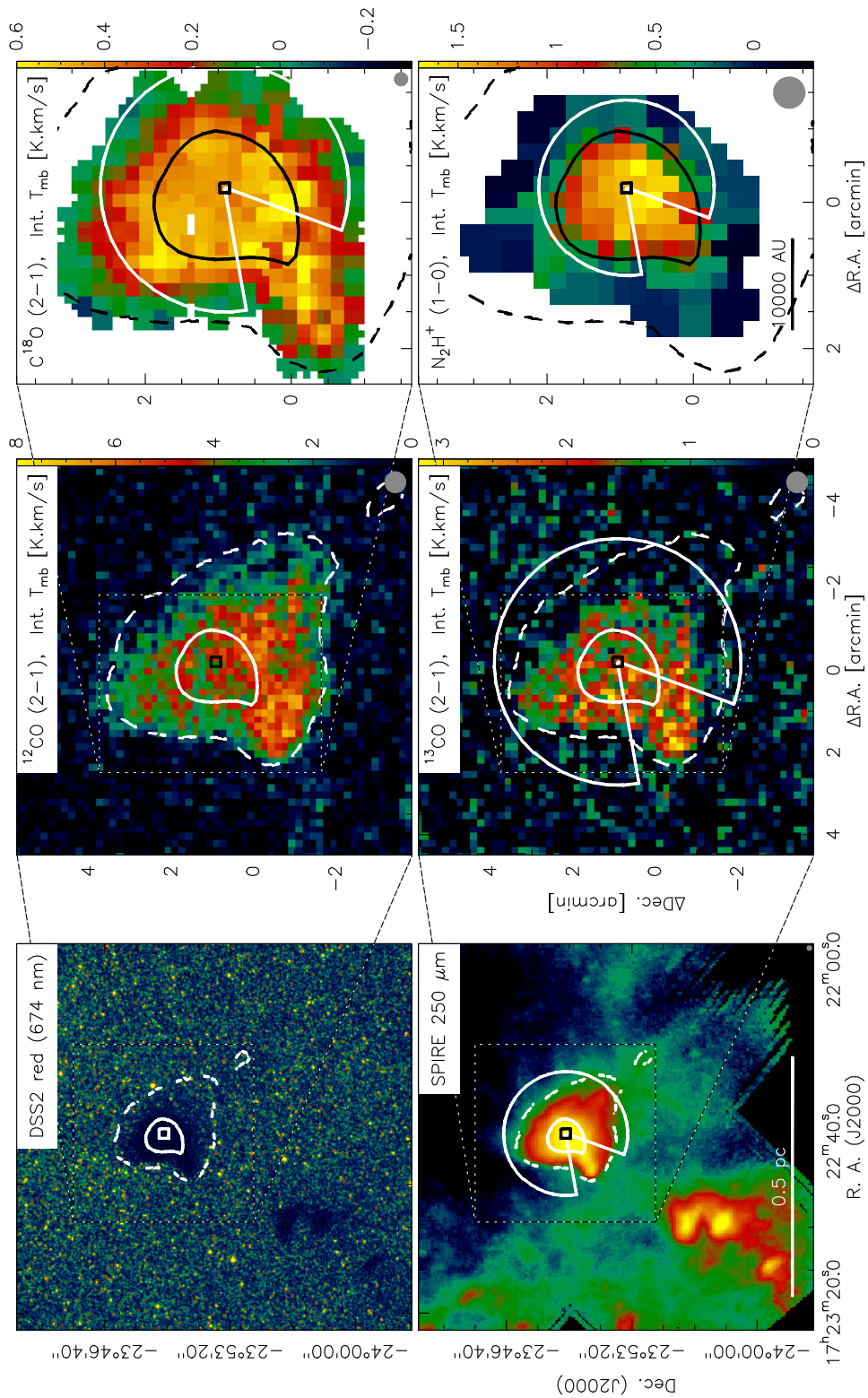


Figure 2.15: Observations of B68. DSS red, Herschel SPIRE 250 μm , ^{12}CO (J=2-1), ^{13}CO (J=2-1), C^{18}O (J=2-1), and N_2H^+ (J=1-0). The grey circles in the lower right corners indicate the respective beam sizes. The squared marker indicates the center of the starless core. The dashed contour marks $N_{\text{H}} = 10^{21}\text{cm}^{-2}$, the solid contour $N_{\text{H}} = 10^{22}\text{cm}^{-2}$. The white circles indicate the regions of which 1D-profiles were obtained by azimuthally averaging.

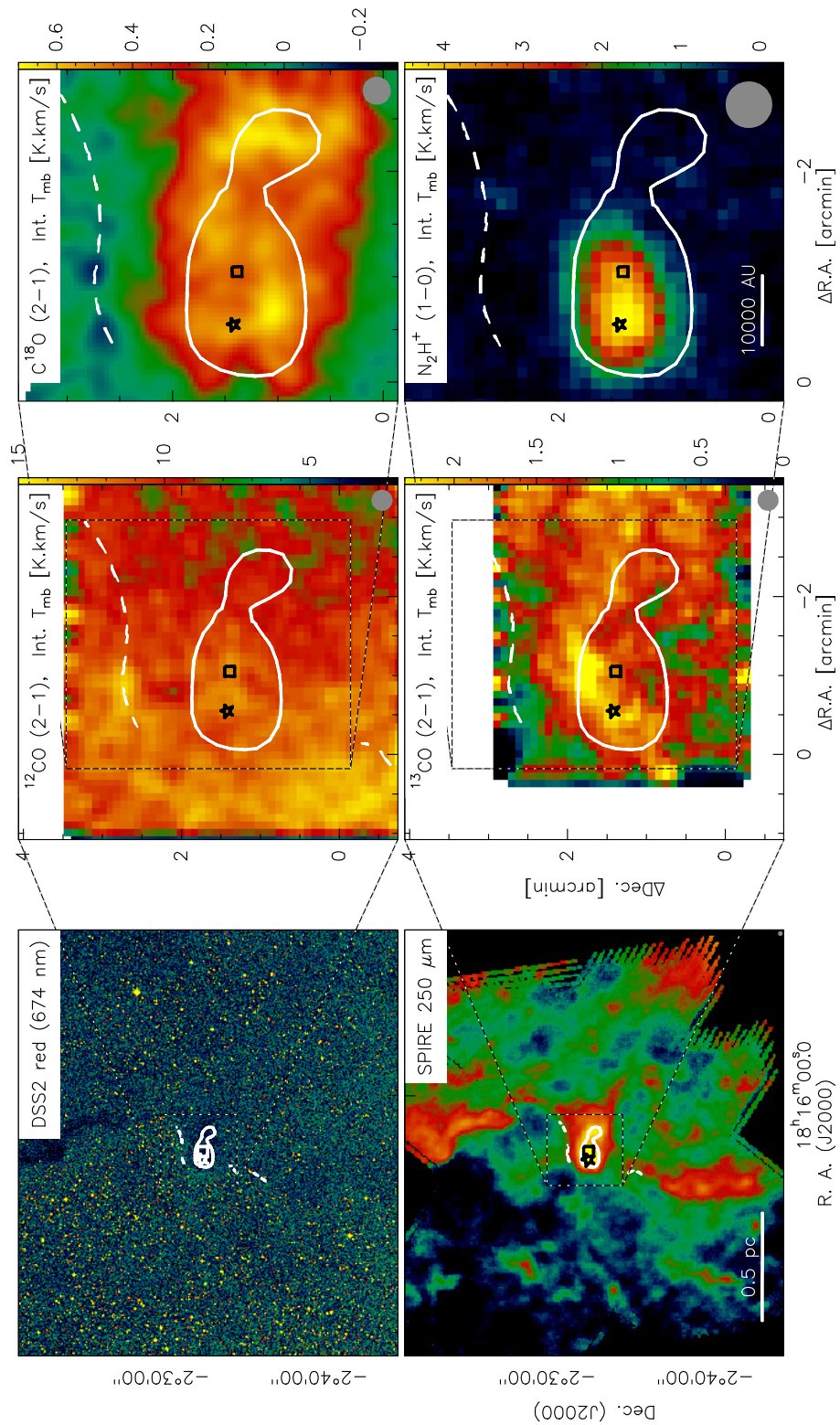


Figure 2.16: Observations of CB130. DSS red, Herschel SPIRE 250 μm , ^{12}CO ($J=2-1$), ^{13}CO ($J=2-1$), C^{18}O ($J=2-1$), and N_2H^+ ($J=1-0$). The grey circles in the lower right corners indicate the respective beam sizes. The squared marker indicates the center of the starless core. The asterisk the position of the Class I YSO. The dashed contour marks $N_{\text{H}} = 10^{21} \text{cm}^{-2}$, the solid contour $N_{\text{H}} = 10^{22} \text{cm}^{-2}$. The white circles indicate the regions of which 1D-profiles were obtained by azimuthally averaging.

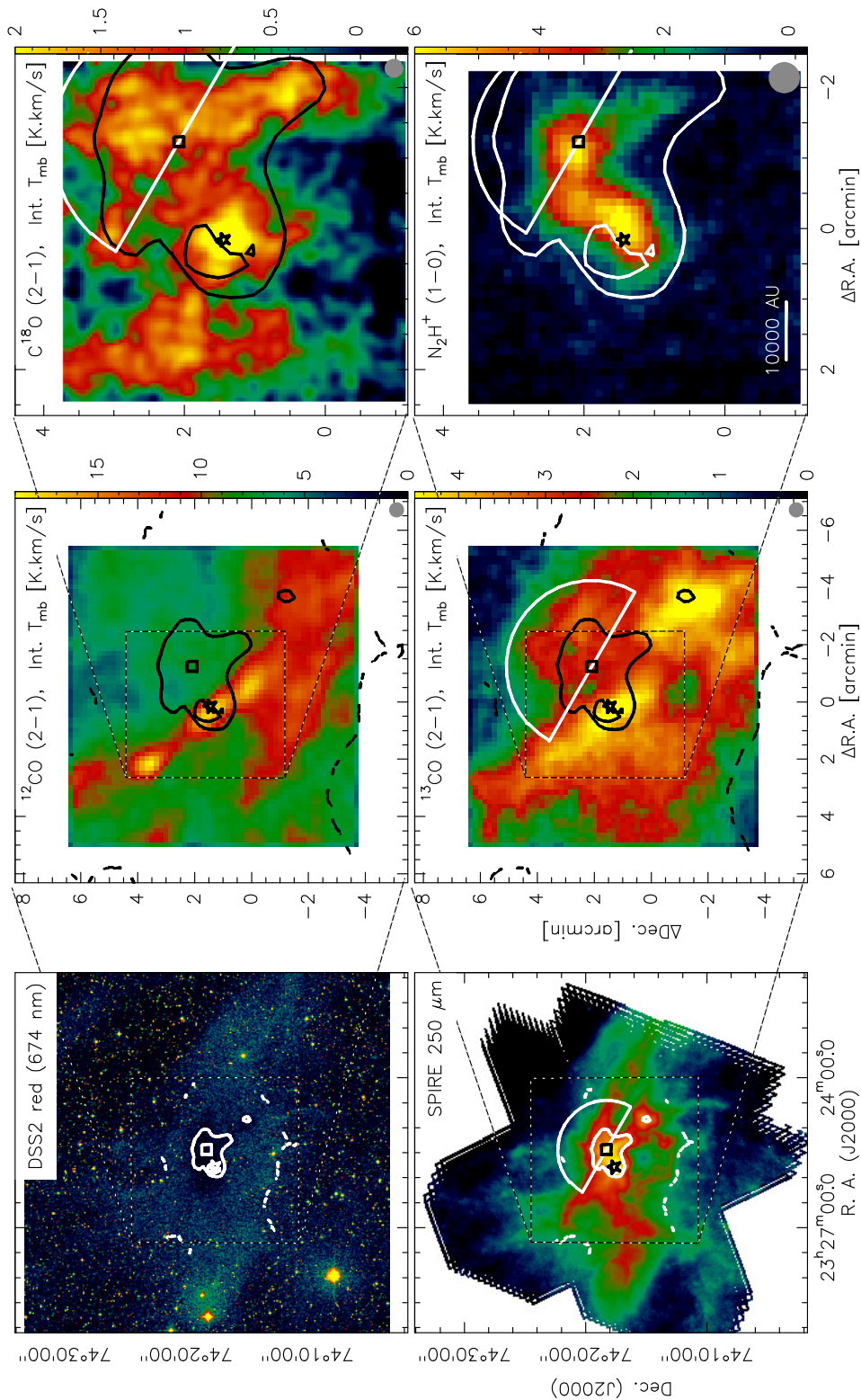


Figure 2.17: Observations of CB244. DSS red, Herschel SPIRE 250 μm , ^{12}CO ($J=2-1$), ^{13}CO ($J=2-1$), C^{18}O ($J=2-1$), and N_2H^+ ($J=1-0$). The grey circles in the lower right corners indicate the respective beam sizes. The squared marker indicates the center of the starless core. The asterisk the center of the Class 0 protostellar core. The dashed contour marks $N_{\text{H}} = 10^{21}\text{cm}^{-2}$, the solid contour $N_{\text{H}} = 10^{22}\text{cm}^{-2}$. The white circles indicate the regions of which 1D-profiles were obtained by azimuthally averaging.

2.B HYDROGEN DENSITY AND DUST TEMPERATURE MAPS

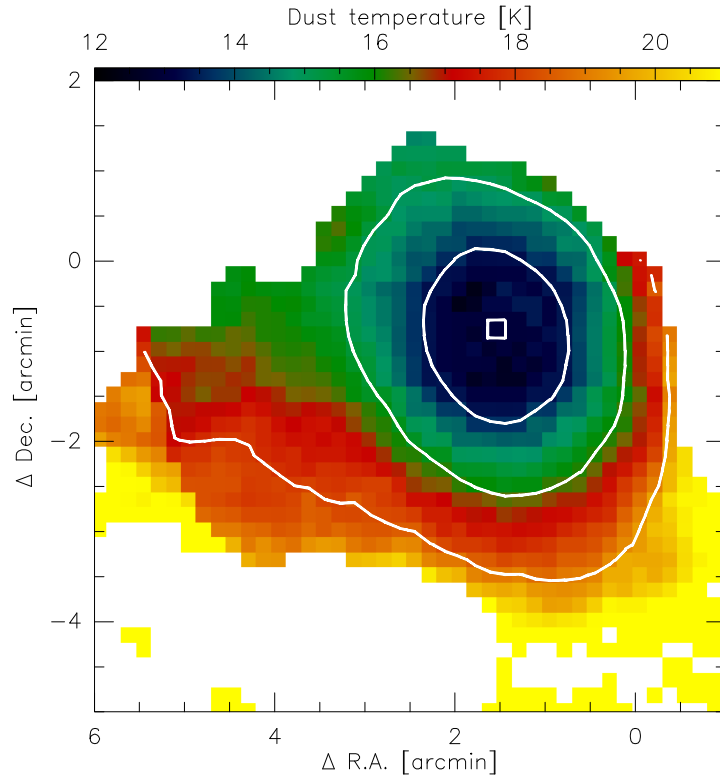


Figure 2.18: Dust temperature map of CB4. Overlaid with contours of the hydrogen density. They mark densities of 10^2 , 10^3 , and 10^4 cm^{-3} . The square indicates the center of the starless core.

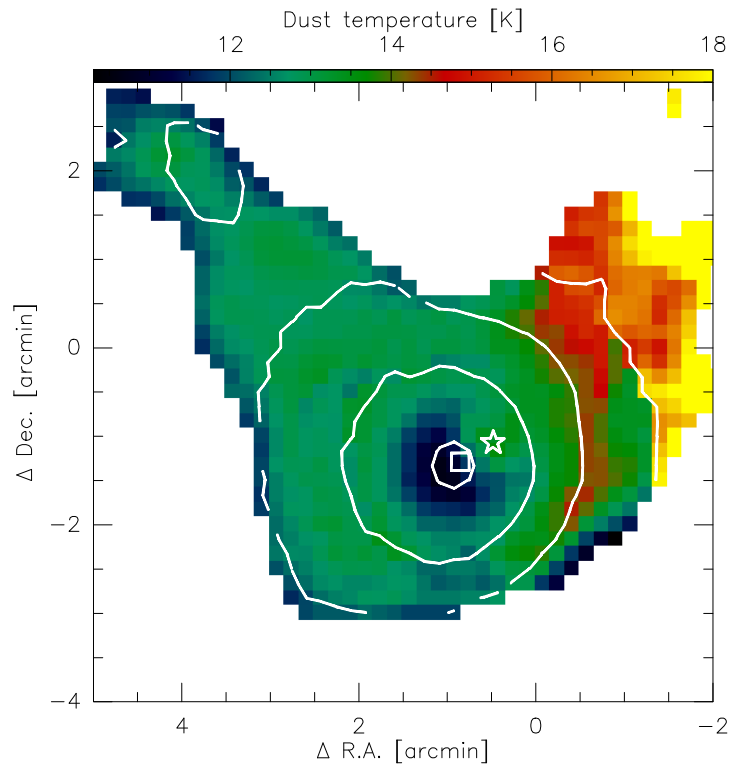


Figure 2.19: Dust temperature map of CB17. Overlaid with contours of the hydrogen density. They mark densities of 10^2 , 10^3 , 10^4 , and 10^5 cm⁻³. The square indicates the center of the starless core.

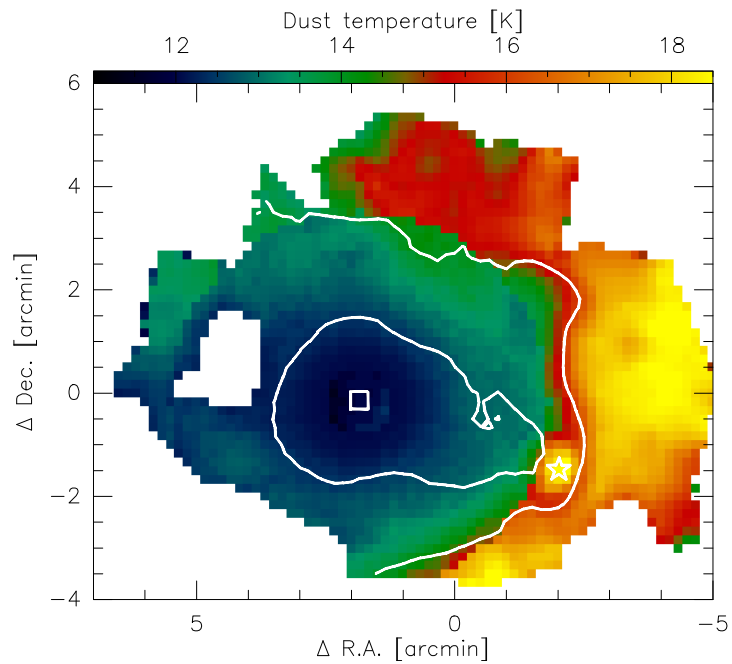


Figure 2.20: Dust temperature map of CB26. Overlaid with contours of the hydrogen density. They mark densities of 10^3 , and 10^4 cm⁻³. The square indicates the center of the starless core.

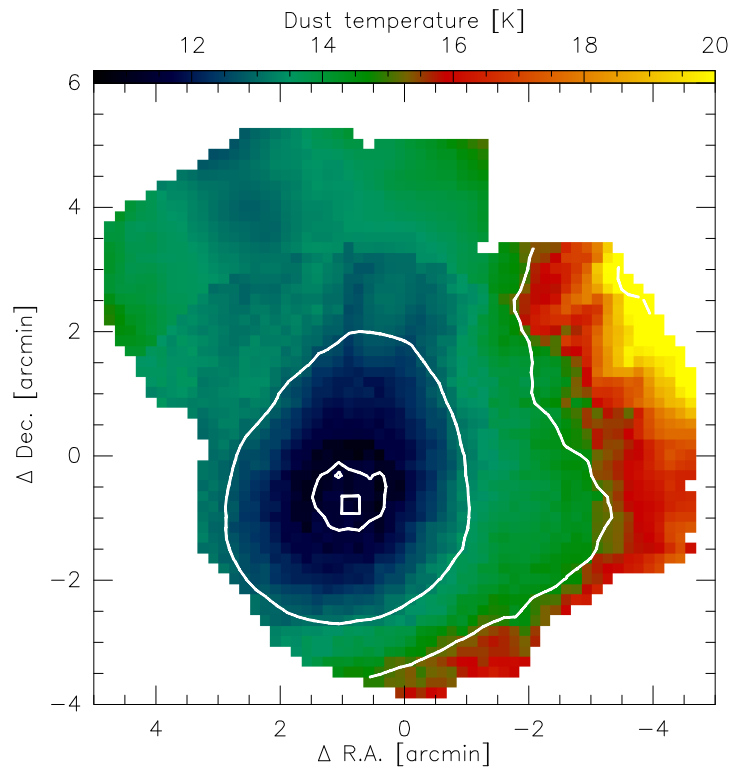


Figure 2.21: Dust temperature map of CB27. Overlaid with contours of the hydrogen density. They mark densities of 10^3 , 10^4 , and 10^5 cm^{-3} . The square indicates the center of the starless core.

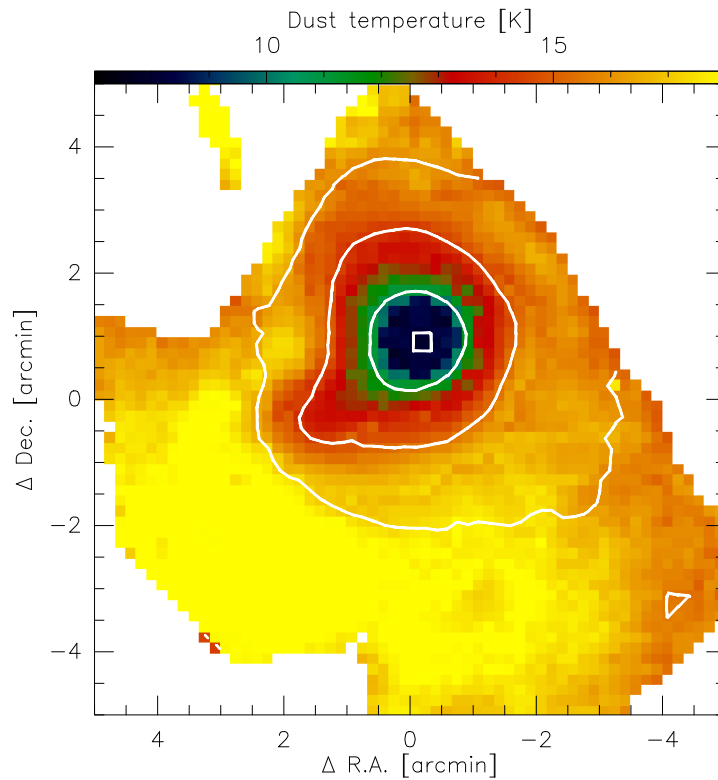


Figure 2.22: Dust temperature map of B68. Overlaid with contours of the hydrogen density. They mark densities of 10^3 , 10^4 , and 10^5 cm^{-3} . The square indicates the center of the starless core.

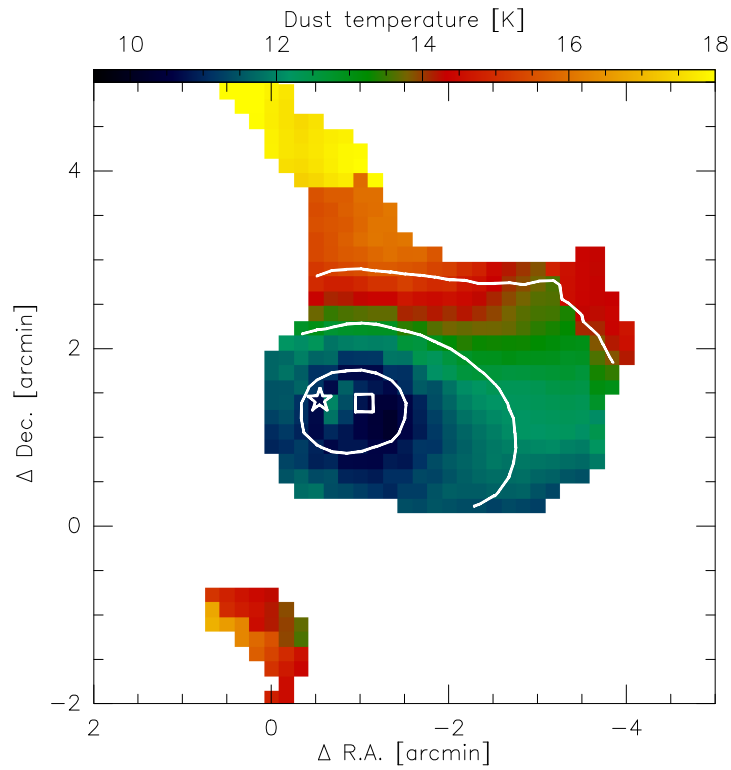


Figure 2.23: Dust temperature map of CB130. Overlaid with contours of the hydrogen density. They mark densities of 10^3 , 10^4 , and 10^5 cm^{-3} . The square indicates the center of the starless core.

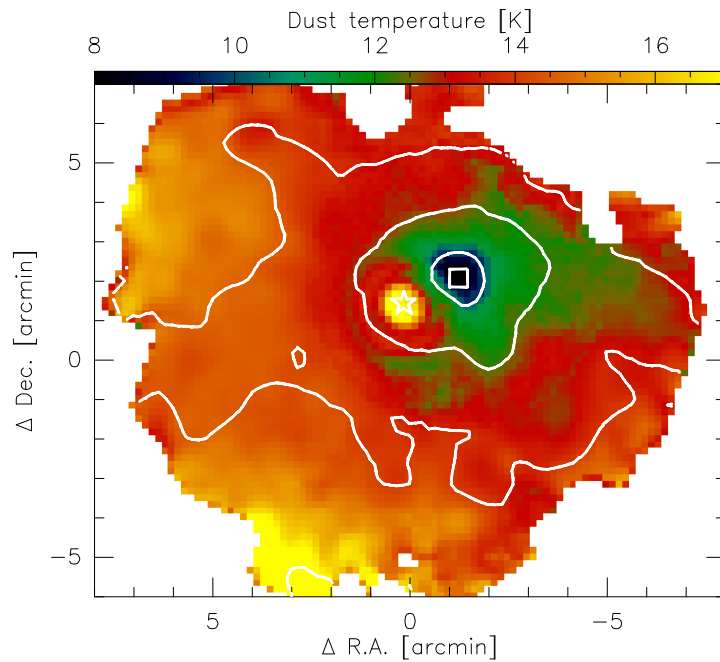


Figure 2.24: Dust temperature map of CB244. Overlaid with contours of the hydrogen density. They mark densities of 10^3 , 10^4 , and 10^5 cm^{-3} . The square indicates the center of the starless core.

2.C LTE ANALYSIS

2.C.1 MODEL

We estimated the molecular column densities of ¹³CO, C¹⁸O and N₂H⁺ in a first step with a simple and well-established approach. For completeness, we shortly describe here this simplified approach, the results and discuss the differences and drawbacks with respect to the full chemical modeling.

We do not model the emission of the ¹²CO (J=2-1) transition, since it becomes optically thick already at $n_{\text{H}} < 10^4$ and therefore does not trace the regions of expected freezeout. At these low densities gas and dust temperatures might also be decoupled (Galli et al. 2002) which is an additional obstacle for the interpretation of the ¹²CO emission.

The method is described in Stahler & Palla (2005). It assumes local thermal equilibrium (LTE) and a constant gas temperature along the line-of-sight. Since we do not have an independent measurement of the gas temperature, we make the simplifying assumption that the kinetic gas temperature is the same as the dust temperature we have obtained from the LoS-averaged black body-fitting of the continuum data in Launhardt et al. (2013). This is justified in the dense interiors of the starless cores, but may no longer be strictly valid in the outer parts at hydrogen densities below a few 10^4 cm^{-3} .

In preparation of the analysis, we obtain maps of the flux in the observed lines by integrating over the velocity axis of the spectral cubes. Maps of the linewidths of the CO isotopologues were derived from Gaussian fits to the spectra. For N₂H⁺ we use the hfs-fitting routine provided with the CLASS package of GILDAS⁹. This routine allows to fit the full hyperfine structure of the $J = 1 - 0$ transition and thereby also derives the optical depth of the lines. The frequency offsets and relative strengths of the individual lines are adopted from Caselli et al. (1995). With these intermediate results at hand we can derive the molecular column densities using

$$N = \frac{8\pi\nu_0^2\Delta\nu Q\Delta\tau}{c^2A_{\text{ul}}}\left(\frac{g_{\text{l}}}{g_{\text{u}}}\right)\left[1 - \exp\left(-\frac{T_0}{T_{\text{ex}}}\right)\right]^{-1}, \quad (2.8)$$

where ν_0 is the frequency of the transition, $\Delta\nu$ the observed linewidth, Q the partition function of the rotational levels, $\Delta\tau$ the total optical thickness of the line, A_{ul} the Einstein parameter of the transition, g_{i} the relative statistical weights of the upper and lower levels, $T_0 = h\nu_0/k_{\text{B}}$, and T_{ex} the excitation temperature of the molecules. Since we assume LTE we set $T_{\text{ex}} = T_{\text{gas}} =$

⁹<http://www.iram.fr/IRAMFR/GILDAS>

$T_{\text{dust, MBB}}$. The partition function Q is given by:

$$Q = \sum_J (2J + 1) \exp\left[-\frac{h}{k_B T_{\text{ex}}} (BJ(J + 1))\right], \quad (2.9)$$

where $B = 55101.011$ MHz is the rotational constant for ^{13}CO , $B = 54891.420$ MHz for C^{18}O , and $B = 46586.867$ MHz for N_2H^+ (Pickett et al. 1998). While the optical depth of N_2H^+ could be determined directly by comparing the strength of the individual hyperfine components, we need to apply the “detection equation” in order to derive the optical depth of the CO lines:

$$T_B = T_0 \left[f(T_{\text{ex}}) - f(T_{\text{bg}}) \right] \left[1 - e^{-\Delta\tau} \right], \quad (2.10)$$

where $f(T) \equiv (\exp(T_0/T) - 1)^{-1}$, $T_{\text{bg}} = 2.73$ K, and T_B taken as the peak value of the Gaussian fits.

One-dimensional profiles of the resulting maps have been obtained by azimuthally averaging around the core centers. In case of asymmetries, a segment of the circle in this direction has been masked for the averaging task. The regions which have been taken into account for the derivation of the 1D-profiles are indicated in Figs. 2.11 - 2.17.

2.C.2 RESULTS

The derived radial profiles of the molecular column densities of ^{13}CO , C^{18}O and N_2H^+ are presented in Figure 2.25. We find signs of depletion of ^{13}CO in all cores except for CB 4, which is the most tenuous core of the studied sample. The ^{13}CO column density of the other cores decreases constantly with the increasing hydrogen column density. The results for ^{13}CO are, however, affected by optical depth effects as well as deviations of the gas temperature from the LoS-averaged dust temperature and sub-thermal rotational excitation.

The derivation of C^{18}O column densities is less influenced by these effects since it is a rarer isotopologue (a factor of ~ 7 lower abundance as compared to ^{13}CO) and since its emission comes from more restricted regions with higher gas densities. The plots of the ^{13}CO column densities vs. visual extinction (top left panel of Fig. 2.25) yield a remarkable difference to those of the C^{18}O column densities. The relative abundance of ^{13}CO drops continuously with increasing extinction indicating central depletion of this species. While this behavior is also found for C^{18}O , its relative abundance also drops toward low hydrogen column densities and peaks between an A_V of 5 to 10 mag. The drop toward lower extinction could be explained by a weaker self-shielding of this rare isotopologue which in turn would lead to photo dissociation of C^{18}O in the envelopes where ^{13}CO is already well shielded. The chemical modeling,

however, suggests that the UV-radiation is already attenuated by several magnitudes in these regions compared to the nominal strength of the ISRF (see Sect. 2.4.4). The difference of the profiles of both species becomes more obvious from the ratio of both column densities. The ratio $N(^{13}CO)/N(C^{18}O)$ decreases continuously with increasing hydrogen column density in all starless cores. Interestingly, it even drops below the usually assumed ratio of 7 for the interstellar medium (ISM). The change of the $N(^{13}CO)/N(C^{18}O)$ ratio could thus not only be due to different self-shielding of both species but also partly due to reactions that increase the abundance of $C^{18}O$ with respect to ^{13}CO due to ion-molecule exchange reactions in cold and dense environments (e.g., Langer et al. 1984).

Where the N_2H^+ emission is strong enough to fit the hyperfine-structure, we also derive column densities for this molecule. We find that the ratio $N(N_2H^+)/N_H$ is roughly constant within the globules (see bottom row of Fig. 2.25). This finding is in contrast to the results of our advanced approach using chemical modeling and a subsequent line-radiative transfer. There we find depletion of N_2H^+ in the centers of the majority of the globules (see Sect. 2.4.4 and Fig. 2.6). This demonstrates the limitation of the often used LOS-averaged analysis.

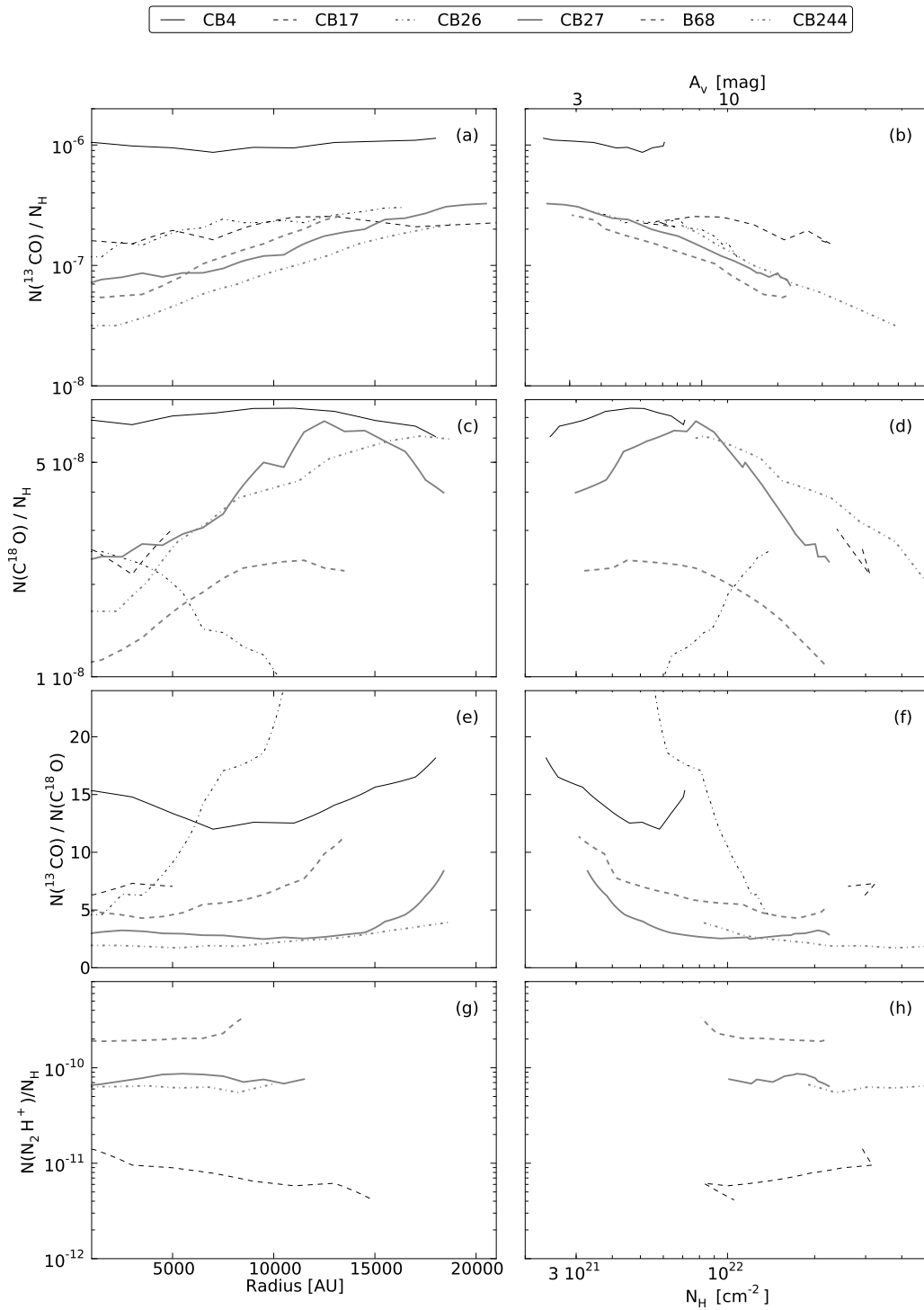


Figure 2.25: Results from the LTE-analysis. Plotted are (a) the relative column densities of ^{13}CO against radius, (b) and against the hydrogen column density, (c) the relative column densities of C^{18}O against radius, (d) and against the hydrogen column density, (e) the ratios of $N(^{13}\text{CO})/N(\text{C}^{18}\text{O})$ are plotted against radius, (f) and against the hydrogen column density, (g) the relative column densities of N_2H^+ against radius, (h) and against the hydrogen column density. The column densities of N_2H^+ in CB 4 and CB 26 could not be derived, since the emission in these globules is too weak and are for this reason missing in the plots.

MODELING OF DUST TEMPERATURE DISTRIBUTIONS IN STARLESS CORES

This Chapter is adapted from the paper Lippok, Launhardt, Robitaille, et al. (in prep.)

3.1 INTRODUCTION

Stars form in cold and dense molecular cloud cores which are observed in extinction at optical and up to mid-infrared wavelengths against the light of background stars and the extended PAH emission of the Galactic plane, and only emit themselves in the far infrared and at longer wavelengths. While most information on these cold objects has so far been obtained from ground-based observations of the continuum and spectral line (sub-)mm emission, the bulk of the thermal dust radiation – which is emitted in the far infrared (FIR) – is not accessible from the ground. Moreover, the thermal radiation of the cold dust (10-15 K) peaks in the the FIR. Therefore, it is hardly possible to constrain the dust temperature of the cores from observations without measuring their FIR emission. So far, uncertainties in the dust temperature have also led to large uncertainties in the density structure derived purely from (sub-)mm observations.

With the *Herschel*¹ space observatory (Pilbratt et al. 2010) and its PACS (Poglitsch et al. 2010) and SPIRE (Griffin et al. 2010) photometers it has for the first time become possible to resolve nearby starless cores in the FIR and observe their thermal dust emission with high sensitivity. As part of the *Herschel* guaranteed time key project "Earliest Phases of Star Formation" (EPoS), a sample of seven low-mass starless cores located in Bok globules has been observed with a sensitivity only limited by the confusion noise. Optical-depth-averaged dust temperature and column density maps of these sources have been derived from modified black-body fits to the thermal emission (Launhardt et al. 2013; Stutz et al. 2010). The same

¹*Herschel* is an ESA space observatory with science instruments provided by European-led Principal Investigator consortia and with important participation from NASA.

technique is also regularly applied to other objects as for instance infrared dark clouds (e.g., Pitann et al. 2013) or filaments (e.g. Palmeirim et al. 2013).

Thanks to their isolation and relatively simple structure, the starless cores of the EPoS sample allow to go one step further and to constrain the dust temperature variations along the line-of-sight from the dust continuum radiation. For this purpose a ray-tracing technique has been developed and radial dust temperature and hydrogen density profiles of the starless cores in the EPoS sample have been derived (Nielbock et al. 2012; Lippok et al. 2013; Schmalzl et al. submitted). It was found that low-mass prestellar cores typically exceed hydrogen densities of 10^5 cm^{-3} and cool down in the core centers to 8 – 12 K.

The derived structure of the cores depends on the dust opacity models used. However, neither the exact composition of the grains is known nor is the size distribution. Moreover, it is expected that the dust grains and in turn the dust opacity evolve at the high densities and low temperatures in starless cores (e.g., Ossenkopf & Henning 1994; Ormel et al. 2011). Coagulation can lead to larger grains and the disappearance of the smallest grains, and molecular freezeout results in ice layers on the surface of the grains favoring coagulation further. We are currently trying to constrain the dust properties in these cores by combining the NIR extinction and FIR/(sub-)mm emission maps. Here, we evaluate if and which combinations of dust model and ISRF lead to an equilibrium temperature distribution in the cores that agrees with the observationally based temperature structure of the globules. For this purpose, we derive dust temperature and density profiles with the ray-tracing technique for seven dust models. We then use radiative transfer modeling to calculate the equilibrium temperature structure for these density profiles and the corresponding dust models. By comparing the temperature structures of both methods, we also test the reliability of the ray-tracing technique.

The Chapter is outlined as follows. In Section 3.2, we describe the data used in this study. We then describe the modeling approaches in Section 3.3. In Section 3.4, we present the results for the dust temperature and hydrogen density profiles derived with the ray-tracing method from the continuum observations and we compare them to continuum radiative transfer models. We discuss the results in Section 3.5 and conclude in Section 3.6.

3.2 DATA

We use maps of continuum observations of the PACS $100 \mu\text{m}$, $160 \mu\text{m}$, and SPIRE $250 \mu\text{m}$, $350 \mu\text{m}$, and $500 \mu\text{m}$ bands that were obtained as part of the *Herschel* guaranteed time key project "Earliest Phases of Star formation" (EPoS) and are presented in Launhardt et al. (2013). These observations are complemented by ground-based (sub-)mm observations that are presented in Launhardt et al. (2010, 2013) and references therein. We also make use of near-infrared (NIR) extinction maps that were derived according to Kainulainen et al. (2006) from NIR observations with the Omega-2000 wide field camera at the Calar Alto 3.5 m tele-

Table 3.1: Source list

Source	Other names	R.A., Dec. (J2000) ^a [h:m:s, °:':"]	Region	Dist. [pc]	Ref.
CB 4	...	00:39:05.2, +52:51:47	Cas A, Gould Belt (GB)	350 ± 150	1,2
CB 17 ^b	L 1389	04:04:37.1, +56:56:02	Perseus, GB	250 ± 50	2,3,1
CB 26 ^c	L 1439	05:00:14.5, +52:05:59	Taurus-Auriga	140 ± 20	2,3,4,5
CB 27	L 1512	05:04:08.1, +32:43:30	Taurus-Auriga	140 ± 20	2,4,5
B68	L 57, CB 82	17:22:38.3, -23:49:51	Ophiuchus, Pipe nebula	135 ± 15	2,6,7,8
CB 244 ^d	L 1262	23:25:26.8, +74:18:22	Cepheus flare, GB	200 ± 30	2,3,4,9

Notes. ^(a) These are the positions of the center of the starless cores. They are defined as column density peaks found in Launhardt et al. (2013). ^(b) CB 17: additional low-luminosity Class I YSO 25'' from starless core. ^(c) CB 26: additional Class I YSO 3.6' south-west of the starless core. ^(d) CB 244: additional Class 0 source ~ 90'' east of starless core.

References. (1) Perrot & Grenier (2003); (2) Launhardt et al. (2013); (3) Launhardt et al. (2010); (4) Loinard et al. (2011); (5) Stutz et al. (2009); (6) de Geus et al. (1989); (7) Lombardi et al. (2006); (8) Alves & Franco (2007); (9) Kun (1998).

scope in 2010. These observations are so far unpublished.

3.3 MODELING

3.3.1 DUST MODELS

One major unknown in the modeling of the thermal dust emission are the dust opacities. In the previous papers where our team has used the ray-tracing technique (Nielbock et al. 2012; Lippok et al. 2013), we have assumed a dust model of Ossenkopf & Henning (1994) assuming composite grains of silicates and amorphous carbon with thin ice layers and a coagulation time of 10^5 yr (in the following called OH5a²). However, large parts of the envelopes have lower densities and higher temperatures that do not necessarily imply significant coagulation and ice layers on the dust grains. For this reason, we expand our analysis in this chapter to additional dust models (Table 3.2). We consider two further models of Ossenkopf & Henning (1994): uncoagulated dust grains (i.e. grains with MRN size distribution; Mathis et al. 1977) without ice layers (in the following called OH1) and uncoagulated dust grains with thin ice layers (in the following called OH4). The dust opacities of Ossenkopf & Henning (1994) have only been calculated for wavelengths down to $1.25 \mu\text{m}$. We extrapolate them to shorter wavelengths according to Cardelli et al. (1989, Eq. 1, Tab. 3, Col. 5) up to the optical regime and to even lower wavelengths by extrapolating the shape of the curve. The dust opacities of

²Note that this opacity model is different from the often used OH5 model which assumes coagulation at a density of 10^6 cm^{-3} . It is not tabulated in the paper but available on-line at <ftp://cdsarc.u-strasbg.fr/pub/cats/J/A+A/291/943>.

Ossenkopf & Henning (1994) only take into account absorption. We therefore augment them with the albedo of the WD3.1 model (see below) following the approach of Young & Evans (2005).

In addition, we test three dust models presented in Ormel et al. (2011). The grains of these models are composed by silicates and graphite. One model, which we hereafter call Ormel1a, considers a mixture without ice layers at a short coagulation time of 3×10^4 yr at a hydrogen density of 10^5 cm^{-3} . The other two models consider a mixture of icy silicates and graphites but different coagulation times of 3×10^4 yr and 10^6 yr at a hydrogen density of 10^5 cm^{-3} . Hereafter, we call them Ormel4a and Ormel4d, respectively. Finally, we also test the model of Weingartner & Draine (2001) for ISM dust ($R_V = 3.1$, in the following called WD3.1).

The mass extinction coefficients and albedo of all dust models are plotted in Fig. 3.1. In the FIR and (sub-)mm range all dust opacity models follow roughly a power-law with a spectral index β between 1.8 and 2.0 but with offsets of the absolute values (see Tab. 3.2).

Some of the models are unlikely to describe the dust population in the dense cores properly, most of all WD3.1 which has been derived for the diffuse ISM, but also OH1 and Ormel1a which both have no ice-layers. Here we test, if this is reflected in the agreement between the equilibrium temperature distributions assuming the respective dust models and the corresponding temperature profiles derived with the ray-tracing technique.

3.3.2 THE RAY-TRACING METHOD

The continuum emission of the globules has been observed in 8 bands ranging from $100 \mu\text{m}$ to 1.2 mm. Our team has developed a ray-tracing algorithm that can restore the dust temperature and density distribution along the line-of-sight (LOS) in starless cores and thus provide the full 3-dimensional dust temperature and density structure, at least for sources with only moderate deviations from spherical symmetry. The data are prepared in the same way as described in Launhardt et al. (2013) for the modified black-body fitting, which actually comprises the first step of the iterative ray-tracing method used here. The latter is explained in detail in Nielbock et al. (2012) and results for globules containing starless cores are presented in Nielbock et al. (2012), Lippok et al. (2013) and Schmalzl et al. (submitted). In these papers, OH5a dust was used for all cores. Here, we present source models for a number of different dust opacity models. In the following, we briefly describe the profile formulae used for the ray-tracing method to illustrate the meaning of the profile parameters.

We describe the hydrogen density profiles with a modified "Plummer"-like profile (Plummer 1911). These profiles describe power-laws that flatten towards the center. Since we find that the hydrogen densities (and column densities) do not drop like a power-law at the cloud edge, but instead level out into a flat-density (to first order) halo around the globules, we add a

Table 3.2: Dust models considered in this paper

Name	Description	$\kappa_{250\mu\text{m}}$ [cm^2/g]	β^a	Reference
OH1 ^b	uncoagulated dust ^c , no ice	6.77	1.87	1
OH4 ^b	10^5 yr, $n_{\text{H}} = 10^5 \text{ cm}^{-3}$, no ice	10.86	1.86	1
OH5a ^b	10^5 yr, $n_{\text{H}} = 10^5 \text{ cm}^{-3}$, thin ice layers	14.16	1.82	1
WD3.1	dust of the ISM with $R_V = 3.1$	4.02	2.00	2
Ormel1a	"(sil,gra)", 3×10^4 yr, $n_{\text{H}} = 10^5 \text{ cm}^{-3}$	13.98	1.66	3
Ormel4a	"ice-sil+gra", 3×10^4 yr, $n_{\text{H}} = 10^5 \text{ cm}^{-3}$	7.16	2.04	3
Ormel4d	"ice-sil+gra", 10^6 yr, $n_{\text{H}} = 10^5 \text{ cm}^{-3}$	25.89	1.80	3

Notes. (a) The power law was fitted to the opacity models in the range of $100 \mu\text{m}$ to 1 mm . (b) Note that the OH models use amorphous carbon (cf. Preibisch et al. 1993) instead of graphite for the carbonaceous component. (c) MRN size distribution.

References. (1) Ossenkopf & Henning (1994); (2) Weingartner & Draine (2001); (3) Ormel et al. (2011)

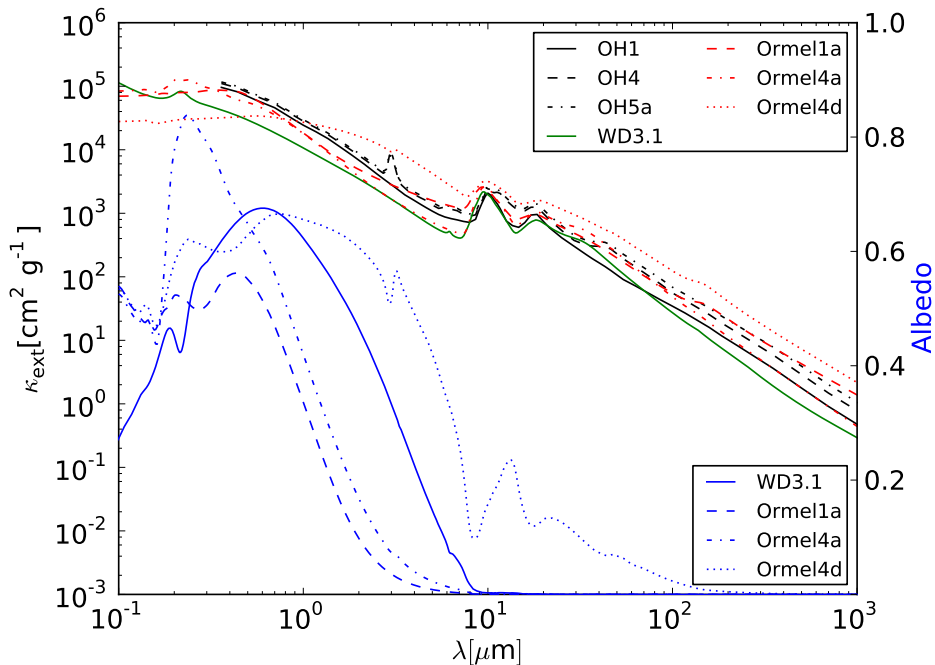


Figure 3.1: Mass extinction coefficients of the considered dust models (*left abscissa*), and the albedos of the models by Ormel et al. (2011) and Weingartner & Draine (2001). The albedo of the WD3.1 model is also adopted for the OH models (*right abscissa*).

corresponding term to the profile. It then reads

$$n_{\text{H}}(r) = \frac{\Delta n}{\left(1 + \left(\frac{r}{r_0}\right)^2\right)^{\eta/2}} + n_{\text{out}} \quad \text{if } r \leq r_{\text{out}} \quad (3.1)$$

where $n_{\text{H}} = 2 \times n(\text{H}_2) + n(\text{H})$ is the total number density of hydrogen nuclei. The radius r_{out} sets the outer boundary of the model cloud. The density beyond this radius is set to zero. This profile (i) accounts for an inner flat-density core inside r_0 with a peak density $n_0 = n_{\text{out}} + \Delta n$ ($\Delta n \gg n_{\text{out}}$), (ii) approaches a power-law with exponent η at $r \gg r_0$, (iii) turns over into a flat-density halo outside r_1 , where

$$r_1 = r_0 \sqrt{\left(\frac{\Delta n}{n_{\text{out}}}\right)^{2/\eta} - 1}, \quad (3.2)$$

and (iv) is cut off at r_{out} . The tenuous envelope is actually neither azimuthally symmetric nor fully spatially recovered by our observations of dust emission. Therefore, r_{out} is only estimated from the circularized $500 \mu\text{m}$ emission profiles and optical (DSS2) images that clearly show the extent of the cloudshine, stellar (ISRF) photons that are scattered at small dust grains in the halos (e.g., Foster & Goodman 2006).

We use an empirical temperature profile function that resembles the radiation transfer equation for an externally heated cloud. It couples the local temperature to the effective optical depth toward the outer "rim" at which the ISRF impacts:

$$T(r) = T_{\text{out}} - \Delta T \left(1 - e^{-\tau(r)}\right) \quad (3.3)$$

with $\Delta T = T_{\text{out}} - T_{\text{in}}$ and the frequency-averaged effective optical depth

$$\tau(r) = \tau_0 \frac{\int_r^{r_{\text{out}}} n_{\text{H}}(x) dx}{\int_0^{r_{\text{out}}} n_{\text{H}}(x) dx}. \quad (3.4)$$

τ_0 is an empirical (i.e. free) scaling parameter that accounts for the a priori unknown mean dust opacity and the spectral energy distribution of the UV radiation of the ISRF. T_{in} is the minimum, inner temperature, and is determined by heating from the ISRF.

3.3.3 RADIATIVE TRANSFER MODELING

The temperature distribution in the cores is a result of heating and cooling processes. We use the Monte-Carlo continuum radiative transfer code HYPERION (Robitaille 2011) to calculate equilibrium temperature distributions of the starless cores assuming the density profiles that have been derived with the ray-tracing technique.

We vary two parameters in the modeling process. First, we vary the NIR extinction $A_K(r_{\text{sym}})$ at the radius r_{sym} up to which we consider the globules as spherically symmetric. The values of r_{sym} are listed in Table 3.3 for all globules. $A_K(r_{\text{sym}})$ is constrained from NIR extinction maps and we list the mean values and the uncertainties in Table 3.3 that we have derived from the NIR observations. The uncertainty of $A_{K,\text{obs}}(r_{\text{sym}})$ defines the range of $A_K(r_{\text{sym}})$ that we consider in the modeling. We model the extinction of the ISRF at r_{sym} by adding a corresponding envelope around the cores. This is realized by cutting off the density profile at a radius r_{out} such that the hydrogen column density at r_{sym} corresponds to the correct extinction. Both are linked via

$$A_K(r_{\text{sym}}) = 2.5 \log_{10}(e) m_H \frac{m_d}{m_H} \kappa_{2.2\mu\text{m}} N_{\text{H},\text{rout}}(r_{\text{sym}}), \quad (3.5)$$

where m_H is the hydrogen atom mass, m_d/m_H is the mass ratio of dust and hydrogen, $\kappa_{2.2\mu\text{m}}$ is the mass extinction at $2.2 \mu\text{m}$, and $N_{\text{H},\text{rout}}(r_{\text{sym}})$ is the hydrogen column density along the line-of-sight (LOS) at r_{sym} depending on the chosen r_{out} . It is calculated by integrating along the LOS over the Plummer-like density profile.

Second, we vary the total power of the ISRF by multiplying its SED by a factor s_{isrf} . The ISRF is the main heating source of the dust in the starless globules studied here. Short-ward of $10 \mu\text{m}$ it is dominated by stellar photons. The radiation at longer wavelengths consists of stellar radiation that has been reprocessed by the ISM. Mathis et al. (1983) derived a total flux of $0.0217 \text{ erg cm}^{-2} \text{ s}^{-1}$ for the ISRF at wavelengths below $9 \mu\text{m}$ in the solar neighborhood. For the shape of the ISRF, we adopt the model of Porter & Strong (2005) at the position of the sun. It is plotted in Fig. 3.2. This spectrum contains about 25% of its energy at wavelengths above $9 \mu\text{m}$ and so we normalize it to a total flux of $0.0290 \text{ erg cm}^{-2} \text{ s}^{-1}$. Evans et al. (2001) pointed out that the ISRF is the by far dominating heating effect for dust particles and all other effects, like direct heating of the dust by cosmic rays, heating by secondary UV-photons produced by scattering of cosmic rays and heating of the dust by collisions with the gas, are negligibly small. However, Goldsmith (2001) modeled the effect of collisional coupling of dust and gas and found that it can increase the dust temperature by about 1-2 K in the center of starless cores. We consider the ISRF as the only heating source in the modeling. But we keep in mind that the dust in the core centers might be heated additionally from collisions with the gas. Since the ISRF varies locally and its exact shape at the location of the target cores is unknown we treat s_{isrf} as free parameter.

We also test, if the agreement between the ray-tracing results and the radiative transfer models varies for the different considered dust models. For this purpose, we run the radiative transfer models for each globule for all dust models listed in Table 3.2 and assume the respective density Plummer-profiles that have been derived with the ray-tracing technique.

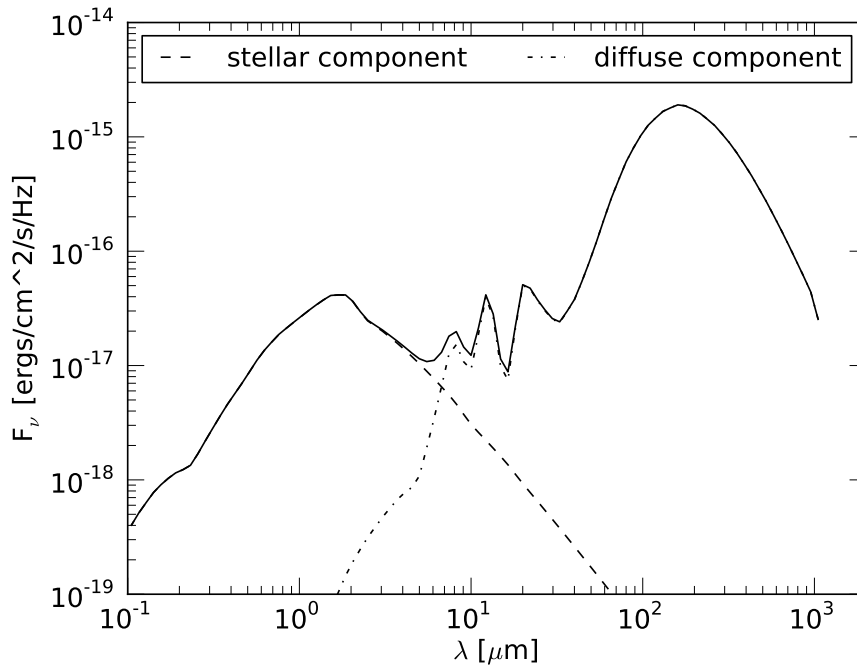


Figure 3.2: Stellar and diffuse component of the ISRF that we adopt for the modeling. The shape is adopted from Porter & Strong (2005) for the solar neighborhood. We normalize the total flux to $0.0290 \text{ erg/cm}^2/\text{s}$ according to Mathis et al. (1983).

3.4 MODELING RESULTS

3.4.1 DENSITY AND TEMPERATURE PROFILES DERIVED WITH THE RAY-TRACING TECHNIQUE

We have derived dust temperature and hydrogen density maps of six starless cores for seven different dust opacity models. Temperature maps derived using the OH5a dust model have been shown in Lippok et al. (2013) (and Appendix 2.B of Chapter 2 of this thesis). Here we only present radially averaged profiles, because the radiative transfer modeling is also done with the assumption of spherical symmetry. In Fig. 3.3 we demonstrate the dependence of the dust temperature and hydrogen density profiles on the assumed dust model with the example of B 68. The shape of the density and temperature profiles is very similar for all dust models. This is a consequence of the similar shape of the dust opacities in the FIR and (sub-)mm regime. The central density is anti-correlated with the absolute value of the (sub-)mm opacity and with the central temperature, as can be seen by comparing Fig. 3.3 and Tab. 3.2. The outer temperature which is similar to the temperature derived by modified black-body fits is anti-correlated to the spectral emissivity index β .

In Fig. 3.4 we plot fits to the hydrogen density, hydrogen column density, and the temperature

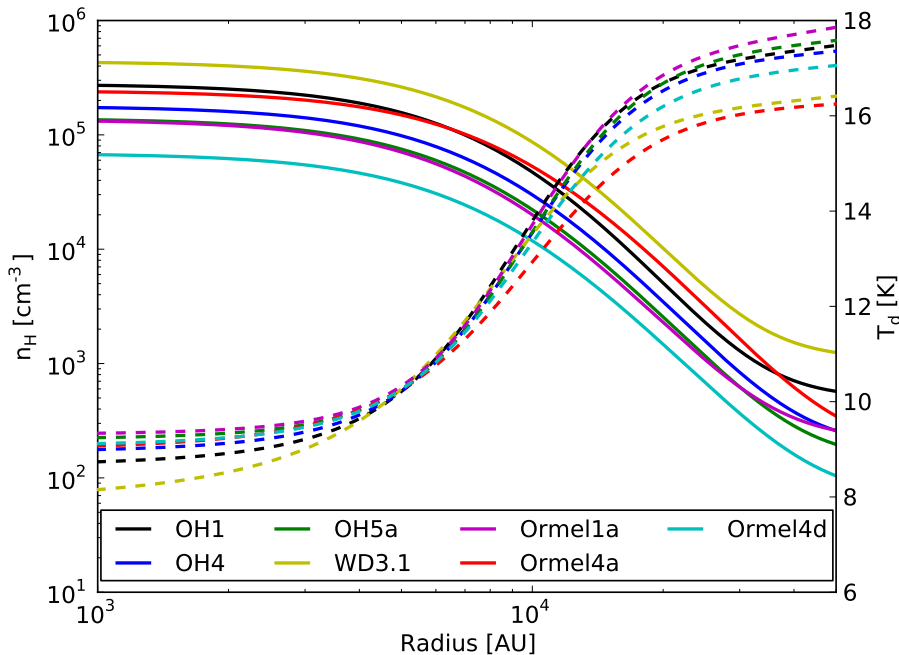


Figure 3.3: Radial hydrogen density (solid lines) and dust temperature profiles (dashed lines) of B 68 for the considered dust models (see Sec. 3.3.1). The profiles are described according to Equations (3.1) and (3.3) and have been derived with the ray-tracing method.

profiles of all globules which were derived with the ray-tracing technique assuming OH5a dust. We only plot the profiles up to their respective r_{sym} . The density and column density profiles were fitted to the radially averaged map points using a Plummer-like profile according to Equation 3.1. The temperature structure can be well fitted by profiles obeying Equation 3.3. The effect of using other dust models is very similar to what is shown for B 68 in Fig. 3.3.

3.4.2 COMPARISON OF DUST RADIATIVE TRANSFER MODELS TO RAY-TRACING RESULTS

We apply radiative transfer modeling to calculate the equilibrium dust temperature distributions of the globules for the density distributions that have been derived with the ray-tracing technique. Before presenting the results for all globules, we show for the example of B 68 the effects of using different dust models and of varying s_{isrf} and $A_{\text{K}}(r_{\text{sym}})$.

EFFECT OF USING DIFFERENT DUST MODELS

We demonstrate the effect of using different dust opacity models for the example of B 68. We calculated the equilibrium dust temperature distributions for all dust models and the corresponding density profiles as they were derived with the ray-tracing technique in Fig. 3.3.

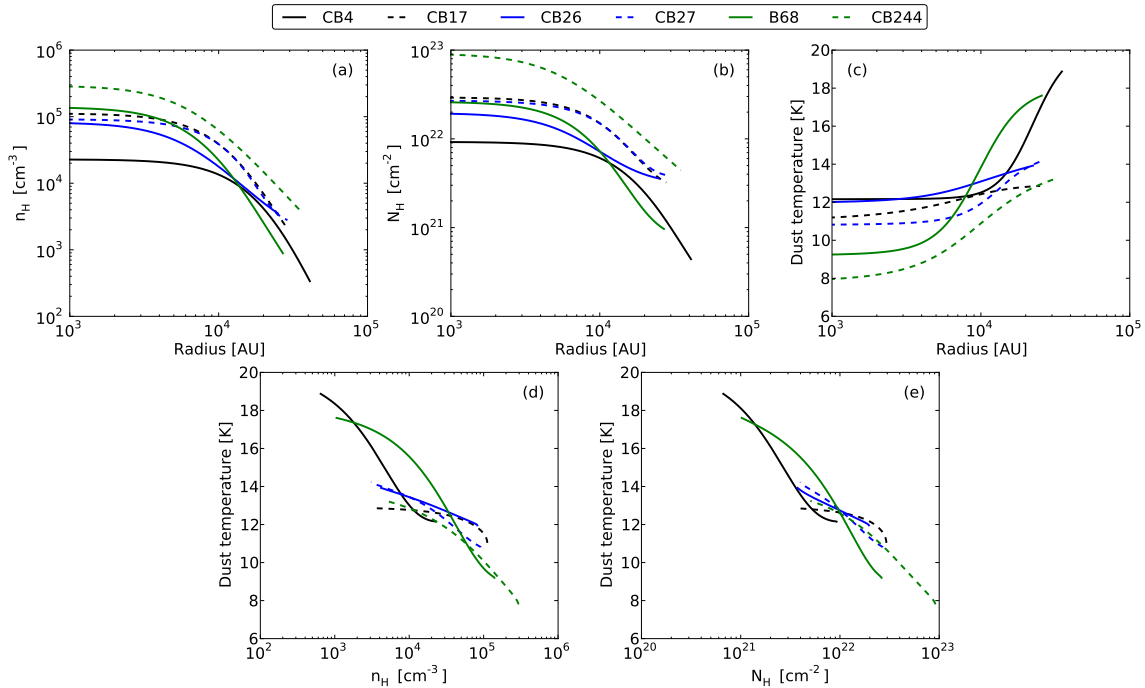


Figure 3.4: Radial profiles derived with the ray-tracing technique assuming OH5a dust plotted up to r_{sym} . (a) Hydrogen density vs. radius, (b) hydrogen column density vs. radius, (c) temperature profiles vs. radius, (d) temperature profile vs. hydrogen density, (e) temperature profile vs. hydrogen column density.

We find that the temperature distributions derived with the radiative transfer modeling do not depend strongly on the assumed dust models, as it was found with the ray-tracing method. This is demonstrated in Fig. 3.5. We show the temperature profiles derived with radiative transfer calculations for all dust models that fit the corresponding ray-tracing results best. In this example we have fixed $A_K(r_{\text{sym}})$ for all dust models to the mean value that is found by NIR extinction mapping (Tab. 3.3). The scaling factor for the ISRF s_{isrf} is 2.0 or 2.5 for all models. Considering the uncertainties in the density and temperature profiles derived with the ray-tracing technique, all dust models – even those which are not expected to be appropriate for the dense and cold cores like OH1 or WD3.1 – lead to good agreements between the temperature profiles derived with the ray-tracing technique and their counterparts derived with the radiative transfer modeling. A systematic difference in the temperature structure is only found for Ormel4d dust, because it has a much smaller visual extinction than the other dust models and at the same time a higher (sub-)mm opacity, so that the heating of the outer envelope by the ISRF is less efficient and the energetic part of the ISRF can penetrate deeper into the core leading to a flatter temperature profile. We also tested the importance of scattering and have run a few models for which the albedo was set to zero. We find that scattering has only a very small (less than 0.5 K difference) effect in the cores up to r_{sym} . At the edges of the models where the unattenuated ISRF impacts onto the cloud, the effect is stronger. The extent of the globules is, however, not well constrained by the *Herschel* observations and the low density material at the cloud edges is also not well described by assuming spherical symmetry.

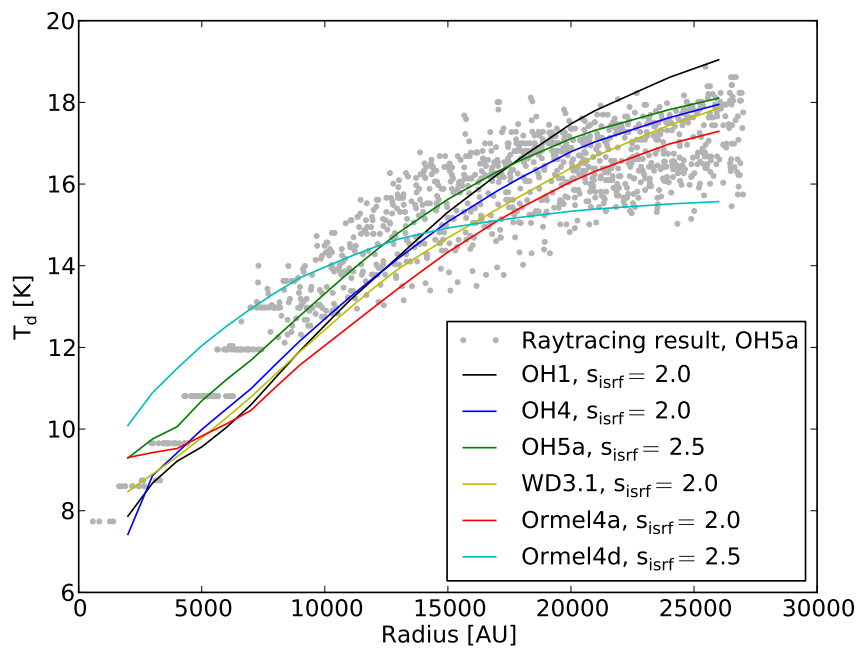


Figure 3.5: Dependence of the radiative transfer results on the dust properties shown for B 68. The dots indicate the ray-tracing result of OH5a dust. The variation between the temperature profiles derived with the ray-tracing technique vary negligibly for different dust models (see Fig. 3.3). The lines show the radiative transfer results for the various dust models that match the ray-tracing results best for $A_K(r_{\text{sym}}) = 0.10$ mag which is the value derived from NIR extinction mapping (see Table 3.3).

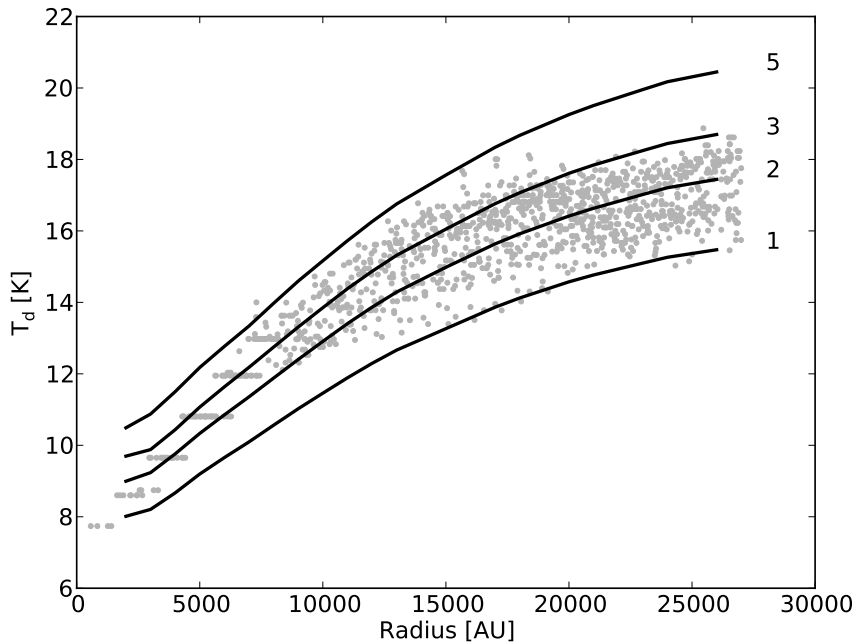


Figure 3.6: Effect of increasing the total flux of the ISRF by up to a factor 5. Example of B 68 assuming OH5a dust and $A_K(r_{\text{sym}}) = A_{K,\text{obs}}(r_{\text{sym}})$.

Therefore, we do not take the outer part of the globules into account for the comparison of the temperatures.

EFFECT OF VARYING THE TOTAL FLUX OF THE ISRF

The effect of scaling the ISRF is illustrated in Fig. 3.6. We compare dust temperature profiles calculated with radiative transfer modeling. We used OH5a dust and left $A_K(r_{\text{sym}})$ fixed but varied the scaling parameter of the ISRF s_{isrf} from 1 to 5. The predicted temperature structure is sensitive to the power of the ISRF everywhere. We find that the ray-tracing results are matched best for an ISRF that is increased by a factor of about 2 with respect to the local value of the total flux of $0.0290 \text{ erg cm}^{-2} \text{ s}^{-1}$. This tendency is also found for the other globules as we show later.

EFFECT OF VARYING THE EXTINCTION OF THE ENVELOPE

The dependence of the temperature structure on the assumed envelope extinction $A_K(r_{\text{sym}})$ is shown in Fig. 3.7. We compare radiative transfer results for models of B 68 assuming OH5a dust and $A_K(r_{\text{sym}}) = 0.1 \text{ mag}, 0.2 \text{ mag}, 0.3 \text{ mag}, 0.5 \text{ mag}$. The first value was derived in NIR-extinction measurements. In contrast to varying the total power of the ISRF, changing $A_K(r_{\text{sym}})$

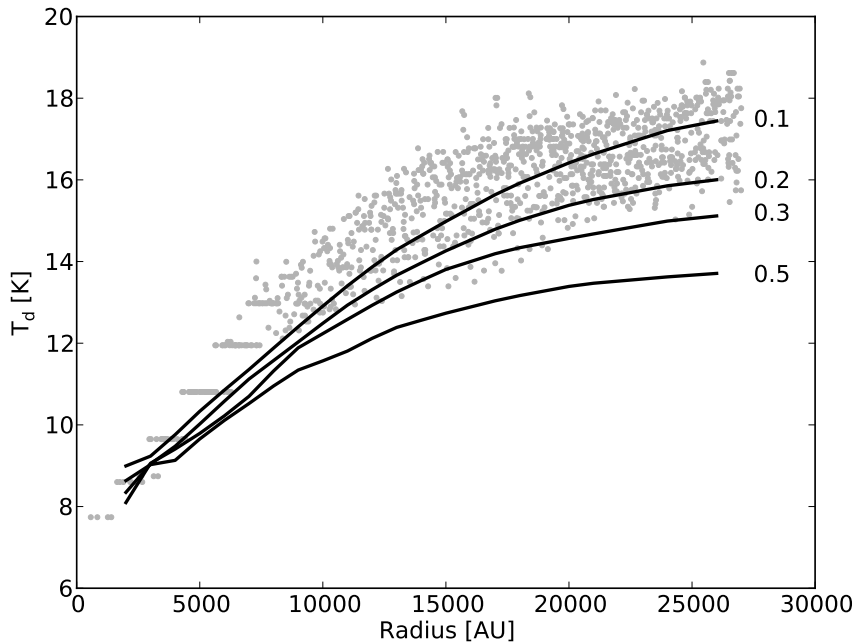


Figure 3.7: Effect of increasing $A_K(r_{\text{sym}})$ from 0.1 mag to 0.5 mag. This example shows temperature profiles of B 68 calculated for OH5a dust and $s_{\text{isrf}} = 2.5$.

mainly influences the temperature at large radii. In the inner 10,000 AU the models are nearly identical. This is because the outer layers of the core absorb the short-wavelength range of the ISRF and only the IR part which is much less affected by extinction in the envelope reaches the core centers.

COMPARISON FOR ALL GLOBULES

Figs. 3.8-3.13 show for all globules and six different dust models a comparison of the temperature profiles derived with the ray-tracing technique and those of the radiative transfer models that agree best with the ray-tracing results. The best models (assuming a free parameter s_{isrf} and by varying $A_K(r_{\text{sym}})$ within the uncertainties, see Table 3.3) have been found with χ^2 -fits. We assumed an uncertainty of the temperature structure of ${}_{-1}^{+2}$ K. This is the uncertainty of the ray-tracing method.

In general, the temperature profiles of the radiative transfer and the ray-tracing models are in good agreement with exception of the globule CB 17. The models for Ormel4d dust stand out because they lead to flatter temperature profiles than the other dust models. For CB 26 and CB 244 the Ormel4d models have the best agreement with the ray-tracing results. For CB 27 all dust models slightly underestimate the central temperature and the model using Ormel4d dust comes closest. The temperature profiles of CB 4 and B 68 are better described by the steeper profiles derived with all but the Ormel4d model.

Table 3.3: List of the outer radii r_{sym} for the comparison of ray-tracing and radiative transfer results and the NIR extinction observed there.

Object	r_{sym} [10^3 AU]	$A_{\text{K,obs}}(r_{\text{sym}})$ [mag]
CB 4	41	0.12 ± 0.11
CB 17	28	0.23 ± 0.03
CB 26	25	0.21 ± 0.09
CB 27	29	0.24 ± 0.11
B 68	27	0.10 ± 0.04
CB 244	35	0.34 ± 0.25

Table 3.4: List of values of s_{isrf} for which the temperatures derived by the ray-tracing and radiative transfer models agree. We list them separately for the core centers and r_{sym} and list the values possible for both locations. For comparison, we list the values for two dust models: OH5a and Ormel4d.

Object	OH5a			Ormel4d		
	$s_{\text{isrf}, r_{\text{sym}}}^a$	$s_{\text{isrf}, \text{center}}^b$	$s_{\text{isrf}, \text{both}}^c$	$s_{\text{isrf}, r_{\text{sym}}}^a$	$s_{\text{isrf}, \text{center}}^b$	$s_{\text{isrf}, \text{both}}^c$
CB 4	1.5 – 7	1.0 – 5	1.5 – 5	2.5 – 10	1.0 – 4.0	2.5 – 4.0
CB 17	0.5 – 1.0	5 – 20	–	0.5 – 2.0	2.5 – 25	–
CB 26	0.4 – 2.5	2.5 – 10	2.5	0.7 – 3.0	1.5 – 7.0	1.5 – 3.0
CB 27	0.7 – 5.0	5 – 15	5	2.0 – 4.0	2.0 – 15.0	2.0 – 4.0
B 68	1.0 – 4.0	1.0 – 7	1.0 – 4	2.5 – 7.0	0.5 – 3.0	2.5 – 3.0
CB 244	0.5 – 4.0	0.8 – 10	0.8 – 4	0.5 – 2.5	1.0 – 15	1.0 – 2.5
Mean values	0.8 – 3.9	2.6 – 11.3	2.2 – 4.1	1.5 – 4.8	1.4 – 11.5	1.9 – 3.3

Notes. ^(a) Ray-tracing and radiative transfer models compared between $r_{\text{sym}} - 2500$ AU and r_{sym} . ^(b) Ray-tracing and radiative transfer models compared between 2500 AU and 5000 AU. ^(c) Range of s_{isrf} which allows for good fits in the center and at r_{sym} . It might, however, require different values of $A_{\text{K}}(r_{\text{sym}})$ at both locations.

The best models are for all globules and dust models found for $s_{\text{isrf}} \sim 2 - 3$. They are plotted in Figs. 3.8-3.13. In Table 3.4 we list the values of s_{isrf} separately that allow for good matches of the temperature profiles in the core centers and around r_{sym} for Ormel4d dust and – representative for all other dust models which lead to steep profiles – for OH5a dust. We find that radiative transfer models using all dust models but the Ormel4d model have the tendency to predict steeper profiles than derived with the ray-tracing method. But even though the Ormel4d dust opacity is most different from the OH5a model compared to the other dust models, the range of s_{isrf} that allows for a good agreement between the temperature profiles derived with the ray-tracing method and the radiative transfer models is almost the same.

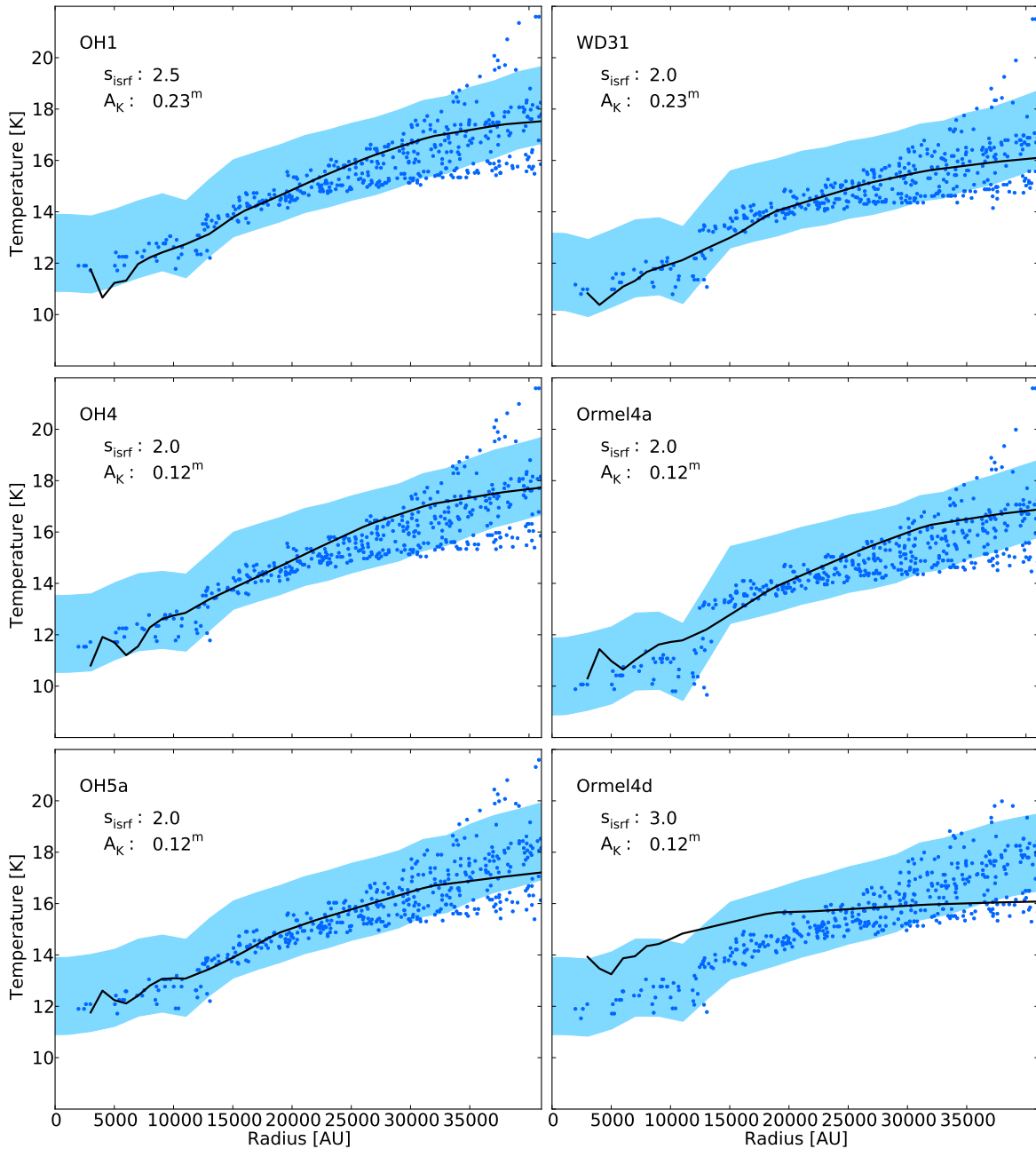


Figure 3.8: Comparison of ray-tracing and radiative transfer results of CB 4 for dust models as labeled in the plot. Each dot represents a pixel of the temperature map produced with the ray-tracing technique. The shadow indicates the uncertainty of the mean temperature profile which we estimate as ${}_{-1}^{+2}$ K. The black line shows the temperature profile of the best fitting radiative transfer model. Its parameters are indicated in the plots.

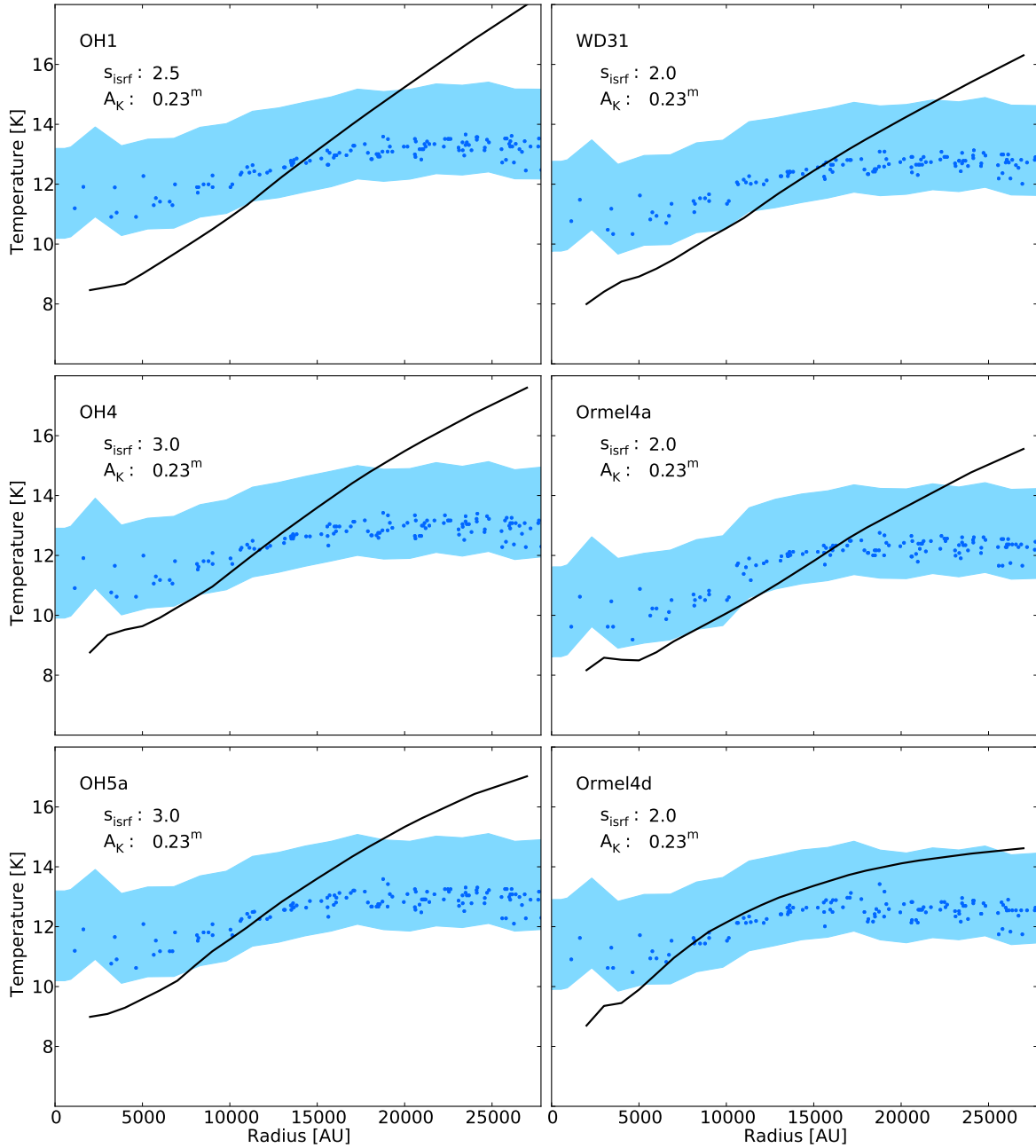


Figure 3.9: Comparison of ray-tracing and radiative transfer results of CB 17 for dust models as labeled in the plot. Each dot represents a pixel of the temperature map produced with the ray-tracing technique. The shadow indicates the uncertainty of the mean temperature profile which we estimate as ${}_{-1}^{+2}$ K. The black line shows the temperature profile of the best fitting radiative transfer model. Its parameters are indicated in the plots.

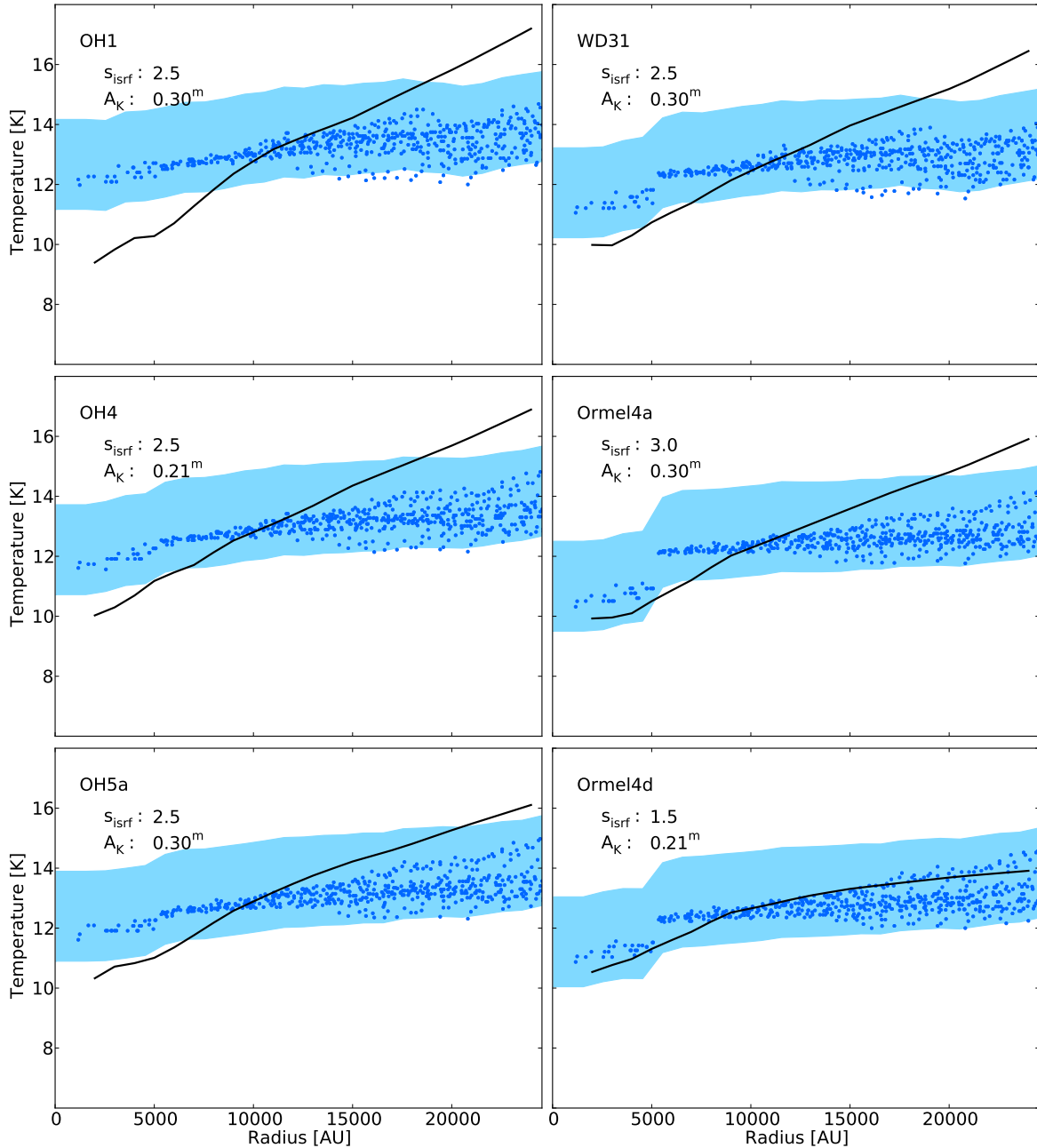


Figure 3.10: Comparison of ray-tracing and radiative transfer results of CB 26 for dust models as labeled in the plot. Each dot represents a pixel of the temperature map produced with the ray-tracing technique. The shadow indicates the uncertainty of the mean temperature profile which we estimate as $^{+2}_{-1}$ K. The black line shows the temperature profile of the best fitting radiative transfer model. Its parameters are indicated in the plots.

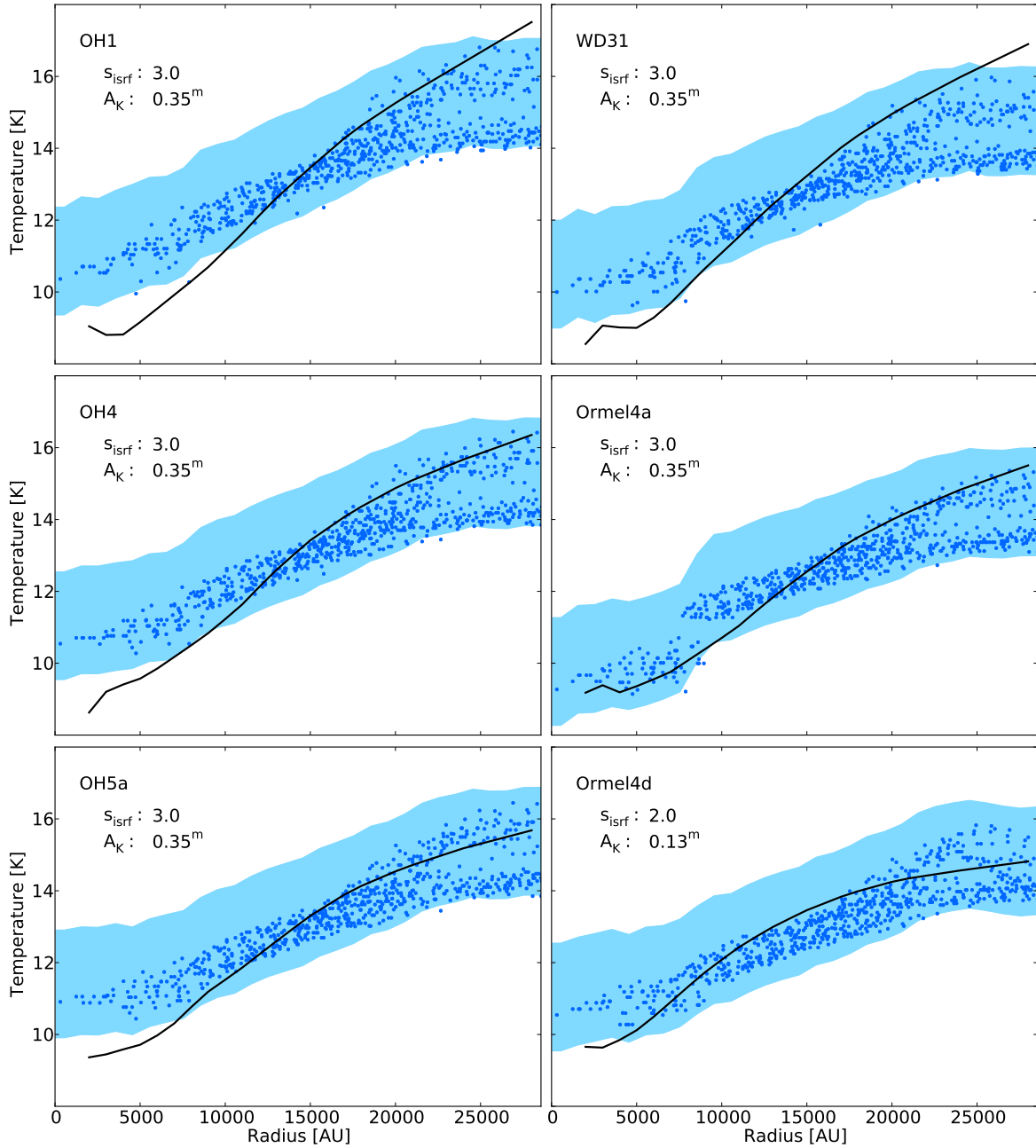


Figure 3.11: Comparison of ray-tracing and radiative transfer results of CB 27 for dust models as labeled in the plot. Each dot represents a pixel of the temperature map produced with the ray-tracing technique. The shadow indicates the uncertainty of the mean temperature profile which we estimate as $^{+2}_{-1}$ K. The black line shows the temperature profile of the best fitting radiative transfer model. Its parameters are indicated in the plots.

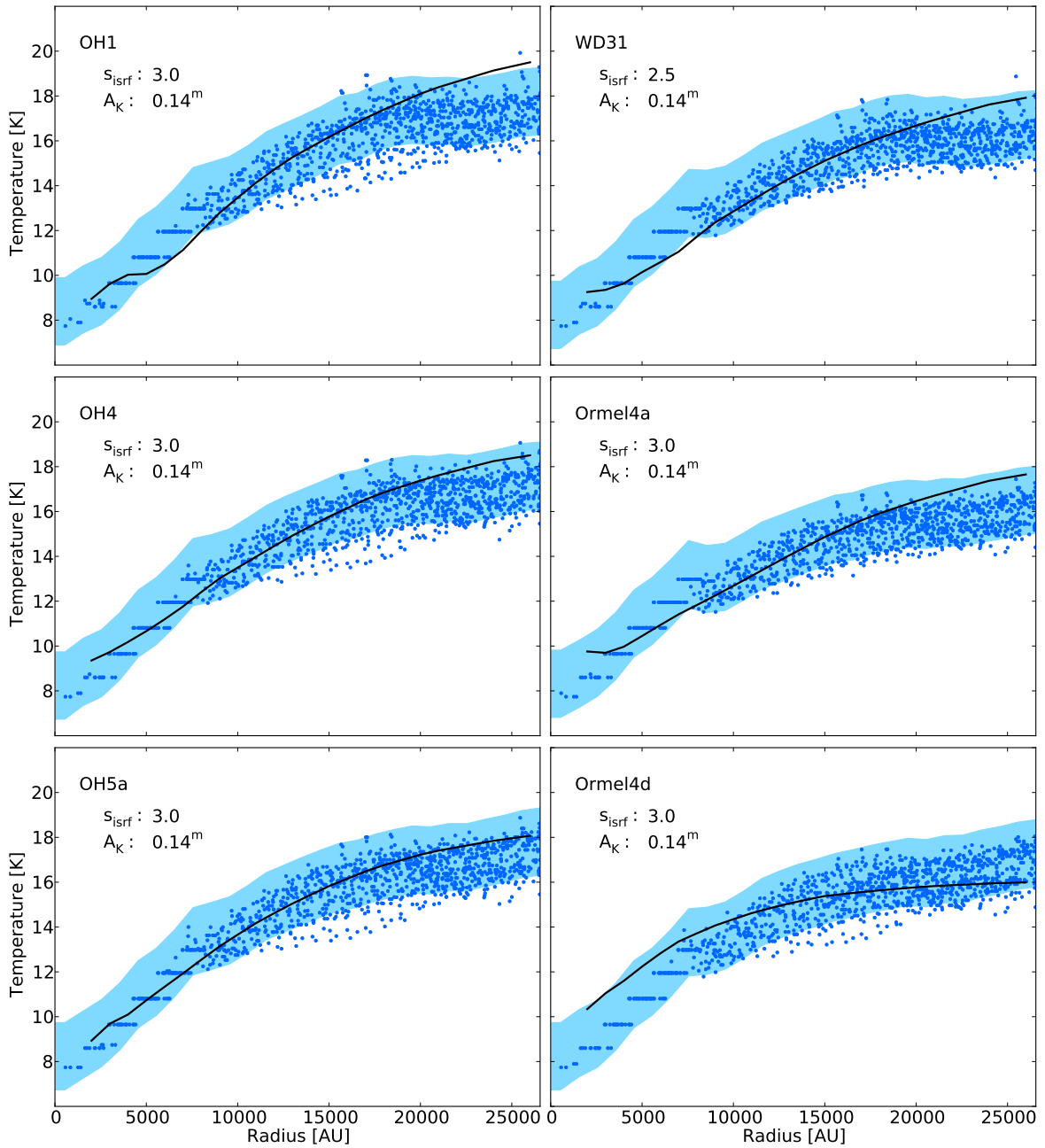


Figure 3.12: Comparison of ray-tracing and radiative transfer results of B 68 for dust models as labeled in the plot. Each dot represents a pixel of the temperature map produced with the ray-tracing technique. The shadow indicates the uncertainty of the mean temperature profile which we estimate as $^{+2}_{-1}$ K. The black line shows the temperature profile of the best fitting radiative transfer model. Its parameters are indicated in the plots.

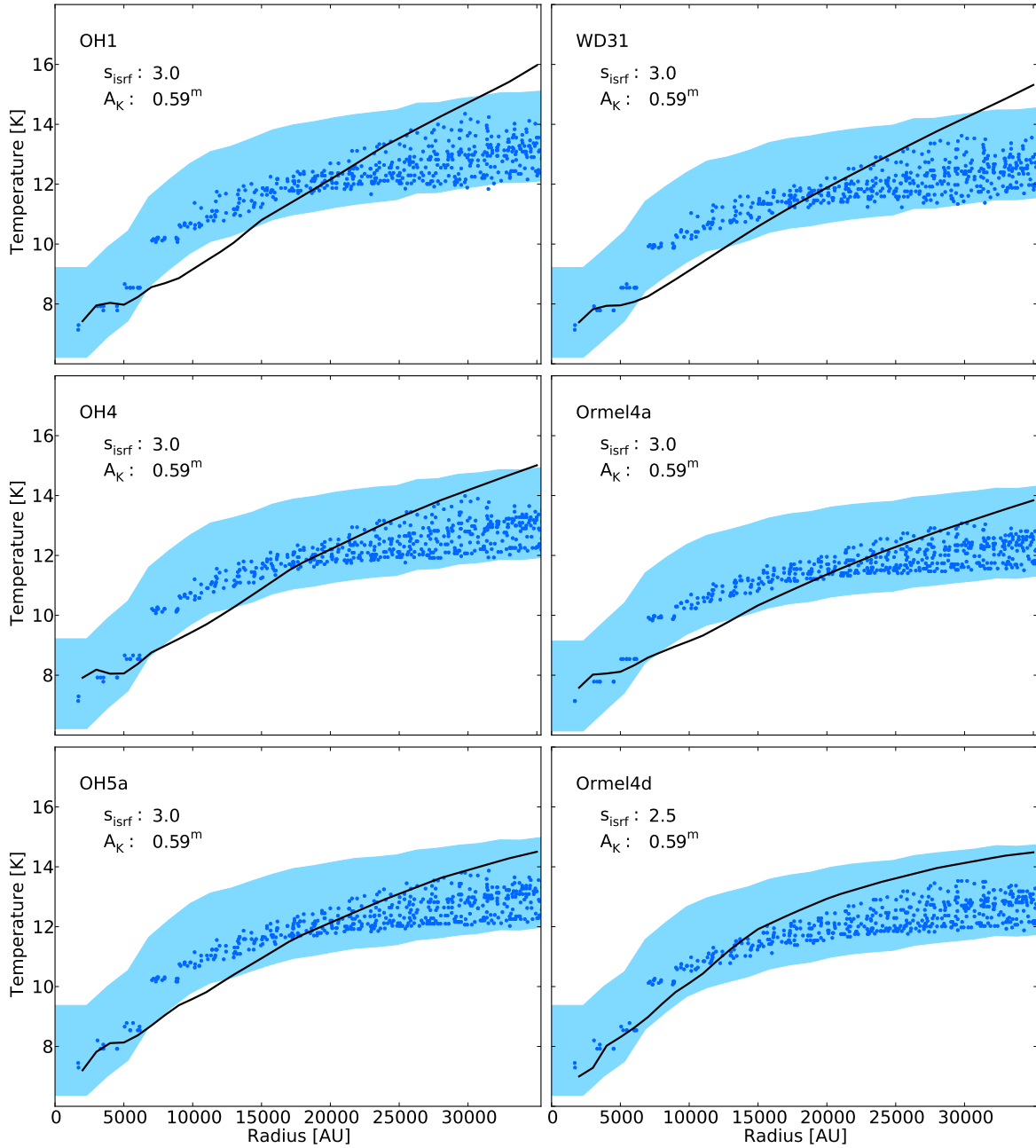


Figure 3.13: Comparison of ray-tracing and radiative transfer results of CB 244 for dust models as labeled in the plot. Each dot represents a pixel of the temperature map produced with the ray-tracing technique. The shadow indicates the uncertainty of the mean temperature profile which we estimate as $^{+2}_{-1}$ K. The black line shows the temperature profile of the best fitting radiative transfer model. Its parameters are indicated in the plots.

3.5 DISCUSSION

3.5.1 THE INDIVIDUAL OBJECTS

Here we briefly discuss the results of the individual globules. For maps of them we refer the reader to [Launhardt et al. \(2013\)](#) and to section 2.A of this thesis. The core sizes, masses, and the bolometric luminosities given here are also taken from this paper. The densities and masses given have all been calculated for OH5a dust. Since the results of the temperature structure are very similar for all dust models except of Ormel4d which generally leads to shallower profiles, we call these models for simplicity in the following "steep dust models".

CB 4 is slightly elongated and very isolated. It has a very low density tail towards the north-east and maybe an already dispersed tail towards the east. This globule has the lowest density and warmest core in the EPoS sample. Its energy balance suggests it is transient ([Lippok et al. 2013](#)). It contains a single starless core in its center. We derive the radial profiles of CB 4 without masking any certain region. The core has a central density of $n_0 = 2.3 \times 10^4 \text{ cm}^{-3}$, a size of $5.2 \times 10^4 \text{ AU}$, a mass of $M_{\text{H}} = 0.7 M_{\odot}$ and a bolometric luminosity of $L_{\text{bol}} = 0.77 L_{\odot}$. This globule has a good agreement between ray-tracing and radiative transfer results. The best radiative transfer models are found the steep models and $s_{\text{isrf}} = 2$.

CB 17 is a cometary-shaped globule with a long tail with a column density of about 10^{21} cm^{-2} . The starless core is located in the center of the globule. It has a size of $2.1 \times 10^4 \text{ AU}$, $n_0 = 1.1 \times 10^5 \text{ cm}^{-3}$, $M_{\text{H}} = 1.0 M_{\odot}$ and $L_{\text{bol}} = 0.37 L_{\odot}$. A Class I YSO is located within one beam width from the center of the starless core to the west ([Schmalzl et al. submitted](#)). This impairs the modeling and leads to larger systematic deviations than for the other globules as this blend probably leads to an overestimation of the inner temperature of the starless core. We think that this is one reason why the radiative transfer models lead to a steeper temperature profile than what is derived by the ray-tracing technique. In addition, we do not resolve the core, because it is relatively small and has a relatively large distance of 250 pc. This probably leads to a large systematic error. Nevertheless, we currently have no explanation for the low observed envelope temperature. CB 17 has in fact the lowest envelope temperature in the EPoS sample.

CB 26 is an elongated and relatively extended globule that inhabits a starless and a protostellar core at a projected separation of 30,000 AU. The unresolved protostellar core contains a YSO with a massive edge-on accretion disk ([Launhardt et al. 2009](#)). Here we only consider the starless core. It has a size of $2.2 \times 10^4 \text{ AU}$, $n_0 = 8.2 \times 10^4 \text{ cm}^{-3}$, $M_{\text{H}} = 0.6 M_{\odot}$ and $L_{\text{bol}} = 0.30 L_{\odot}$. The radiative transfer models predict steeper profiles than derived by the ray-tracing method. Only the Ormel4d dust model leads to a good agreement which is best for $s_{\text{isrf}} = 1.5$. The other models would agree better for larger values of $A_{\text{K}}(r_{\text{sym}})$ which are, however, in contradiction with the observed NIR extinction. But this might be explained by the asymmetric shape of this globule leading to a higher average extinction than observed along the LOS.

CB 27 has an extended envelope with a diffuse tail extending to the north and is in contrast tightly constrained to the south. It also has a tail towards the west. The core itself is extended in north-south direction. It has a size of 2.6×10^4 AU, $n_0 = 9.2 \times 10^4 \text{ cm}^{-3}$, $M_{\text{H}} = 1.2 M_{\odot}$ and $L_{\text{bol}} = 0.44 L_{\odot}$. The steep dust models lead to slightly too steep temperature profiles derived by radiative transfer models and they fit best for $s_{\text{isrf}} = 3$. The Ormel4d model leads to a better agreement but for $s_{\text{isrf}} = 2$.

B 68 comes closest to a spherical symmetry together with CB 4. To the south-east it, however, also shows a small extension which is discussed in detail in Nielbock et al. (2012). The core has a size of 1.6×10^4 AU, $n_0 = 1.4 \times 10^5 \text{ cm}^{-3}$, $M_{\text{H}} = 0.6 M_{\odot}$ and $L_{\text{bol}} = 0.23 L_{\odot}$. As in the case of CB 4, the radiative transfer models match the temperature profile derived with the ray-tracing technique for $A_{\text{K}}(r_{\text{sym}}) = A_{\text{obs}}(r_{\text{sym}})$. The best agreement is found for $s_{\text{isrf}} = 3$.

CB 244 is an extended globule that appears to lie at the crossing point of filaments. It contains a protostellar and a prestellar core at a separation of 18,000 AU. The prestellar core has a size of 2.3×10^4 AU, $n_0 = 2.9 \times 10^5 \text{ cm}^{-3}$, $M_{\text{H}} = 2.1 M_{\odot}$ and $L_{\text{bol}} = 0.53 L_{\odot}$. The protostellar core has a bolometric luminosity of $1.8 L_{\odot}$. Its emission is more extended than one SPIRE 500 beam and overlaps with the extent of the prestellar core. This makes the definition of the location of the core center somewhat uncertain. However, the agreement between the temperature profiles derived by the ray-tracing method and the radiative transfer models is good and best for Ormel4d dust and $s_{\text{isrf}} = 2.5$.

3.5.2 UNCERTAINTIES

Even in the most simple-structured star-forming regions like Bok globules, the envelopes of the starless cores are not spherically symmetric (Myers et al. 1991; Launhardt et al. 2013; Lippok et al. 2013). Half of the globules in our sample contain a nearby protostar and the starless core is not located in the center of the globules which further complicates modeling their structure. We elude these problems by cutting out pixels manually that clearly deviate from the symmetric structure for these reasons. We also set an outer radius r_{sym} for the comparison of ray-tracing and radiative transfer results where the assumption of symmetry breaks down or where the signal in the continuum maps gets too weak to allow for reliable derivations of the structure. While this procedure is to some extent arbitrary, the radial profiles would barely change by taking into account a few pixels more or less for averaging. Also, the range of reasonable values of r_{sym} is small and hence the inner region of the cores which is taken into account for the model comparison is well defined.

Not only the cloud structure is asymmetric, the same is expected for the ISRF. It could be enhanced towards the direction of massive stars or the galactic plane. In fact, it was found in Launhardt et al. (2013) that most globules have varying outer temperatures of their envelopes. It was, however, in general not possible to connect directions of increased temperatures with

galactic heating sources. Since we expect that enhancements of the ISRF are coupled to increased dust temperatures, we should to first order not introduce systematic errors into the analysis by radial averaging.

Uncertainties in the distance of the globules lead to an increased uncertainty of the normalization of the density profile but not to increased uncertainties of the temperature profile derived by the ray-tracing technique (apart from smoothing of the profile because of a limited resolution). In the radiative transfer modeling the temperature structure is to first order dependent on the column density. Thus the distance uncertainty does not significantly affect the results of the radiative transfer modeling.

3.5.3 STEEPNESS OF THE TEMPERATURE PROFILES

For five out of six globules we find agreement between the temperature structure derived with the ray-tracing technique and radiative transfer models. However, despite being within the uncertainties in most cases, all dust models in this study except of Ormel4d lead to temperature profiles derived from radiative transfer models that are slightly steeper than the corresponding profiles derived with the ray-tracing technique. There are several potential reasons that might be of different relevance for the individual globules and we discuss them in the following.

The Ormel4d dust opacity has been calculated for dust with thin ice-layers and a coagulation time of 10^6 yr at a hydrogen density of 10^5 cm^{-3} . This model presumably overestimates the coagulation in large parts of the globules because the globules are mostly less dense and likely also younger (Lippok et al. 2013 and Chapter 2).

The opacity of the Ormel4d dust model might compensate for a wrong model of the SED of the ISRF. Other models for the ISRF exist but we unfortunately only have the one at hand that we used in this study. We plan to test further models in the near future.

As already stated in the previous Section, an asymmetry of the cores might in some cases lead to a stronger average extinction of the ISRF than observed.

The density and temperature profiles that are calculated by the ray-tracing technique are convolved to the resolution of the SPIRE 500 μm maps of 36.4". The radiative transfer modeling calculates the temperature structure based on the convolved density profile and the resulting temperature profile is not additionally smoothed. Hence, it is probably systematically steeper than the temperature profiles derived with the ray-tracing method.

The starless cores might also have additional internal heating sources that we do not account for, in particular cosmic rays. The results on their impact onto the dust temperature in the literature are inconsistent. Evans et al. (2001) have argued that neither direct nor secondary heating by cosmic rays, nor collisions with the gas can significantly increase the dust temperature in the interior of starless cores. In contrast, Goldsmith (2001) modeled the effect of

cosmic ray heating in starless cores and they found that collisions of the heated gas with dust grains can increase the dust temperature in the core centers by 1 to 2 K.

3.5.4 COMPARISON TO PREVIOUS STUDIES

None of the earlier studies on the temperature structure of globules containing starless cores had such a strong observational constraint on the thermal dust emission from observations as we have thanks to the *Herschel* observations. For instance, the radiative transfer models by Evans et al. (2001) and Shirley et al. (2005) were only constrained by the (sub-)mm emission of starless cores in globules.

To our knowledge, B 68 is the only core of our study of which the dust temperature structure was attempted to be constrained before using radiative transfer modeling. Bianchi et al. (2003) compared SCUBA 850 μm and SIMBA 1.2 mm maps of this globule to the NIR extinction map of Alves et al. (2001) and calculated the dust temperature distribution with a model by Gonçalves et al. (2004). The correlation of the dust emission to the NIR extinction showed a flattening toward large A_K and they showed that models assuming a temperature gradient can describe the data better than models assuming an isothermal cloud. However, their data did not allow to put tight constraints onto the temperature of B 68 but their result is in agreement with our temperature structure. They also found that the spectral emissivity index is at least 2 in the center of this globule which is larger than what is assumed by the dust models used in this study. Bergin et al. (2006) also calculated the dust temperature of this globule using the model of Zucconi et al. (2001). They found a central dust temperature of about 8 K in agreement with this study but the temperature drop is stronger at larger radii than in our model and in return the temperature structure is shallower at high densities. In Nielbock et al. (2012) we used radiative transfer modeling in order to test the hypothesis that the increased FIR emission on the side of the galactic plane of this globule is a result of a stronger ISRF coming from this direction. The modeling result confirmed this assumption, but did, however, not quantitatively constrain the temperature distribution.

3.6 CONCLUSIONS

With the *Herschel* space observatory it has for the first time become possible to resolve starless cores in the FIR and to sample the peak of the SED of the thermal dust radiation with high sensitivity. This allows to break the density-temperature degeneracy in the interpretation of the continuum emission that had been inevitable before the *Herschel* era. In Nielbock et al. (2012) we presented a ray-tracing technique that allows to simultaneously derive a dust temperature and density structure from the FIR and (sub-)mm emission of starless cores taking into account a thermal gradient in the cores towards the center. We estimated the systematic uncertainties

in the derived dust temperatures to be ± 1 K. This precise temperature estimation strongly decreases the uncertainties in the derived corresponding density structure. While we so far had only used one dust model, we compare the ray-tracing results of seven different dust models in this paper and find that the derived dust temperature is very similar for the considered dust models. In contrast, the dust densities vary by up to an order of magnitude. We further test, if the ray-tracing results are in agreement with radiative transfer models of the thermal equilibrium and find a very good agreement for five out of six studied objects. However, we find that the strength of the interstellar radiation field needs to be increased by a factor of 2-3 in all cases. The results for six dust models that assume uncoagulated or mildly coagulated dust grains with and without ice-layers are very similar. Only one dust model (Ormel4d) which assumes strong coagulation leads to systematically flatter temperature profiles. These flatter profiles are for three globules in better agreement with the ray-tracing results than the profiles derived for the other dust models. The strong coagulation assumed by the Ormel4d model seems unlikely in the cores and we discussed other potential reasons why the temperature structure derived with radiative transfer models appears to be steeper than profiles of the ray-tracing method. In a next step we will test the effect of assuming other models of the ISRF. But it seems likely that in order to distinguish between the scenarios, a three-dimensional radiative transfer forward-modeling will be required that also takes into account a potential change of the dust opacities within the cores.

COMPARISON OF DUST AND GAS TEMPERATURES IN STARLESS CORES

4.1 INTRODUCTION

The work in this thesis is based on *Herschel* continuum observations of the thermal dust emission of starless cores and the derivation of the dust density and temperature thereof. The dust temperature is an important property: without knowledge of the dust temperature the derivation of densities from the dust emission would be highly uncertain. Furthermore, the dust temperature influences the grain properties and the surface chemistry. However, about 99% of the mass in starless cores exists in the gas phase. In order to estimate the thermal and kinetic energies in the cores accurately, it is hence necessary to know the gas temperature. Yet, gas and dust temperatures are expected to be coupled through collisions at hydrogen densities above $\sim 3 \times 10^4 \text{ cm}^{-3}$ (e.g., Galli et al. 2002). Below this density, the coupling is less efficient and the gas and dust temperatures are expected to deviate from each other.

In the center of starless cores the gas is heated only by cosmic rays. Since the main coolants like CO are depleted from the gas phase and the emission of many transitions becomes optically thick (see Chapter 2), cooling of the gas occurs only to a minor extent by molecular emission and predominantly by collisions with the dust grains. At lower densities, cooling of the gas from molecular line emission becomes more efficient and the gas-dust coupling becomes weaker. The gas temperature is thus expected to drop below the dust temperature (e.g., Bergin et al. 2006). Only in the outermost parts of the clouds (at $A_V < 2 \text{ mag}$) photo-electric heating of the gas from the external UV-field becomes so strong that the gas temperature should increase rapidly and rise above the dust temperature. In fact, we found indications for a decoupling of dust and gas temperatures from chemical modeling of the starless cores studied in Chapter 2.

In this Chapter, we aim at measuring the gas temperature and comparing it to the dust temperature, focusing in particular on the conditions in the core centers and out to the radii where gas and dust temperatures are expected to decouple. The gas temperature in cold clouds is usually

inferred from the excitation of the rotational states of some molecular tracers. At low densities CO can be used for this purpose because it is abundant and easily excited (Evans 1999). However, the derivation of the kinetic temperature from CO observations requires sophisticated modeling of the molecular distribution and excitation. At hydrogen densities above 10^4 cm^{-3} , CO freezes out (see Chapter 2) and is thus useless as tracer of the central gas temperature.

The best suited and well established gas temperature probe at $n_{\text{H}} > 10^4 \text{ cm}^{-3}$ is ammonia (NH_3). This molecule is known to barely deplete in the core centers (e.g., Tafalla et al. 2002) and to exist only at hydrogen densities above 10^4 cm^{-3} . It is a symmetric top molecule and the inversion lines of the (J,K)=(1,1) and (2,2) states are known to be excellent tracers of the gas temperature (Walmsley & Ungerechts 1983; Danby et al. 1988; Maret et al. 2009; Juvela et al. 2012). We have, therefore, observed three globules containing starless cores in the NH_3 (1,1) and (2,2) inversion transitions and derived the gas temperature in the cores from these observations.

This Chapter is outlined as follows. In Section 4.2, we describe the observations and the data reduction. The resulting spectral cubes are presented and analyzed in Section 4.3. In Section 4.4, we derive the gas temperature structure of the cores and compare it to the dust temperature in Section 4.5. We discuss the results in Section 4.6 and summarize our findings in Section 4.7.

4.2 OBSERVATIONS

The observations of the ammonia (J,K)=(1,1) and (2,2) inversion lines at 23.7 GHz have been performed at the *Greenbank Telescope* (GBT) in Charlottesville, West Virginia, USA between February and April of 2013. A "Dynamic Scheduling System" is employed at the GBT that schedules observations only a few days before the observing sessions. This ensured excellent weather conditions during the course of the observations. These are needed for observations around 22 GHz because water vapor in the atmosphere strongly absorbs at these wavelengths. We used the K-band focal plane array (KFPA) and obtained On-The-Fly maps with inband frequency-switching. The channel width was set to 3.05 kHz corresponding to 0.039 km/s. With a bandwidth of 50 MHz we could observe both transitions simultaneously. This ensures a correct relative calibration of the (1,1) and (2,2) emission which makes the subsequent temperature derivation from the ratio of the intensities of both lines reliable. At the beginning of each observing session we calibrated the flux of the seven individual beams of the KFPA using calibrators listed in Ott et al. (1994). For the objects CB 17 and CB 27, we used the flux calibrator 3C147 and for B 68 the calibrator NGC7027. We generated a spectral cube per observing session with the GBT pipeline taking into account the respective beam scaling factors. Then we converted the cubes into the Gildas data format and used CLASS¹ for a final

¹<http://www.iram.fr/IRAMFR/GILDAS>

baseline subtraction and the combination of several cubes for those objects which had been observed in more than one session. The half-power beam-width of the observations is $31''$ and the rms noise per channel is 33 mK for CB 17, 40 mK for CB 27, and 85 mK for B 68 which has been covered less than the other globules.

4.3 RESULTS

4.3.1 INTEGRATED INTENSITY MAPS

In Figures 4.1-4.3 we present emission maps of the NH_3 (1,1) and NH_3 (2,2) transitions of the globules CB 17, CB 27, and B 68. They are supplemented by emission maps of the ($J=1-0$) transition of the chemically related molecule N_2H^+ (Aikawa et al. 2005) and maps of the $350\ \mu\text{m}$ continuum emission as observed with the SPIRE photometer on board the *Herschel* space observatory.

In CB 17 and CB 27, the NH_3 (1,1) emission is more extended than the N_2H^+ emission while the opposite is the case for B 68. This is very likely caused by the sensitivity of the respective observations: as can be seen in Table 4.1, the noise level of the N_2H^+ map of B 68 is much lower than for the other globules and at the same time the noise level of the ammonia observations is higher for B 68 than for the other globules. Thus, very small abundances of ammonia probably exist also at lower hydrogen densities but below the detection limit and it is not possible to directly conclude from the observations whether NH_3 or N_2H^+ molecules are more extended.

The blue dashed lines in Figures 4.1-4.3 indicate the hydrogen mid-plane density as derived with the ray-tracing technique for OH5a dust. The ammonia (1,1) transition is detected at hydrogen densities $n_{\text{H}} \gtrsim 10^4\ \text{cm}^{-3}$. The NH_3 (2,2) line was detected at hydrogen densities $n_{\text{H}} \gtrsim 5 \times 10^4\ \text{cm}^{-3}$.

The similarity in the shapes of the optically thin continuum emission and the NH_3 (1,1) emission indicates that ammonia traces the innermost parts of the starless cores. While the N_2H^+ emission flattens towards the center of the cores in CB 27 and B 68, this is not observed for the NH_3 (1,1) emission. This is an indication that depletion of NH_3 in the core centers is not as severe as of N_2H^+ . This was also found by Tafalla et al. (2002).

We found in Chapter 2 that the cores of CB 17 and CB 27 have approximately the same mass and very similar density and temperature structures. The NH_3 (1,1) emission of the core center in CB 27 is in contrast 20% stronger than in CB 17. At the same time the N_2H^+ emission is 30% weaker. The ratio between the NH_3 (2,2) and the NH_3 (1,1) transition is smaller by 35% in CB 27 compared to CB 17. While we have derived very similar properties on the physical structure from the continuum emission, this indicates that the core of CB 27 might be

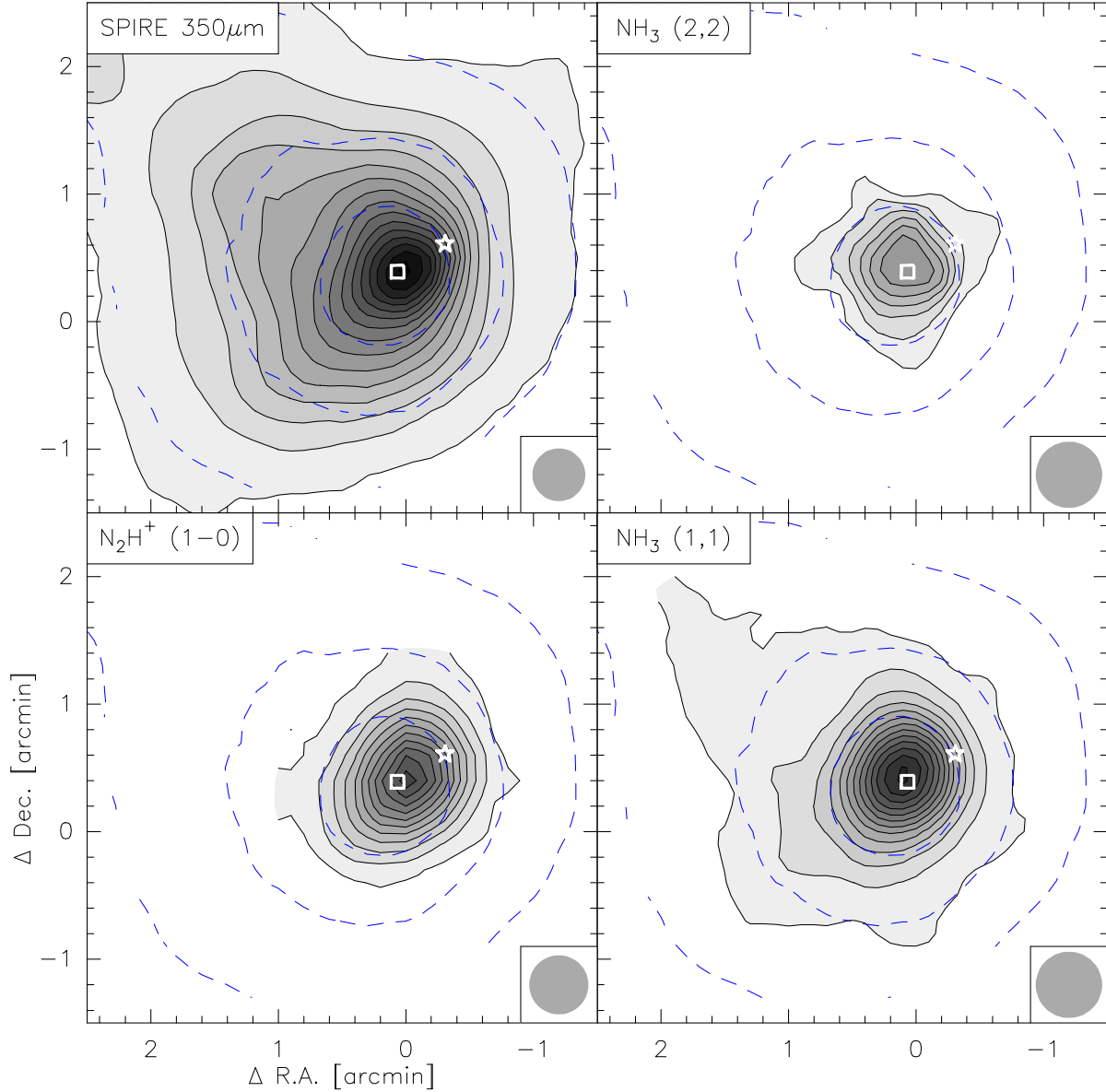


Figure 4.1: CB17. Maps of the continuum emission at 350 μm observed with SPIRE and the integrated emission (over all hyperfine lines) of the NH_3 (1,1), NH_3 (2,2), and N_2H^+ (1-0) transitions. The squared marker indicates the center of the starless core and the asterisk marks the position of the YSO. The values of the first contour and the steps of the next contours in the continuum map is 0.2 Jy/beam with a beam size of 24.9". The first contour of the NH_3 (1,1) map is at 0.12 K.km/s, the next contours have steps of 0.3 K.km/s. The values of the first contour and the steps of the NH_3 (2,2) map is 0.02 K.km/s. The first contour of the N_2H^+ (1-0) map is at 0.2 K.km/s, the next contours have steps of 0.4 K.km/s. The blue dashed lines correspond to mid-plane hydrogen densities n_{H} derived with the ray-tracing technique (see Chapters 2 and 3) of 10^3cm^{-3} , 10^4cm^{-3} , and $5 \times 10^4\text{cm}^{-3}$.

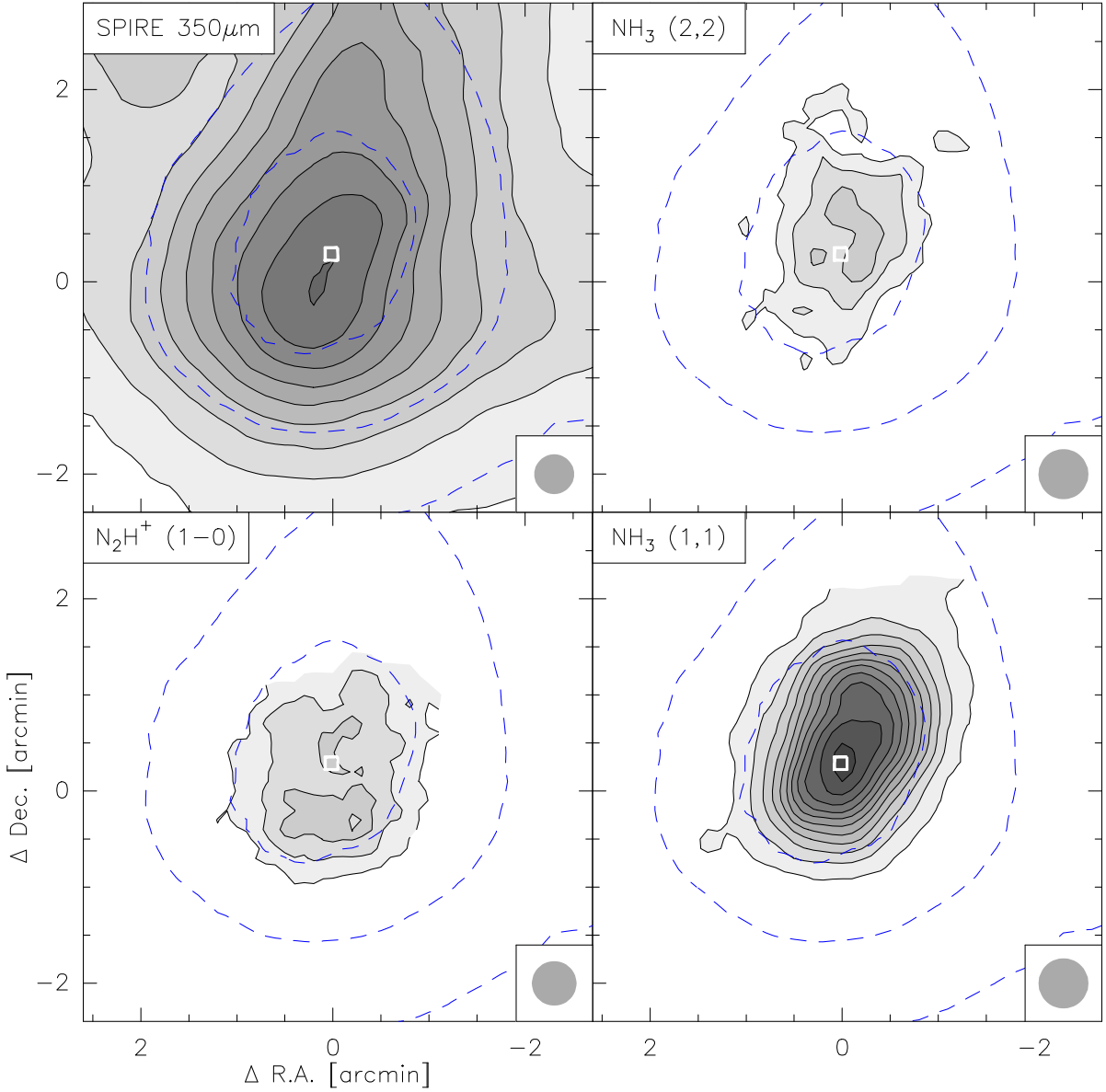


Figure 4.2: CB27. Maps of the dust continuum emission at 350 μm observed with SPIRE and the integrated line emission (over all hyperfine lines) of the NH₃ (1,1), NH₃ (2,2), and N₂H⁺ (1-0) transitions. The squared marker indicates the center of the starless core. For all maps the first contour and the contour interval is the same. The values are 0.2 Jy/beam for the continuum map with a beam size of 24.9'', 0.4 K.km/s for the NH₃ (1,1) map, 0.04 K.km/s for the NH₃ (2,2) map, and 0.75 K.km/s for N₂H⁺ (1-0). The blue dashed lines correspond to n_{H} of 10^3 cm^{-3} , 10^4 cm^{-3} , and $5 \times 10^4 \text{ cm}^{-3}$.

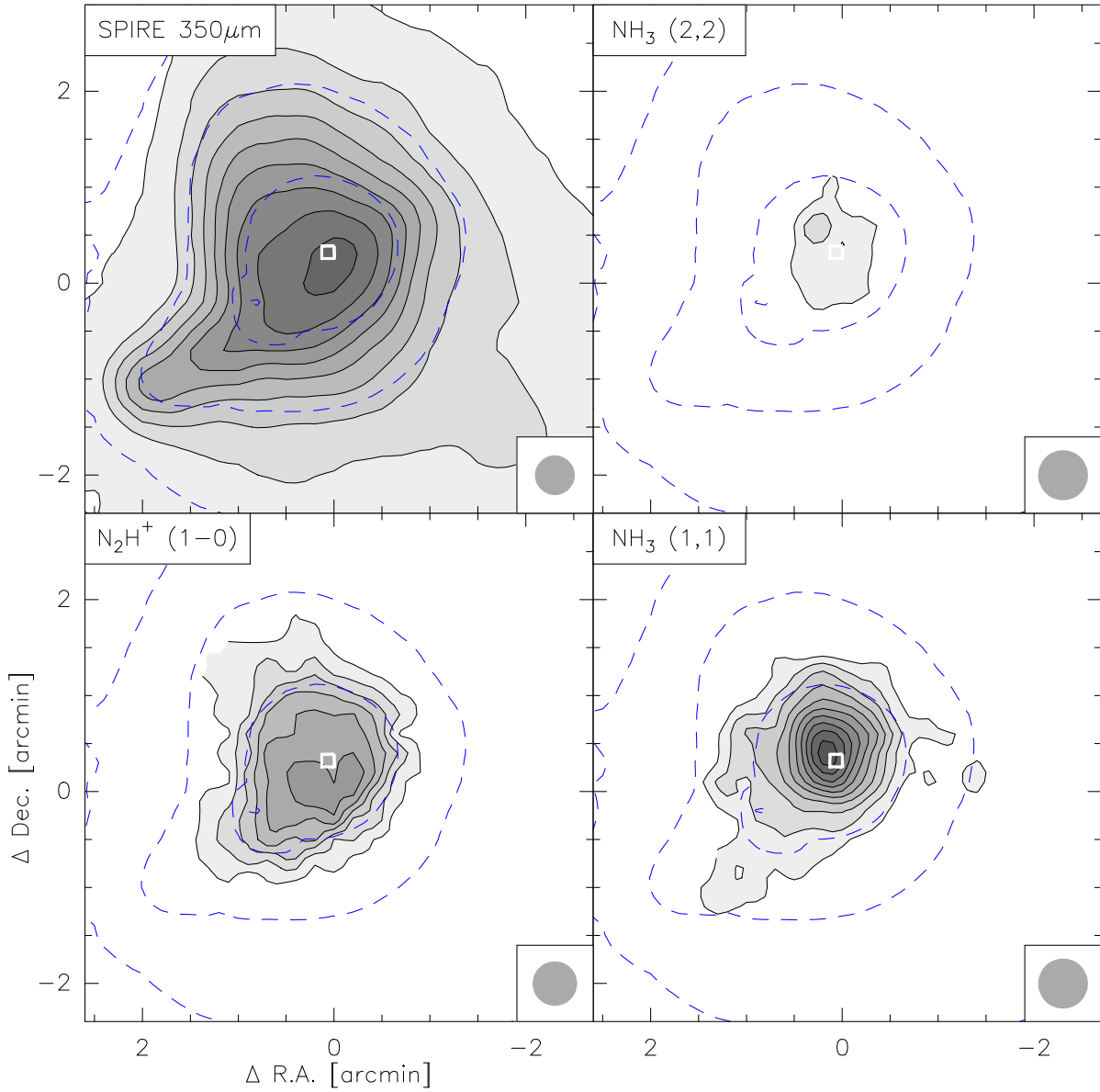


Figure 4.3: B68. Maps of the continuum emission at $350\mu\text{m}$ observed with SPIRE and the integrated emission (over all hyperfine lines) of the NH_3 (1,1), NH_3 (2,2), and N_2H^+ (1-0) transitions. The squared marker indicates the center of the starless core. For all maps the first contour and the contour interval is the same. The values are 0.2 Jy/beam for the continuum map with a beam size of $24.9''$, 0.3 K.km/s for the NH_3 (1,1) map, 0.05 K.km/s for the NH_3 (2,2) map, and 0.25 K.km/s for N_2H^+ (1-0). The blue dashed lines correspond to n_{H} of 10^3 cm^{-3} , 10^4 cm^{-3} , and $5 \times 10^4\text{ cm}^{-3}$.

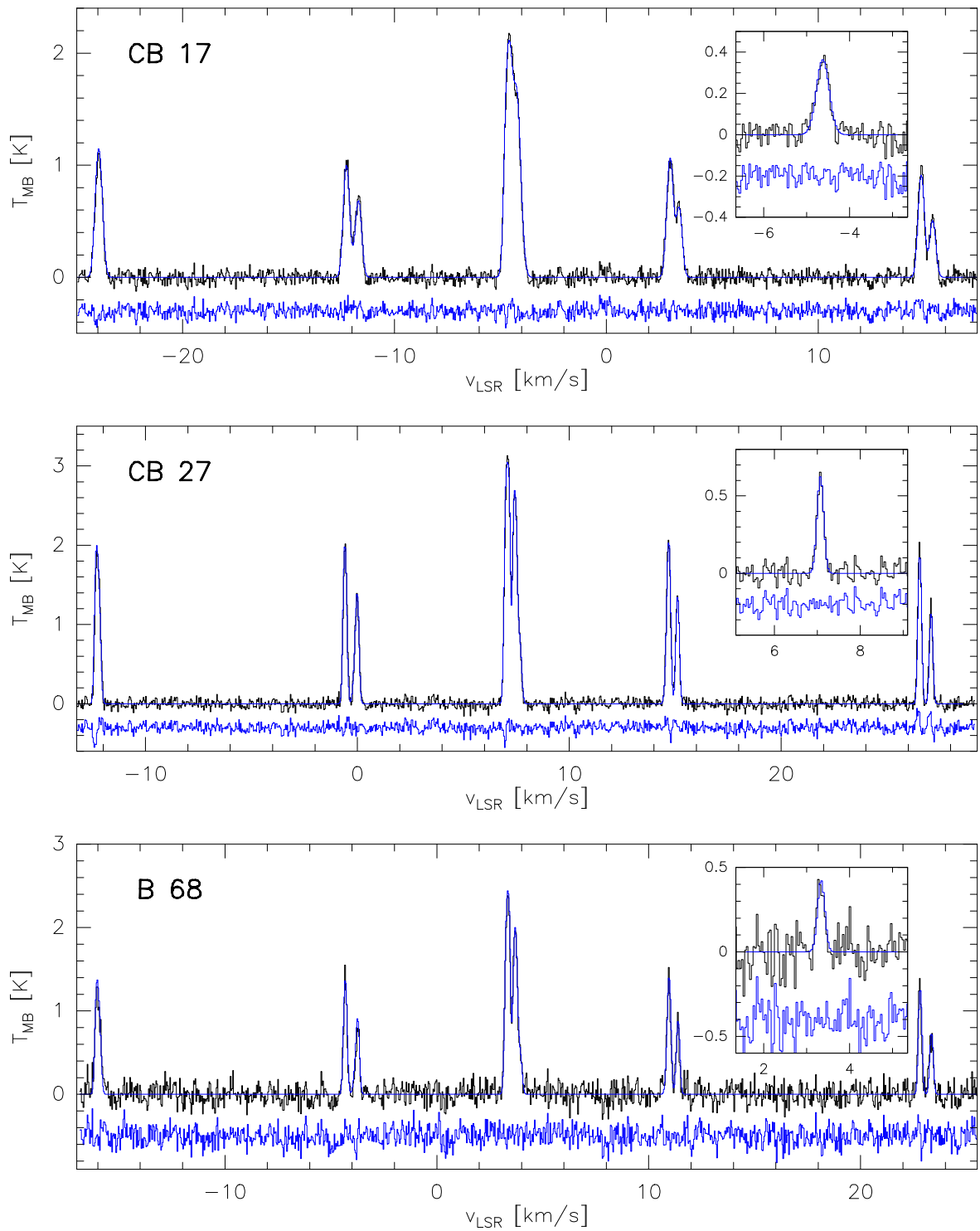


Figure 4.4: Spectra and fits of the NH_3 (1,1) transition at the center of the starless cores of CB 17, CB 27, and B 68. The inset shows the main line of the NH_3 (2,2) transition. Its hyperfine lines are not detected. The observed spectra are plotted black. The fits and their residua are blue colored.

denser and colder than that of CB 17.

Finally, we note that the YSO of CB 17 is not detected in the ammonia maps which indicates that it is not embedded in a dense core as already concluded from the dust emission maps in Launhardt et al. (2013).

4.3.2 GAS KINEMATICS

We determined the line-of-sight velocity component v_{LSR} as well as its width Δv of the ammonia molecules from fits to the hyperfine structure of the $\text{NH}_3(1,1)$ emission. For this task, we used the "nh3" hyperfine fitting routine provided with CLASS. Maps of v_{LSR} and Δv of all globules are shown in Fig. 4.5.

In CB 27 and B 68 a monotonic gradient of v_{LSR} is observed which can to first order be interpreted as solid-body rotation of the entire core. Both globules are roughly elliptically shaped but while the rotational axis of CB 27 is in the direction of the semi-minor-axis (prolate spheroid), it is in the direction of the semi-major axis in B 68 (oblate spheroid). The line-width of both core centers is very similar and increases toward larger radii. The values for the core centers are listed in Table 4.1. The central spectra are also shown in Figure 4.5.

CB 17 shows a gradient which is orthogonal to the north-east direction of the cometary tail. This direction was interpreted as the orientation of the rotational axis of the starless core in Schmalzl et al. (submitted). Towards the south-west of the center of the starless core, the velocity gradient turns around. CB 17 does not show the lowest line-widths in the core center. Instead, the width has a butterfly-like structure with two local minima in the north-west and south-east of the core center and an increase width along the rotational axis. Schmalzl et al. (submitted) also found this from observations of N_2H^+ and discussed several scenarios leading to these observations. The most likely scenario is that the rotating starless core is moving in the plane-of-the-sky from the north-east to the south-west through the more extended envelope. It was found in Chen et al. (2012) from interferometric observations that the starless core of CB 17 inhabits a small continuum source. Interferometric CO observations reveal that the YSO in CB 17 drives an outflow in the direction of this source and that the source itself might also drive an outflow. In either case, this further complicates the interpretation of the line-widths.

Table 4.1: Spectral line parameters at the center of the starless cores

Source	Line	$v_{\text{lsr}}^{(a,b)}$ [km/s]	$T_{\text{MB}}^{\text{peak}(b,c)}$ [K]	$T_{\text{MB}}^{\text{RMS}(d)}$ [mK]	$\Delta v_{\text{FWHM}}^{(a,b)}$ [m/s]	$v_{\text{therm}}^{(e)}$ [m/s]	$v_{\text{non-therm}}$ [m/s]	$I_{\text{line}}^{(f)}$ [K.km/s]
CB 17	NH ₃ (1,1)	-4.59	2.15 ± 0.03	33	329 ± 3	177 ± 9	277 ± 9	3.79 ± 0.04
	NH ₃ (2,2)	-4.62	0.37 ± 0.03	33	352 ± 24	177 ± 9	304 ± 33	0.14 ± 0.01
	N ₂ H ⁺ (1-0)	-4.63	1.5 ± 0.02	190	325 ± 2	135 ± 7	296 ± 5	3.0 ± 0.06
CB 27	NH ₃ (1,1)	+7.09	3.13 ± 0.04	40	179 ± 1	168 ± 9	62 ± 27	4.55 ± 0.05
	NH ₃ (2,2)	+7.09	0.59 ± 0.04	40	181 ± 11	168 ± 9	67 ± 52	0.11 ± 0.01
	N ₂ H ⁺ (1-0)	+7.10	2.10 ± 0.08	80	187 ± 4	129 ± 6	135 ± 11	2.15 ± 0.07
B 68	NH ₃ (1,1)	+3.35	2.36 ± 0.07	85	184 ± 4	166 ± 9	79 ± 28	3.10 ± 0.1
	NH ₃ (2,2)	+3.32	0.32 ± 0.04	85	189 ± 14	166 ± 9	90 ± 46	0.065 ± 0.03
	N ₂ H ⁺ (1-0)	+3.35	0.88 ± 0.01	10	249 ± 3	127 ± 6	220 ± 7	1.5 ± 0.04

Notes. ^(a) for the NH₃ (1,1) and N₂H⁺ (1-0) transitions determined from fits to the hyperfine structure, ^(b) for the NH₃ (2,2) transition determined from a Gaussian fit to the main line, ^(c) for the NH₃ (1,1) and N₂H⁺ (1-0) transitions we take the peak value of the spectrum, ^(d) root-mean-square noise of the spectra ^(e) assuming the gas temperature of the core centers derived from the ammonia observations (see Table 4.2), ^(f) determined by integrating over all hyperfine components of the spectra.

4.4 COLUMN DENSITY AND KINETIC TEMPERATURE DERIVED FROM AMMONIA

4.4.1 METHOD

Ammonia is a tracer of the dense gas in starless cores. It forms out of N_2H^+ (Aikawa et al. 2005) and is a late depleter. In fact, it even appears to be enhanced where N_2H^+ is already depleted (Tafalla et al. 2002). It therefore traces the center of the cores. Ammonia has quantum mechanical properties that make it favorable as tracer of the gas temperature. It is a symmetric top molecule and its $(J = K)$ levels are metastable. Their population is, therefore, mainly defined by collisions and thus by the rotational temperature of the ammonia molecules. The critical density of the (1,1) and (2,2) states is about $2 \times 10^3 \text{ cm}^{-3}$ (Evans 1999) so that they are in local thermal equilibrium at the conditions in the dense starless cores. Each (J, K) state is split up into two sub-levels (inversion doubling) corresponding to two different orientations of the nitrogen nucleus with respect to the plane made up by the hydrogen atoms. The inversion doublet is further split up into hyperfine states. The emission from the inversion transitions thus has a hyperfine structure. Since the hyperfine lines are differently excited, their optical depth is different. The total optical depth and thus the level populations of the $(J = K)$ states can therefore be determined from fits to the hyperfine structure of the inversion transitions. By measuring the population of two states, the rotational temperature T_{rot} can be determined. T_{rot} is in turn well related to the kinetic temperature T_{kin} . In the following, I describe the procedure for the derivation of the gas temperature from the ammonia observations.

For the derivation of the kinetic temperature of NH_3 we follow in principle the "standard analysis" which results in line-of-sight averaged and ammonia density weighted kinetic temperatures. In a first step, the rotational temperature T_{rot} is derived from the spectra of the $(J, K) = (1, 1)$ and $(2, 2)$ transitions (e.g., Bachiller et al. 1987). It is related to the relative rotational level populations by

$$\frac{N_{\text{u}}}{N_{\text{d}}} = \frac{g_{\text{u}}}{g_{\text{d}}} e^{-\Delta E/k_{\text{b}}T_{\text{rot}}}, \quad (4.1)$$

where k_{b} is the Boltzmann constant, $g_{\text{u}, \text{d}}$ are the statistical weights of the upper and lower state and ΔE is the energy difference between the states.

For ammonia it can be calculated from the optical depths of the (1,1) and (2,2) inversion transitions τ_{11} and τ_{22} via (Ho et al. 1979; Hotzel et al. 2002):

$$T_{\text{rot}} = -\frac{41.5}{\ln\left(\frac{9}{20} \frac{\tau_{22}}{\tau_{11}}\right)}. \quad (4.2)$$

We obtain τ_{11} directly from fits to the hyperfine structure of the NH_3 (1,1) transition. This

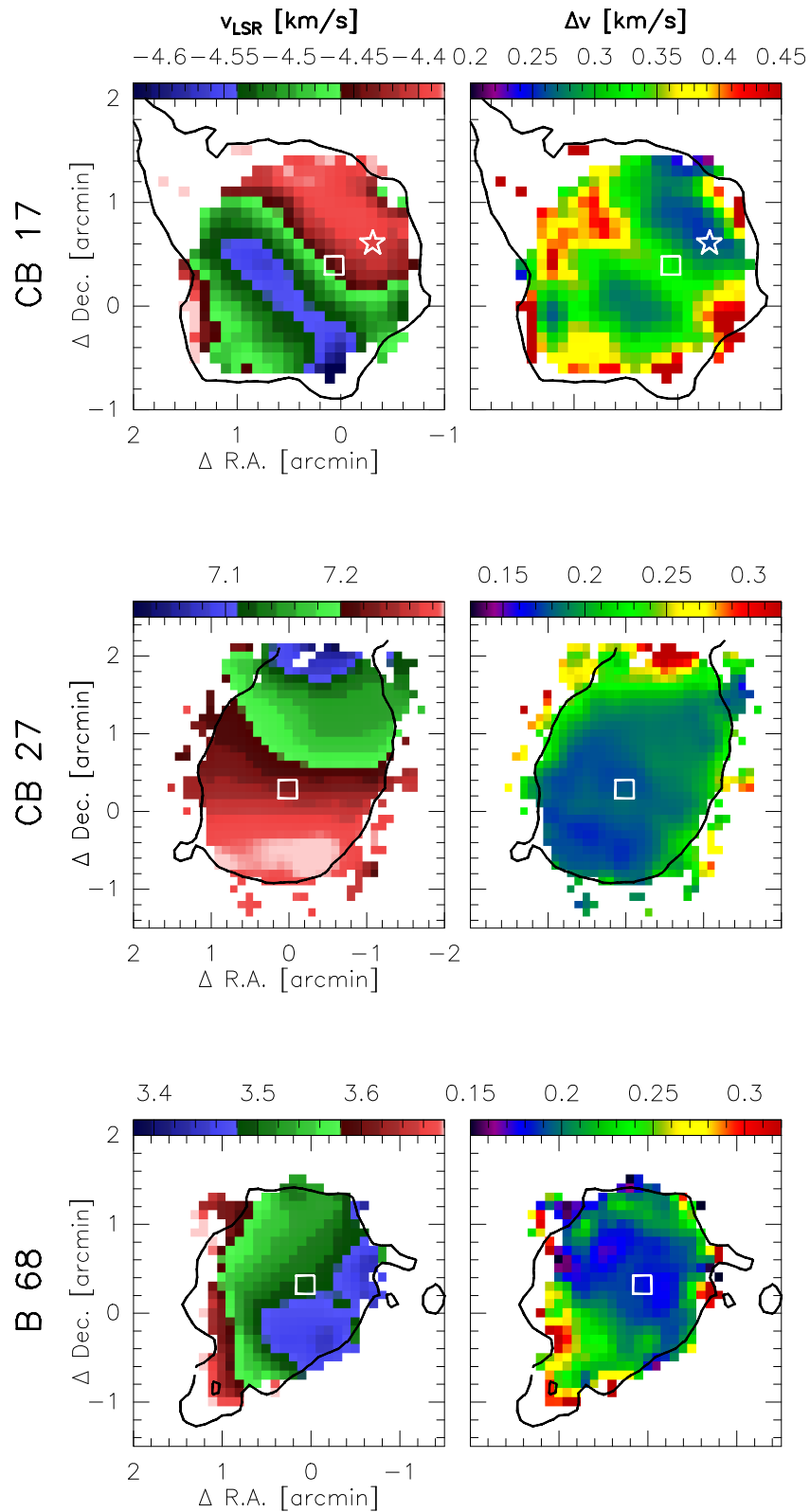


Figure 4.5: Line-of-sight velocity component of the globules obtained from fits to the hyperfine structure of the NH_3 (1,1) transition. The contours are the same as the outer contours in the emission maps of NH_3 (1,1) in Figures 4.1-4.3. The white squares indicate the centers of the starless cores. The asterisk marks the position of the YSO in CB 17.

fit also reveals the excitation temperature T_{ex} of the (1,1) transition. The (2,2) transition is so weak that the hyperfine structure is not detected and only the main line can be used for the analysis. Therefore, the excitation temperature of this transition cannot be derived directly from the spectra and it is usually assumed that the (2,2) transition has the same excitation temperature as the (1,1) transition. Then, τ_{22} can be derived from the "detection equation":

$$T_{\text{MB}}^{22} = T_0 \left(f(T_{\text{ex}}) - f(T_{\text{bg}}) \right) (1 - e^{-\tau_{22}}) \quad (4.3)$$

where $T_0 = h\nu_{22}/k_{\text{b}}$ and $\nu_{22} = 23.723$ GHz which is the frequency of the (2,2) transition, $T_{\text{bg}} = 2.73$ K, T_{MB}^{22} being the peak main beam temperature of the Gaussian-shaped line, and

$$f(T) \equiv \frac{1}{e^{T_0/T} - 1}. \quad (4.4)$$

We use an empirical formula for the conversion of T_{rot} to T_{kin} that was derived by Tafalla et al. (2004). They also showed that below 20 K, this formula is exact within 5%:

$$T_{\text{kin}} = \frac{T_{\text{rot}}}{1 - \frac{T_{\text{rot}}}{42} \ln(1 + 1.1 \exp(-16/T_{\text{rot}}))} \quad (4.5)$$

Following Rosolowsky et al. (2008), we derive the column density of the (1,1) state by:

$$N(1, 1) = \frac{\sqrt{2\pi} 8\pi\nu_{11}^3}{c^3} \frac{g_1}{g_2} \frac{\Delta\nu\tau_{11}}{A(1, 1)} \left(1 - \exp\left(-\frac{h\nu_{11}}{k_{\text{b}}T_{\text{ex}}}\right) \right)^{-1} \quad (4.6)$$

where the statistical weights g_1 and g_2 are equal and $A(1, 1) = 1.68 \times 10^{-7} \text{s}^{-1}$ (Pickett et al. 1998). The total ammonia column density is then given by

$$N_{\text{NH}_3} = Z N(1, 1) \quad (4.7)$$

with Z being the partition function of the metastable states:

$$Z = \sum_J (2J + 1) S(J) \exp\left(\frac{-h(BJ(J + 1) + (C - B)J^2)}{k_{\text{b}}T_{\text{rot}}}\right). \quad (4.8)$$

$S(J)$ takes into account the statistical weights of the ortho- over the para-NH₃ states. $S(J) = 2$ for $J = 3, 6, 9, \dots$ and 1 otherwise. According to Pickett et al. (1998), the rotational constants B and C have the values 298117 MHz and 186736 MHz, respectively.

4.4.2 UNCERTAINTIES

There are several sources of uncertainties in this analysis. First, the absolute flux of the calibrators has an uncertainty of below 10%. Second, the flux calibration that we carried out at the beginning of each session also introduces uncertainties. We estimate that both contributions lead to an uncertainty in the absolute flux of 10% of our observations as recommended at the GBT. The flux uncertainty only affects the derivation of the column densities, but not of the kinetic temperature, because to first order, only the ratio of the intensities of the (1,1) and (2,2) transitions enters T_{kin} and we have observed them simultaneously.

Next, the line fitting introduces uncertainties that are quantified by the fitting routine for each fit and enter both the derivation of the column density as well as of the temperature.

Ho et al. (1979) showed that the largest error of the kinetic temperature is introduced by the assumption that $T_{\text{ex}}(1, 1) = T_{\text{ex}}(2, 2)$. However, Maret et al. (2009) and Juvela et al. (2012) both show using radiative transfer modeling that the derivation of the kinetic temperature from the (1,1) and (2,2) inversion transitions assuming $T_{\text{ex}}(1, 1) = T_{\text{ex}}(2, 2)$ is very reliable. The results are expected to be correct within 0.3 K even at the largest optical depths that are present in the core centers.

An additional error is introduced, if the emissivity structure is not resolved. This is probably the case in CB 17 because this globule has a relatively high distance of 250 pc. However, this uncertainty enters equally the NH_3 (1-1) and (2-2) transitions such that we average the kinetic temperature over the beam. Since the derivation of the dust temperature also has these uncertainties, we do not introduce additional uncertainties in the comparison of both temperature profiles.

4.4.3 MAPS OF THE AMMONIA COLUMN DENSITY AND KINETIC TEMPERATURE

Maps of the kinetic temperature T_{kin} and the column density of the (1,1) state are plotted in Figs. 4.6-4.8. The maps of the temperature are less extended than those of the (1,1) column densities, because the temperature derivation requires reliable fits of the (2,2) inversion spectra. This emission is very weak and only detected in the regions of the strongest (1,1) emission. The temperature maps of CB 17 and B 68 are about two beam widths across. The temperature map of CB 27 is somewhat larger. The variations of the temperature in the maps are largely within the uncertainties, but a tentative trend towards higher temperatures off the core center is visible.

We plot the column densities of the NH_3 (1,1) state and not the total column density of ammonia because this quantity can only be calculated with the knowledge of the partition function Z (Eq. 4.7 and 4.8) which requires that the rotational temperature is known. However, we find that N_{tot} is only 5% larger than $N(1, 1)$ in those regions where Z is known. The central column

Table 4.2: Comparison of densities and temperatures at the core centers

Object	T_{kin}^a [K]	T_d^b [K]	$N(\text{NH}_3)^b$ [10^{14} cm^{-2}]	N_{H}^b [10^{22} cm^{-2}]	n_{H}^b [10^4 cm^{-3}]
CB 17	11.7 ± 1.2	11.0_{-1}^{+2}	1.3 ± 0.3	2.9 ± 0.7	11.2 ± 2.8
CB 27	10.5 ± 1.2	10.8_{-1}^{+2}	1.5 ± 0.4	2.7 ± 0.7	9.2 ± 2.3
B 68	10.2 ± 1.1	7.7_{-1}^{+2}	1.0 ± 0.2	2.6 ± 0.7	13.9 ± 3.5

Notes. ^(a) LOS and mass averaged kinetic temperature of ammonia derived according to Sect. 4.4.1.

^(b) Derived with the raytracing technique for OH5a dust.

density N_{tot} of all cores is about 10^{14} cm^{-2} and the central ratio of $N_{\text{tot}}/N_{\text{H}}$ is the same for all cores within the uncertainties (see Tab. 4.2). We also plot contours of the mid-plane hydrogen density n_{H} derived with the ray-tracing technique for OH5a dust in Figs. 4.6-4.8 and find that they have a very similar shape as the NH_3 (1,1) column density distribution for $n_{\text{H}} > 10^4 \text{ cm}^{-3}$. This confirms that ammonia traces the densest regions of the cores. One exception is found for B 68: a high density region with $n_{\text{H}} > 5 \times 10^4 \text{ cm}^{-3}$ in the south-east of the core center has a relatively low ammonia column density. Interestingly, in this region the C^{18}O emission is increased (see Fig. 2.15). Hence, the globule might in this region be chemically not as evolved as in the core center.

4.5 COMPARISON OF GAS AND DUST TEMPERATURES

In order to obtain a better signal-to-noise ratio of the kinetic temperature of ammonia and an easy comparison to the dust temperature, we obtained radial temperature profiles. They are plotted in Fig. 4.9 against the radius of the starless core and in Fig. 4.10 against the corresponding mid-plane hydrogen density as derived with the ray-tracing technique assuming OH5a dust. The uncertainties have been calculated by taking into account the contributions discussed in Sect. 4.4.2. In all cores, the smallest kinetic temperature is found towards the core centers (see Table 4.2 for values) and it slowly increases outwards by about 2 K.

We also plot the dust temperature profiles in Fig. 4.9 and Fig. 4.10. They have been derived with the ray-tracing technique using the OH5a dust opacity model. Within the uncertainties, dust and gas temperatures are the same in the core centers of CB 17 and CB 27. The central gas temperature of B 68 and CB 27 are similar, but the dust temperature of B 68 is by 2.5 K lower. Towards larger radii the difference of the gas and dust temperatures in B 68 decreases by about 1 K.

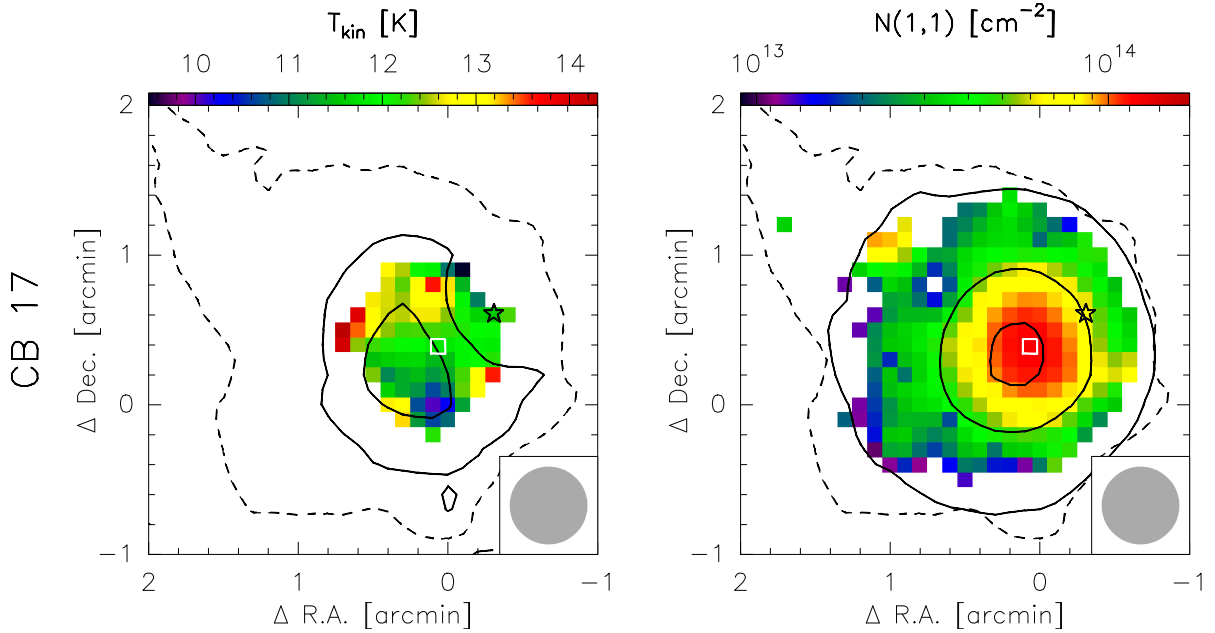


Figure 4.6: (*Left:*) Map of the kinetic temperature of CB 17 derived from the NH_3 (1,1) and (2,2) inversion lines. The solid contours depict dust temperatures and correspond to 11.5 K and 12.5 K. (*Right:*) Column densities of the NH_3 (1,1) state. The solid contours represent mid-plane hydrogen densities as derived with the ray-tracing technique of 10^5 cm^{-3} , $5 \times 10^4 \text{ cm}^{-3}$, and 10^4 cm^{-3} . The dashed contours in both plots are the same as the outer contours of the NH_3 (1,1) emission map presented in Fig. 4.1 and indicate the extent of detected NH_3 (1,1) emission.

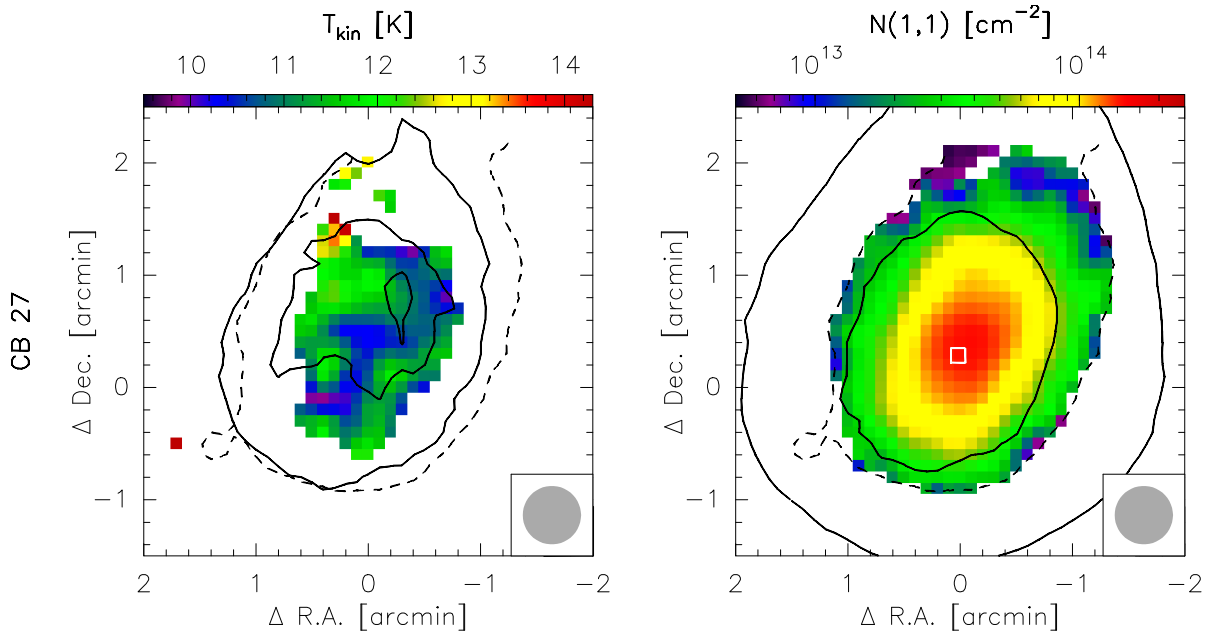


Figure 4.7: (*Left:*) Map of the kinetic temperature of CB 27 derived from the NH_3 (1,1) and (2,2) inversion lines. The solid contours depict dust temperatures and correspond to 11 K and 12 K. (*Right:*) Column densities of the NH_3 (1,1) state. The solid contours represent mid-plane hydrogen densities as derived with the ray-tracing technique of $5 \times 10^4 \text{ cm}^{-3}$ and 10^4 cm^{-3} . The dashed contours in both plots are the same as the outer contours of the NH_3 (1,1) emission map presented in Fig. 4.2 and indicate the extent of detected NH_3 (1,1) emission.

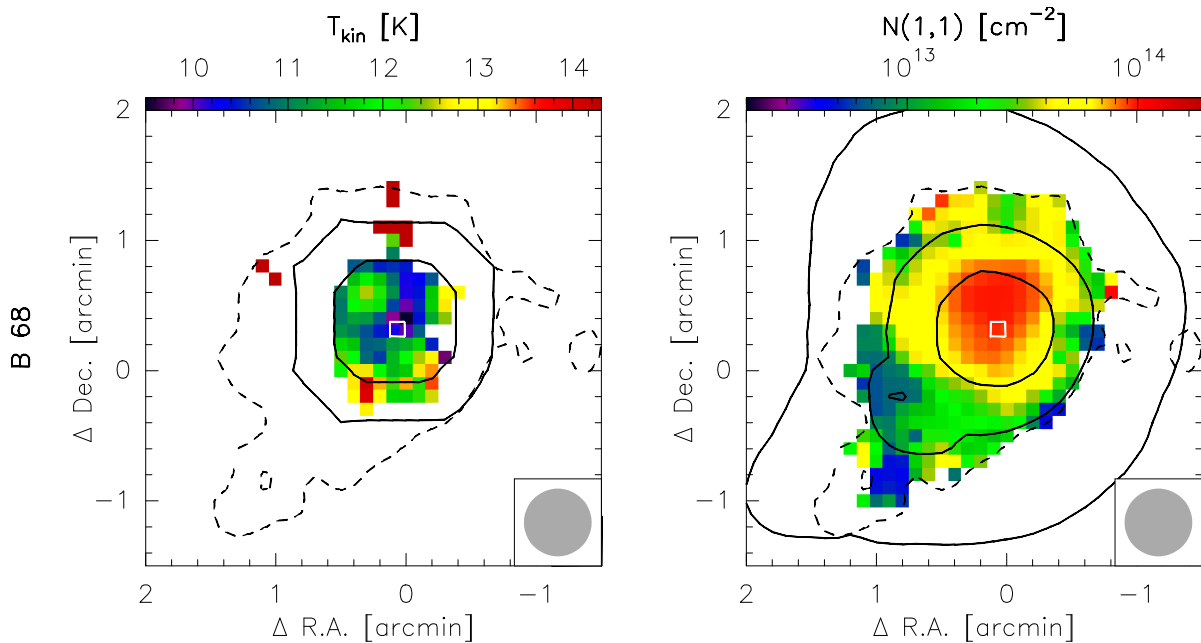


Figure 4.8: (*Left:*) Map of the kinetic temperature of B 68 derived from the NH_3 (1,1) and (2,2) inversion lines. The solid contours depict dust temperatures and correspond to 11 K and 12 K. (*Right:*) Column densities of the NH_3 (1,1) state. The solid contours represent mid-plane hydrogen densities as derived with the ray-tracing technique of $5 \times 10^4 \text{ cm}^{-3}$ and 10^4 cm^{-3} . The dashed contours in both plots are the same as the outer contours of the NH_3 (1,1) emission map presented in Fig. 4.3 and indicate the extent of detected NH_3 (1,1) emission.

4.6 DISCUSSION

The central dust temperature of CB 17 and CB 27 is about 11 K and the gas temperature in the center of these cores is the same within the uncertainties. In contrast, B 68 has a central dust temperature of only 8 K but a gas temperature of 10 K. The gas temperature of B 68 has been measured before using ammonia observations with a single pointing towards the core center by Hotzel et al. (2002). Their measurement of $T_{\text{kin}} = 10 \pm 1.2 \text{ K}$ is well in agreement with our result. Bergin et al. (2006) pointed out that the assumed uncertainty of the measurement by Hotzel et al. (2002) originated mainly from the assumption of $T_{\text{ex}}(1, 1) = T_{\text{ex}}(2, 2)$ of $\pm 20\%$ which is very conservative. The difference between dust and gas temperatures in the core center of B 68 is just within the conservatively estimated uncertainties.

Tafalla et al. (2002) found that the ammonia abundance rises towards the centers of starless cores in contrast to N_2H^+ . Since we found in Chapter 2 that N_2H^+ is strongly depleted in the core center of B 68, we tested what the abundance of ammonia is in the chemical model that we found in Chapter 2 to describe the N_2H^+ (1-0) observations best. The absolute and relative abundance profiles of both species of this model are shown in Fig. 4.11. According to this model, ammonia is also somewhat depleted in the center of B 68, but because of the increase of the total gas density, its absolute abundance is roughly constant within the inner 4,000 AU

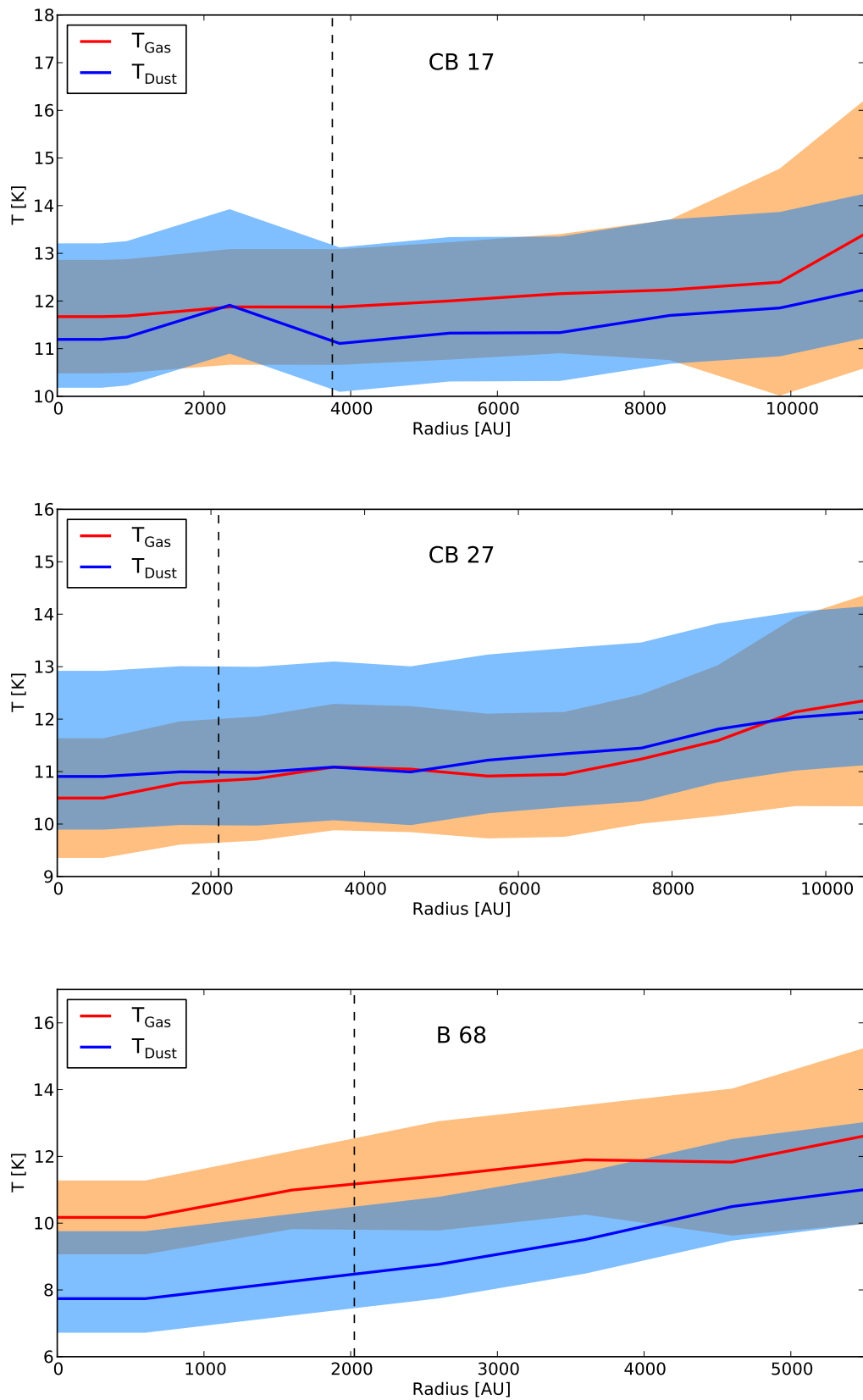


Figure 4.9: Comparison of radially averaged temperature profiles of CB 17 (*top*), CB 27 (*middle*), and B 68 (*bottom*). The temperature is plotted over the radius of the cores. The dust temperature was derived with the ray-tracing technique assuming OH5a dust. The gas temperature is the line-of-sight averaged kinetic temperature of ammonia.

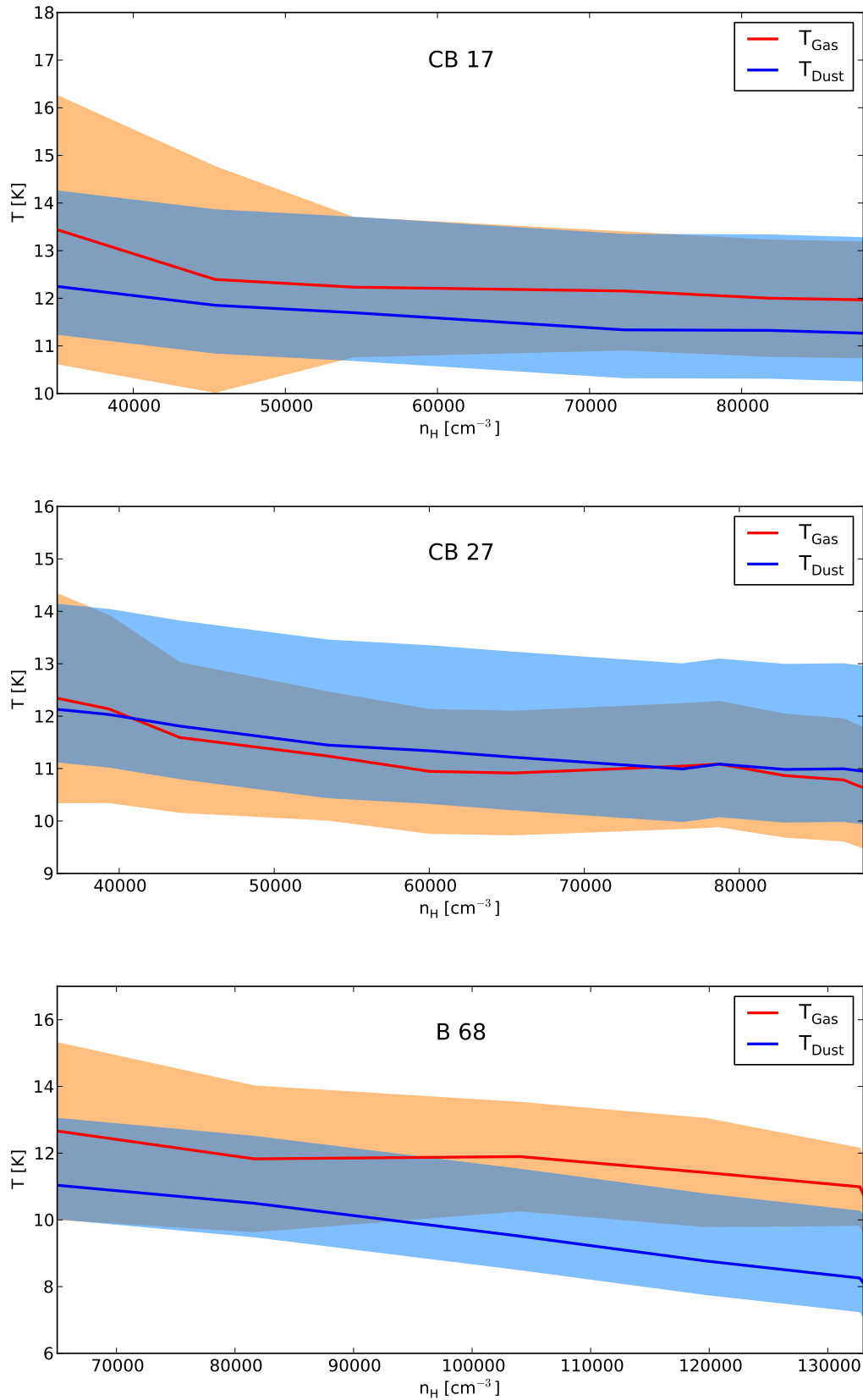


Figure 4.10: Comparison of radially averaged temperature profiles of CB 17 (*top*), CB 27 (*middle*), and B 68 (*bottom*). The temperature is plotted against the corresponding mid-plane hydrogen density. The dust temperature was derived with the ray-tracing technique assuming OH5a dust. The gas temperature is the line-of-sight averaged kinetic temperature of ammonia.

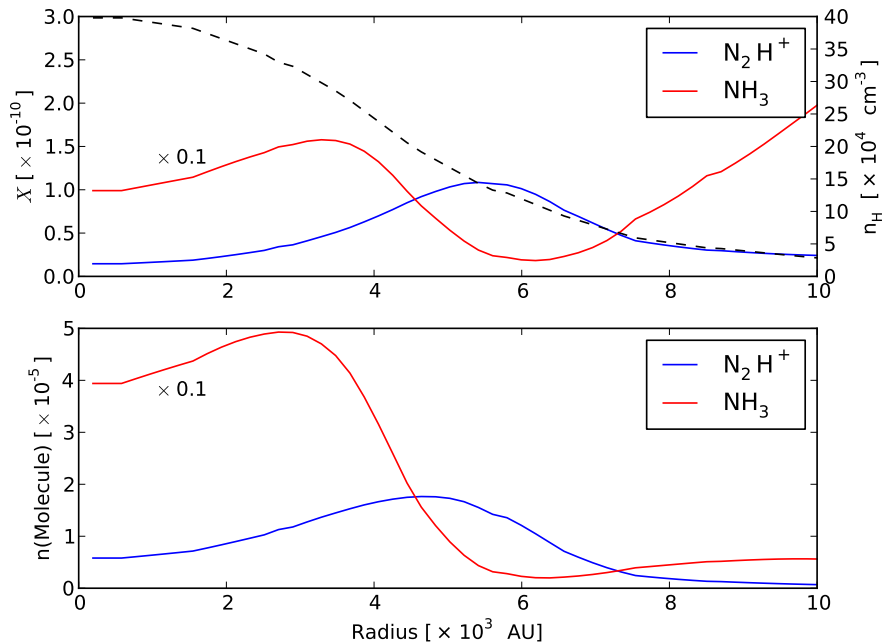


Figure 4.11: Plot of the relative (*top*) and absolute (*bottom*) abundances of NH_3 and N_2H^+ in the starless core of B 68. Both belong to the chemical model of B 68 that was found in Chapter 2 to predict the observed N_2H^+ (1-0) line profile best.

and decreases quickly towards larger radii. Hence, we expect that ammonia traces the central part even of the densest and coldest core of this study.

A potential heating source that could explain the increased gas temperature in the core center of B 68 are cosmic rays. However, cosmic rays that are strong enough to explain a gas temperature of 10 K in the core centers are in contradiction with CO observations of B 68 (Bergin et al. 2006). These authors also showed that a reduced gas-dust coupling by an order of magnitude could explain a temperature difference between the gas and dust in the core center. Moreover, they found that a small change in the size of the smallest grains could already lead to a strongly reduced gas-dust coupling. We are currently working on observational constraints on the dust opacities in the starless cores but this is work in progress.

We measured the ammonia temperature out to radii with hydrogen densities below $n_{\text{H}} \sim 5 \times 10^4 \text{ cm}^{-3}$ and did not observe a decoupling of gas and dust temperatures. However, it has to be kept in mind that the ammonia temperature is averaged over the full beam of the telescope and along the line-of-sight weighted by the ammonia density. Because of this averaging, the gas temperature derived with our analysis for the core centers is an upper limit. In contrast, at the outermost radii at which the (2,2) line is detected it is a lower limit. In the future, the gas temperature estimate could be refined by deeper observations of the (2,2) line. This is in principle possible since ammonia is in LTE already at low densities and it is abundant there as well. It would, however, require substantial observing time. Also, modeling the

ammonia distribution and its resulting emission would allow to put tighter constraints onto the gas temperature in the region where decoupling of the gas and dust temperatures is expected.

Alternative gas temperature tracers of the thermal decoupling are rare, since most molecules are subthermally excited at $n_{\text{H}} \sim 5 \times 10^4 \text{ cm}^{-3}$ (Evans 1999). Furthermore, their distribution within the cloud cores is not well constrained and any attempt to derive a temperature from their emission would require large modeling efforts and would probably lead to only weak constraints on the gas temperature. The most promising alternative might be CO and its isotopologues, since they are readily excited, have easily detectable emission, and are sensitive to different depths of the cores. However, CO molecules start to freeze out above $n_{\text{H}} \sim 10^4 \text{ cm}^{-3}$ (see Chapter 2), so that their emission traces mainly regions of lower densities and their sensitivity to the gas temperature in regions of beginning decoupling is probably limited.

4.7 SUMMARY

We have measured the emission of the $(J, K) = (1, 1)$ and $(2, 2)$ inversion transitions of ammonia in three starless cores contained in the Bok globules CB 17, CB 27, and B 68. We find that ammonia is abundant in the center of the starless cores and barely freezes out. Thus, it traces the center of the starless cores. We derive the kinetic temperature of ammonia representative for the gas temperatures in the cores and find for the core centers $T_{\text{gas}} = 11.7 \pm 1.2 \text{ K}$ in CB 17, $T_{\text{gas}} = 10.5 \pm 1.2 \text{ K}$ in CB 27 and $T_{\text{gas}} = 10.2 \pm 1.1 \text{ K}$ in B 68. In the case of CB 17 and CB 27, the central gas temperature is equal to the central dust temperature within the uncertainties. In contrast, the gas temperature in the core center of B 68 is about 2.5 K higher than the dust temperature. This is just within the uncertainties of both temperature estimates. Furthermore, it could also be a result of reduced gas-dust coupling in the core center which might have been boosted in this globule due to coagulation of the dust grains.

5.1 SUMMARY

In the long cascade of development stages of the ISM leading eventually to the formation of low-mass stars, prestellar cores are the step directly prior to the onset of gravitational collapse. In order to model the evolution of prestellar cores to individual stars, it is necessary to know the physical and chemical conditions in the cores. The goal of this thesis was to put new observational constraints onto these conditions.

With the *Herschel Space Observatory* and its sensitive photometers, it has for the first time become possible to observe the far-infrared portion of the thermal dust emission with a resolution that permits analyzing individual, nearby star-forming cores. As part of the *Herschel* Guaranteed Time Key project "Earliest Phases of star formation" (EPoS), a sample of seven starless cores contained in Bok globules has been observed. Bok globules are the simplest structured sites of star formation, because they are small, nearby and isolated making them ideal for detailed studies of the star formation process.

In Chapter 2 we presented dust temperature and hydrogen density maps of prestellar cores located in Bok globules that have been derived with a ray-tracing technique from *Herschel* and complementary (sub-)mm observations of the thermal dust emission. This method minimizes input model assumptions that may affect the interpretation of the dust emission. The resulting maps constitute the most accurate determination of the dust temperature and hydrogen density structure of prestellar cores from observations today. The dust temperature of the cores drops from 12 – 18 K in the envelopes to 8 – 13 K in the core centers while the central hydrogen density ranges from 10^4 cm^{-3} to several 10^5 cm^{-3} anti-correlated with the temperature. Most cores were found to be approximately thermally balanced with the tendency of being thermally supercritical.

Based on radially averaged profiles of the dust temperature and hydrogen density distributions

we modeled the chemical evolution of the gas in the cores. From the modeled abundances we obtained synthetic observations using line-radiative transfer calculations and compared them to observations of ^{13}CO , C^{18}O , and N_2H^+ . These molecules are complementary tracers of the conditions in the cores because CO freezes out in the core centers allowing N_2H^+ to build up in the gas phase. We found that CO is heavily depleted in all core centers and that also N_2H^+ is depleted at hydrogen densities above 10^5 cm^{-3} . The emission of both species does thus not trace the innermost regions of the core centers. Furthermore, we could constrain the chemical age of all cores to be of the order of 10^5 yr .

In Chapter 3 we tested, if the dust temperature and hydrogen density profiles derived with the ray-tracing technique are in agreement with radiative transfer models of the thermal equilibrium distributions of the cores. The cores were assumed to be only heated by the ISRF and to cool via thermal radiation. These processes should to first order determine the thermal conditions in the cores because it has been shown previously that the influence of the gas and cosmic rays on the thermal balance of the dust grains is very small if not negligible. We found that the radiative transfer models describe the temperature profiles derived with the ray-tracing technique very well confirming the reliability of this method. Furthermore, we tested the effect of using different dust opacity models and we found that the level of agreement is independent of the assumed models as long as they represent uncoagulated or only mildly coagulated dust grains. Only one model in our study that assumes the strongest coagulation led to significantly systematic flatter temperature profiles in the radiative transfer models. However, for all globules and dust models we have to increase the strength of the ISRF by a factor 2-3 otherwise the temperature derived by the radiative transfer is too low by about 2 K.

In Chapter 4 we presented observations of the ammonia (1,1) and (2,2) inversion transitions of three starless cores. From these observations we derived the kinematic gas temperatures and compared them to the dust temperatures in the cores. We found that both temperatures agree in the centers of two of the cores and that the gas is slightly warmer than the dust in the third core. The reduced central coupling in this core might be caused by a decreased collisional coupling of gas and dust caused by coagulation of the dust grains.

5.2 OUTLOOK

In Chapter 4 we used measurements of the ammonia inversion transitions to constrain the gas temperature in starless cores. In spite of very deep observations we could only constrain the temperature in the core centers. At lower densities where a decoupling of gas and dust temperatures is expected to occur, the emission got too weak. However, ammonia is probably the only tracer that permits relatively direct measurements of the gas temperature under the conditions where the decoupling occurs. Deriving the gas temperature from other molecules that trace the region of decoupling would require a significant modeling effort, since they typically also

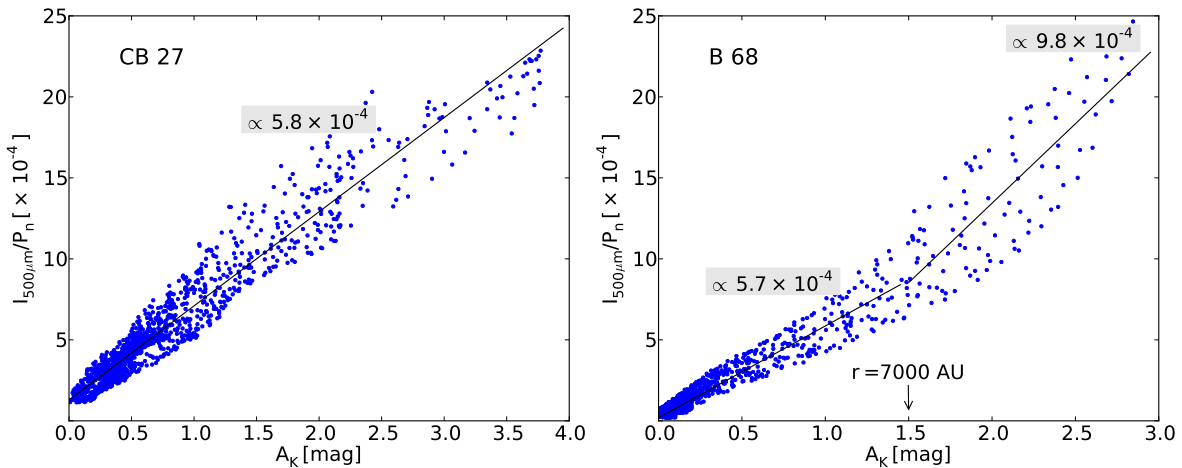


Figure 5.1: Following the procedure described in Shirley et al. (2011), we plot the ratio of the dust continuum emission at $500\ \mu\text{m}$ divided by the density weighted Planck function over the NIR extinction. The slope of the fit can be identified with the ratio of the dust extinction at $500\ \mu\text{m}$ and $2.2\ \mu\text{m}$ (Eq. 6 in Shirley et al. 2011).

emit from warmer outer parts which makes the interpretation of the emission difficult. Moreover, from most other molecules one would have to observe at least two rotational transitions at very different frequencies which would result in uncertainties of the relative calibration. My suggestion for a next step is therefore to obtain extremely deep observations of the ammonia inversion lines just for a few pointings in the region of expected decoupling in order to minimize the observing time required.

In principle, the dust emission maps of the globules obtained by *Herschel* and (sub-)mm telescopes in combination with near-infrared extinction maps have the potential to constrain the dust opacities in the cores. The results of a preliminary attempt to constrain the dust properties is shown in Fig. 5.1. Following the description by Shirley et al. (2011), we plotted the SPIRE $500\ \mu\text{m}$ emission normalized by a density-weighted Planck function over the near-infrared extinction of two prestellar cores. The slope of the distribution corresponds to the ratio of the dust extinction coefficients at $500\ \mu\text{m}$ and $2.2\ \mu\text{m}$. While the ratio is the same for both globules below $A_K \sim 1.5\ \text{mag}$ and approximately similar to that of OH5a dust (see Chapter 3), it increases for B 68 at a $A_K \gtrsim 1.5\ \text{mag}$ in accordance with models of strongly coagulated dust. However, in order to tap the full potential of the dust emission maps in their original resolution and complementary near-infrared extinction maps, we plan to apply a three-dimensional forward modeling of the thermal dust emission of the globules.

In Chapter 2 we found from time-dependent chemical models of CO and N_2H^+ a typical chemical age of the cores of about $10^5\ \text{yr}$. In the future, additional information on the nature of these prestellar cores can be obtained by expanding the chemical models and observations to deuterated species whose abundance is particularly sensitive to the thermal history of the cores. In a further step one could also add a time-dependence to the physical conditions to obtain information on the formation process of the cores.

Magnetic fields have not been studied in this thesis but their role in the development of prestellar cores towards protostellar collapse is expected to be important, because they impede core contraction and remove angular momentum. Only in a handful of prestellar cores the magnetic field has been constrained (Ward-Thompson et al. 2000; Wolf et al. 2003; Crutcher et al. 2004). Low sensitivity of former bolometers has so far hampered a systematic study of the magnetic field in prestellar cores. The polarimeter of the new SCUBA-2 bolometer array at the JCMT has the potential to observe the polarized dust emission with high sensitivity of a significant number of prestellar cores allowing to measure the magnetic fields and determine their influence on the formation and evolution of prestellar cores much better. The EPoS sample would be an obvious choice for such observations.

Although prestellar cores are mostly found not to show substructure (e.g., Olmi et al. 2005; Schnee et al. 2010), some exceptions have been found (e.g., Olmi et al. 2005; Schnee et al. 2010; Bourke et al. 2012; Chen et al. 2012). The true nature of these condensations within starless cores is debated but they are certainly an evolutionary step towards protostars. Further prestellar cores need to be searched for these objects in order to place them into the sequence of star formation. The prestellar core in CB 244 is the prime candidate for this evolutionary stage in the EPoS sample since it is the gravitationally most unstable prestellar core.

ACKNOWLEDGMENTS

I would like to thank my advisor Ralf Launhardt for his commitment and support during the three years of this thesis. I would also like to thank Thomas Henning who gave me the opportunity to become a member of the EPoS team during the exciting times when the Herschel data was arriving and who was always available for discussions. I am also very thankful to Dmitry Semenov who introduced me to astrochemistry and helped me with the chemical modeling.

I enjoyed the probably unique social, cooperative, and stimulating atmosphere at the MPIA which so many people have been contributing to. In particular, I would like to thank my various office mates and collaborators.

In the last steps of thesis writing I got lots of support from Hendrik Linz, Markus Nielbock, and Amy Stutz and I am very thankful for your efforts.

I would also like to thank Simon Glover for examining this thesis.

Finally, I would like to thank Janette, my family and friends for their support, understanding, and the good times we had over the last three years.

BIBLIOGRAPHY

- Aikawa, Y., Herbst, E., Roberts, H., & Caselli, P. 2005, *ApJ*, 620, 330
- Albertsson, T., Semenov, D. A., Vasyunin, A. I., Henning, T., & Herbst, E. 2013, *ApJS*, 207, 27
- Alves, F. O. & Franco, G. A. P. 2007, *A&A*, 470, 597
- Alves, J. F., Lada, C. J., & Lada, E. A. 2001, *Nature*, 409, 159
- André, P. 2013, ArXiv e-prints
- André, P., Basu, S., & Inutsuka, S. 2009, *The formation and evolution of prestellar cores*, ed. G. Chabrier (Cambridge University Press), 254
- André, P., Men'shchikov, A., Bontemps, S., et al. 2010, *A&A*, 518, L102
- André, P., Ward-Thompson, D., & Greaves, J. 2012, *Science*, 337, 69
- Bachiller, R., Guilloteau, S., & Kahane, C. 1987, *A&A*, 173, 324
- Bacmann, A., André, P., Puget, J.-L., et al. 2000, *A&A*, 361, 555
- Bacmann, A., Lefloch, B., Ceccarelli, C., et al. 2002, *A&A*, 389, L6
- Bacmann, A., Taquet, V., Faure, A., Kahane, C., & Ceccarelli, C. 2012, *A&A*, 541, L12
- Ballesteros-Paredes, J., Klessen, R. S., & Vázquez-Semadeni, E. 2003, *ApJ*, 592, 188
- Bergin, E. A., Alves, J., Huard, T., & Lada, C. J. 2002, *ApJ*, 570, L101
- Bergin, E. A., Maret, S., van der Tak, F. F. S., et al. 2006, *ApJ*, 645, 369
- Bergin, E. A. & Tafalla, M. 2007, *ARA&A*, 45, 339
- Beuther, H., Henning, T., Linz, H., et al. 2010, *A&A*, 518, L78
- Beuther, H., Tackenberg, J., Linz, H., et al. 2012, *A&A*, 538, A11
- Bianchi, S., Gonçalves, J., Albrecht, M., et al. 2003, *A&A*, 399, L43
- Bigiel, F., Leroy, A., Walter, F., et al. 2008, *AJ*, 136, 2846
- Biham, O., Furman, I., Pirronello, V., & Vidali, G. 2001, *ApJ*, 553, 595
- Bok, B. J. 1948, *Harvard Observatory Monographs*, 7, 53
- Bonnor, W. B. 1956, *MNRAS*, 116, 351

- Bourke, T. L., Myers, P. C., Caselli, P., et al. 2012, *ApJ*, 745, 117
- Brinch, C. & Hogerheijde, M. R. 2010, *A&A*, 523, A25
- Cardelli, J. A., Clayton, G. C., & Mathis, J. S. 1989, *ApJ*, 345, 245
- Carlhoff, P., Nguyen Luong, Q., Schilke, P., et al. 2013, *ArXiv e-prints*
- Carter, M., Lazareff, B., Maier, D., et al. 2012, *A&A*, 538, A89
- Caselli, P., Benson, P. J., Myers, P. C., & Tafalla, M. 2002, *ApJ*, 572, 238
- Caselli, P., Myers, P. C., & Thaddeus, P. 1995, *ApJ*, 455, L77
- Caselli, P., Walmsley, C. M., Tafalla, M., Dore, L., & Myers, P. C. 1999, *ApJ*, 523, L165
- Chen, X., Arce, H. G., Dunham, M. M., et al. 2012, *ApJ*, 751, 89
- Chen, X., Arce, H. G., Zhang, Q., et al. 2013, *ApJ*, 768, 110
- Connelley, M. S., Reipurth, B., & Tokunaga, A. T. 2008, *AJ*, 135, 2526
- Crutcher, R. M., Nutter, D. J., Ward-Thompson, D., & Kirk, J. M. 2004, *ApJ*, 600, 279
- Danby, G., Flower, D. R., Valiron, P., Schilke, P., & Walmsley, C. M. 1988, *MNRAS*, 235, 229
- de Geus, E. J., de Zeeuw, P. T., & Lub, J. 1989, *A&A*, 216, 44
- Draine, B. T. 1978, *ApJS*, 36, 595
- Draine, B. T. & Bertoldi, F. 1996, *ApJ*, 468, 269
- Ebert, R. 1955, *ZAp*, 37, 217
- Evans, II, N. J. 1999, *ARA&A*, 37, 311
- Evans, II, N. J., Rawlings, J. M. C., Shirley, Y. L., & Mundy, L. G. 2001, *ApJ*, 557, 193
- Ford, A. B. & Shirley, Y. L. 2011, *ApJ*, 728, 144
- Foster, J. B. & Goodman, A. A. 2006, *ApJ*, 636, L105
- Galli, D., Walmsley, M., & Gonçalves, J. 2002, *A&A*, 394, 275
- Garrod, R. T. 2013, *ApJ*, 765, 60
- Garrod, R. T. & Herbst, E. 2006, *A&A*, 457, 927
- Garrod, R. T., Wakelam, V., & Herbst, E. 2007, *Astron. Astrophys*, 467, 1103
- Goldsmith, P. F. 2001, *ApJ*, 557, 736
- Gonçalves, J., Galli, D., & Walmsley, M. 2004, *A&A*, 415, 617
- Goodman, A. A., Barranco, J. A., Wilner, D. J., & Heyer, M. H. 1998, *ApJ*, 504, 223
- Goodman, A. A., Benson, P. J., Fuller, G. A., & Myers, P. C. 1993, *ApJ*, 406, 528
- Griffin, M. J., Abergel, A., Abreu, A., et al. 2010, *A&A*, 518, L3
- Hasegawa, T. I. & Herbst, E. 1993, *MNRAS*, 263, 589
- Heiderman, A., Evans, II, N. J., Allen, L. E., Huard, T., & Heyer, M. 2010, *ApJ*, 723, 1019
- Heiles, C. & Crutcher, R. 2005, in *Lecture Notes in Physics*, Berlin Springer Verlag, Vol. 664, *Cosmic Magnetic Fields*, ed. R. Wielebinski & R. Beck, 137
- Hennebelle, P. 2013, in *EAS Publications Series*, Vol. 62, *EAS Publications Series*, 67–94
- Hennebelle, P. & Chabrier, G. 2008, *ApJ*, 684, 395

- Henning, T., Linz, H., Krause, O., et al. 2010, *A&A*, 518, L95
- Herbst, E. & Klemperer, W. 1973, *ApJ*, 185, 505
- Herbst, E. & van Dishoeck, E. F. 2009, *ARA&A*, 47, 427
- Herschel, W. 1785, *Royal Society of London Philosophical Transactions Series I*, 75, 213
- Ho, P. T. P., Barrett, A. H., Myers, P. C., et al. 1979, *ApJ*, 234, 912
- Hopkins, A. M. & Beacom, J. F. 2006, *ApJ*, 651, 142
- Hotzel, S., Harju, J., Juvela, M., Mattila, K., & Haikala, L. K. 2002, *A&A*, 391, 275
- Indriolo, N., Neufeld, D. A., Gerin, M., et al. 2012, *ApJ*, 758, 83
- Jappsen, A.-K. & Klessen, R. S. 2004, *A&A*, 423, 1
- Juvela, M., Harju, J., Ysard, N., & Lunttila, T. 2012, *A&A*, 538, A133
- Kainulainen, J., Lehtinen, K., & Harju, J. 2006, *A&A*, 447, 597
- Kainulainen, J., Ragan, S. E., Henning, T., & Stutz, A. 2013, *A&A*, 557, A120
- Kandori, R., Nakajima, Y., Tamura, M., et al. 2005, *AJ*, 130, 2166
- Katz, N., Furman, I., Biham, O., Pirronello, V., & Vidali, G. 1999, *ApJ*, 522, 305
- Kennicutt, Jr., R. C. 1998, *ApJ*, 498, 541
- Kessler, M. F., Steinz, J. A., Anderegg, M. E., et al. 1996, *A&A*, 315, L27
- Keto, E. & Caselli, P. 2008, *ApJ*, 683, 238
- Kirk, J. M., Ward-Thompson, D., & André, P. 2005, *MNRAS*, 360, 1506
- Klessen, R. S., Ballesteros-Paredes, J., Vázquez-Semadeni, E., & Durán-Rojas, C. 2005, *ApJ*, 620, 786
- Kun, M. 1998, *ApJS*, 115, 59
- Lai, S.-P., Velusamy, T., Langer, W. D., & Kuiper, T. B. H. 2003, *AJ*, 126, 311
- Langer, W. D., Graedel, T. E., Frerking, M. A., & Armentrout, P. B. 1984, *ApJ*, 277, 581
- Launhardt, R. & Henning, T. 1997, *A&A*, 326, 329
- Launhardt, R., Nutter, D., Ward-Thompson, D., et al. 2010, *ApJS*, 188, 139
- Launhardt, R., Pavlyuchenkov, Y., Gueth, F., et al. 2009, *A&A*, 494, 147
- Launhardt, R. & Sargent, A. I. 2001, *ApJ*, 562, L173
- Launhardt, R., Stutz, A. M., Schmiedeke, A., et al. 2013, *A&A*, 551, A98
- Lee, C. W. & Myers, P. C. 1999, *ApJS*, 123, 233
- Lee, H.-H., Herbst, E., Pineau des Forets, G., Roueff, E., & Le Bourlot, J. 1996, *A&A*, 311, 690
- Lee, J.-E., Evans, II, N. J., Shirley, Y. L., & Tatematsu, K. 2003, *ApJ*, 583, 789
- Linz, H., Krause, O., Beuther, H., et al. 2010, *A&A*, 518, L123
- Lippok, N., Launhardt, R., Semenov, D., et al. 2013, *A&A*, 560, A41
- Lizano, S. & Shu, F. H. 1989, *ApJ*, 342, 834
- Lodders, K., Palme, H., & Gail, H.-P. 2009, *Landolt Börnstein*, 44
- Loinard, L., Mioduszewski, A. J., Torres, R. M., et al. 2011, in *Revista Mexicana de Astrono-*

- mia y Astrofísica Conference Series, Vol. 40, *Revista Mexicana de Astronomía y Astrofísica Conference Series*, 205–210
- Lombardi, M., Alves, J., & Lada, C. J. 2006, *A&A*, 454, 781
- Maret, S., Faure, A., Scifoni, E., & Wiesenfeld, L. 2009, *MNRAS*, 399, 425
- Mathis, J. S., Mezger, P. G., & Panagia, N. 1983, *A&A*, 128, 212
- Mathis, J. S., Rumpl, W., & Nordsieck, K. H. 1977, *ApJ*, 217, 425
- Meidt, S. E., Schinnerer, E., Garcia-Burillo, S., et al. 2013, *ArXiv e-prints*
- Miville-Deschênes, M.-A. & Lagache, G. 2005, *ApJS*, 157, 302
- Myers, P. C., Fuller, G. A., Goodman, A. A., & Benson, P. J. 1991, *ApJ*, 376, 561
- Nielbock, M., Launhardt, R., Steinacker, J., et al. 2012, *A&A*, 547, A11
- Nutter, D. & Ward-Thompson, D. 2007, *MNRAS*, 374, 1413
- Öberg, K. I., Linnartz, H., Visser, R., & van Dishoeck, E. F. 2009a, *ApJ*, 693, 1209
- Öberg, K. I., van Dishoeck, E. F., & Linnartz, H. 2009b, *A&A*, 496, 281
- Olmi, L., Testi, L., & Sargent, A. I. 2005, *A&A*, 431, 253
- Ormel, C. W., Min, M., Tielens, A. G. G. M., Dominik, C., & Paszun, D. 2011, *A&A*, 532, A43
- Ormel, C. W., Paszun, D., Dominik, C., & Tielens, A. G. G. M. 2009, *A&A*, 502, 845
- Ossenkopf, V. 1993, *A&A*, 280, 617
- Ossenkopf, V. & Henning, T. 1994, *A&A*, 291, 943
- Ott, M., Witzel, A., Quirrenbach, A., et al. 1994, *A&A*, 284, 331
- Pagani, L., Pardo, J.-R., Apponi, A. J., Bacmann, A., & Cabrit, S. 2005, *A&A*, 429, 181
- Pagani, L., Steinacker, J., Bacmann, A., Stutz, A., & Henning, T. 2010, *Science*, 329, 1622
- Palmeirim, P., André, P., Kirk, J., et al. 2013, *A&A*, 550, A38
- Pavlyuchenkov, Y., Henning, T., & Wiebe, D. 2007, *ApJ*, 669, L101
- Pavlyuchenkov, Y., Wiebe, D., Launhardt, R., & Henning, T. 2006, *ApJ*, 645, 1212
- Perrot, C. A. & Grenier, I. A. 2003, *A&A*, 404, 519
- Pickett, H. M., Poynter, R. L., Cohen, E. A., et al. 1998, *J. Quant. Spec. Radiat. Transf.*, 60, 883
- Pilbratt, G. L., Riedinger, J. R., Passvogel, T., et al. 2010, *A&A*, 518, L1
- Pitann, J., Linz, H., Ragan, S., et al. 2013, *ApJ*, 766, 68
- Plummer, H. C. 1911, *MNRAS*, 71, 460
- Poglitsch, A., Waelkens, C., Geis, N., et al. 2010, *A&A*, 518, L2
- Porter, T. A. & Strong, A. W. 2005, in *International Cosmic Ray Conference*, Vol. 4, *International Cosmic Ray Conference*, 77
- Preibisch, T., Ossenkopf, V., Yorke, H. W., & Henning, T. 1993, *A&A*, 279, 577
- Ragan, S., Henning, T., Krause, O., et al. 2012, *A&A*, 547, A49
- Robitaille, T. P. 2011, *A&A*, 536, A79

- Rosolowsky, E. W., Pineda, J. E., Foster, J. B., et al. 2008, *ApJS*, 175, 509
- Schinnerer, E., Meidt, S. E., Pety, J., et al. 2013, ArXiv e-prints
- Schmalzl, M., Launhardt, R., & Stutz, A. M. submitted, *A&A*
- Schnee, S., Brunetti, N., Di Francesco, J., et al. 2013, *ApJ*, 777, 121
- Schnee, S., Enoch, M., Johnstone, D., et al. 2010, *ApJ*, 718, 306
- Schöier, F. L., van der Tak, F. F. S., van Dishoeck, E. F., & Black, J. H. 2005, *A&A*, 432, 369
- Schruba, A., Leroy, A. K., Walter, F., Sandstrom, K., & Rosolowsky, E. 2010, *ApJ*, 722, 1699
- Semenov, D., Hersant, F., Wakelam, V., et al. 2010, *A&A*, 522, A42
- Shalabiea, O. M. & Greenberg, J. M. 1994, *Astron. Astrophys*, 290, 266
- Shirley, Y. L., Huard, T. L., Pontoppidan, K. M., et al. 2011, *ApJ*, 728, 143
- Shirley, Y. L., Nordhaus, M. K., Grcevich, J. M., et al. 2005, *ApJ*, 632, 982
- Stahler, S. W. & Palla, F. 2005, *The Formation of Stars*
- Stamatellos, D. & Whitworth, A. P. 2003, *A&A*, 407, 941
- Straižys, V., Černis, K., & Bartašiūtė, S. 2003, *A&A*, 405, 585
- Stutz, A., Launhardt, R., Linz, H., et al. 2010, *A&A*, 518, L87
- Stutz, A. M., Rieke, G. H., Bieging, J. H., et al. 2009, *ApJ*, 707, 137
- Tafalla, M., Myers, P. C., Caselli, P., & Walmsley, C. M. 2004, *A&A*, 416, 191
- Tafalla, M., Myers, P. C., Caselli, P., Walmsley, C. M., & Comito, C. 2002, *ApJ*, 569, 815
- Tafalla, M. & Santiago, J. 2004, *A&A*, 414, L53
- Tielens, A. G. G. M., Tokunaga, A. T., Geballe, T. R., & Baas, F. 1991, *ApJ*, 381, 181
- van der Tak, F. F. S., Black, J. H., Schöier, F. L., Jansen, D. J., & van Dishoeck, E. F. 2007, *A&A*, 468, 627
- van Dishoeck, E. F., Jonkheid, B., & van Hemert, M. C. 2006, *Faraday discussion*, Vol. 133, *Photoprocesses in protoplanetary disks*, ed. I. R. Sims & D. A. Williams (Royal Society of Chemistry, Cambridge), 231
- Vasyunin, A. I. & Herbst, E. 2013, *ApJ*, 769, 34
- Walmsley, C. M. & Ungerechts, H. 1983, *A&A*, 122, 164
- Ward-Thompson, D., André, P., Crutcher, R., et al. 2007, *Protostars and Planets V*, 33
- Ward-Thompson, D., André, P., & Kirk, J. M. 2002, *MNRAS*, 329, 257
- Ward-Thompson, D., Kirk, J. M., Crutcher, R. M., et al. 2000, *ApJ*, 537, L135
- Ward-Thompson, D., Motte, F., & André, P. 1999, *MNRAS*, 305, 143
- Ward-Thompson, D., Scott, P. F., Hills, R. E., & André, P. 1994, *MNRAS*, 268, 276
- Weingartner, J. C. & Draine, B. T. 2001, *ApJ*, 548, 296
- Whitworth, A. P. & Ward-Thompson, D. 2001, *ApJ*, 547, 317
- Willacy, K., Langer, W. D., & Allen, M. 2002, *ApJ*, 573, L119
- Willacy, K., Langer, W. D., & Velusamy, T. 1998, *ApJ*, 507, L171
- Wilson, T. L. & Rood, R. 1994, *ARA&A*, 32, 191

- Witt, A. N., Oliveri, M. V., & Schild, R. E. 1990, *AJ*, 99, 888
- Wolf, S., Launhardt, R., & Henning, T. 2003, *ApJ*, 592, 233
- Xie, T., Allen, M., & Langer, W. D. 1995, *ApJ*, 440, 674
- Young, C. H. & Evans, II, N. J. 2005, *ApJ*, 627, 293
- Zucconi, A., Walmsley, C. M., & Galli, D. 2001, *A&A*, 376, 650